

Molecular Modelling of Nanopore Structures

by

Thomas C. McDermott, BE

**Submitted to the School of Chemical and Bioprocess Engineering,
University College Dublin,
for the degree of Doctor of Philosophy (PhD)**

October 2011

Under the supervision of
Prof. J.M.Don MacElroy, BE, PhD, MAIChE, MIChE



An Cholaíste Ollscoile, Baile Átha Cliath
Scoil na hInnealtóireachta Ceimicí agus Bithphróisis

For Nuala, Charlie, Linda, John, Roger, and Nurwahida.

Acknowledgements

I wish to express my deep gratitude to my supervisor Professor J.M.D. MacElroy for his expertise and thoughtfulness during the course of my research, and for his patience, support, and encouragement which ensured the successful completion of this work. I also thank him for giving me the opportunity to gain experience as a lecturer in UCD, providing financial support, for introducing me to the field of molecular simulation and the theory of diffusion, and more importantly, for providing a model of scientific rigour, diligence and integrity which I will try to emulate.

I would also like to express my sincerest gratitude to the staff of the UCD School of Chemical Engineering, both past and present, who have contributed to an environment where it was a joy to work and I thank them for their kindness and support over the years. Despite the risk of leaving someone out, I would still like to thank the following individually: Dr. Niall English, for his friendship, encouragement, and generous provision of computational resources, Dr. D.A. Mooney who has helped me greatly through the provision of funding and computer facilities, Prof. Daniel Carroll for his encouragement and support which led me to undertake postgraduate studies and who provided financial support through Labscan Ltd., Dr John Byrne, Prof. Brian Glennon, Dr Frank MacLoughlin, who provided lecture notes and assisted me with courses which I taught in UCD, Dr Dermot Malone for answering questions on computational problems and Dr Susan McDonnell for helping me with administrative issues. I thank Brian Turner for his expertise in high performance computing hardware in developing and maintaining the computer clusters. I thank Aoife Carney for making the School office so friendly and helpful and for the numerous problems she has assisted me with, and acts of kindness she has organized for my benefit over the years.

I also wish to thank colleagues past and present in the simulation group for their friendship, encouragement, and support, including: Dr Mark Purdue, Dr John Moloney, Dr Matt Landowski, Dr Taslima Akter, Dr Sanket Deshmukh, Savita Kulkarni, Dr Amsarani Ramamoorthy, Dr Gleb Solomentsev, and Ritwik Kavathekar. I also wish to thank Caoimhin Mullally and Cian O'Meara for their friendship and support in my undergraduate years which I never forget.

Finally, I thank my family: my parents Nuala and Charlie for their selfless devotion and the sacrifices made to educate me and my siblings, my sister Linda and brothers, John and Roger for their constant encouragement and support, and my beloved wife Nurwahida, whose love, patience and support have made this work possible.

Abstract

Partitioning and transport within porous structures are key phenomena in a wide variety of Chemical Engineering industrial processes ranging from pressure swing and thermal swing adsorbers, chromatographic operations and membranes separations to heterogeneous catalytic and non-catalytic reaction systems. The focus of the research reported in this thesis is on gases in contact with model nanoporous materials and while there currently exists a broad body of work on this topic in the open literature there are significant questions which remain to be answered on a range of issues.

Of primary interest in this work are porous materials composed of silica, notably because of their wide use and versatility in applications ranging from low temperatures to moderately high temperatures. Molecular simulation techniques are employed to investigate three explicit topics in this research: (a) adsorption and diffusion of a simple model fluid in a crystalline silica nanopore; (b) molecular dynamics of diffusion and permselectivity in dense nanoporous amorphous silica films; and (c) kinetic Monte Carlo of the formation of thin silica films via chemical vapour deposition as a preparatory route towards composite membrane fabrication.

In the first topic the behaviour of a model WCA/Lennard-Jones methane vapour confined within a crystalline silica nanopore is investigated using Grand Canonical Monte Carlo (GCMC) and equilibrium and non-equilibrium molecular dynamics (EMD and NEMD) simulations. Simulations are conducted over a range of fluid densities which span the two-phase coexistence and supercritical regions for the pure fluid adsorbed within the crystalline nanopore. The GCMC simulations provide the low temperature coexistence points for the open pore fluid and are used to locate the capillary critical temperature for the system. The equilibrium configurational states obtained from these simulations are then used as input data for the EMD simulations in which the self-diffusion coefficients are computed using the Einstein equation. NEMD colour diffusion simulations are also conducted to validate the use of a system averaged Einstein analysis for this inhomogeneous fluid. In all cases excellent agreement is observed between the

equilibrium (linear response theory) predictions for the diffusivities and non-equilibrium colour diffusivities.

The simulation results are also compared with the quasi-hydrodynamic theory of Pozhar and Gubbins (1993, 1997). The model fluid and the nature of the fluid wall interactions employed conform to the decomposition of the particle-particle interaction potential explicitly used by Pozhar and Gubbins and the local self-diffusivity is calculated from the local fluid-fluid and fluid wall hard core collision frequencies. While this theory provides reasonable results at moderate pore fluid densities, poor agreement is observed in the low and high density limits.

The second topic investigated in this work is the origin of permselectivity in dense silica films which possess a pore structure with pore sizes commensurate with the molecular size of the diffusing gas species. This forms part of an ongoing study in gas mixture separation technology involving the development of novel composite ceramic membranes suitable for use across a broad range of process conditions. A common theme in these studies is the use of mesoporous/microporous support materials (e.g. α -alumina/ γ -alumina, Vycor etc) with a pore size of approximately 5 nm upon which is deposited a silica layer containing subnanometer pores. This layer is the selective coating which itself is typically 30-100 nm thick. While it is generally assumed that the transport process of the gas species within the selective layer is activated in nature, there are anomalies with this simplified picture. In this thesis a new model is developed which, for the first time, explains the permselective behaviour of the *thin* selective coatings ubiquitous to membrane separation processes. The model involves the possible existence of two primary transport domains within the solid film one of which rapidly conducts the permeating gas while the second domain involves a slow diffusion mode characterised by normal Fickian transport. To validate the model, molecular dynamics simulations are conducted for diffusion of a number of simple gases (He, N₂ and CO₂) within silica glasses over a range of solid densities. The silica media employed in these studies are based on a novel approach developed in this work for the construction of three-dimensionally

periodic atomistic structures of silica of arbitrary density in which network bond connectivity is ensured. The results obtained from this work are in agreement with experimental observations and confirm the existence of dual mode transport which is central to the interpretation of the permselectivity in composite membranes systems.

The third topic of this thesis is a continuation of earlier work reported by the molecular simulations group at UCD on the possibility of fabricating membranes with both high kinetic selectivities and acceptable permeability. It is known that the experimental conditions employed during composite membrane fabrication via chemical vapour deposition (CVD) processes can have a very significant influence on the fundamental microscopic details of the membranes formed. In this work, the creation of moderately density silica films is investigated via direct simulation of the CVD process at intermediate to high temperatures. To model the creation of nanoporous silica layers via CVD a hybrid kinetic Monte-Carlo (KMC) method is applied in which lattice KMC is used for the elementary reactions and an off-lattice method is employed for silica network relaxation. Silica film growth is simulated by deposition onto non-porous silica (SiO_2) substrates from the chemical precursors $\text{Si}(\text{OH})_4$ and TEOS (tetraethoxysilane) via low pressure chemical vapour deposition (LPCVD). The influence of deposition temperature and pressure on the properties of the SiO_x layers is addressed via analysis of the film growth rates, density profiles of the deposited thin films, pore size distributions and pore accessibility for layers of different thickness (8 - 18 nm). A comparison of the simulation results with experimental observations is also carried out where possible. This work is an initial step in the validation of the KMC algorithm which will form the basis for simulations to be conducted in a later project on thin film growth on porous substrates.

Contents

List of Figures	x
List of Tables	xiv
1 Introduction	1
2 Literature Survey	5
2.1 Gas separation in porous membranes	5
2.1.1 Activated diffusion	6
2.1.2 Molecular Sieving	7
2.1.3 Surface diffusion	8
2.1.4 Knudsen diffusion	9
2.1.5 Transition State Theory	10
2.2 Overview of liquid theory	12
2.3 Lattice diffusion	15
2.4 Simulation	16
2.4.1 MD	16
2.4.2 KMC	18
2.4.2.1 Bortz-Kalos-Liebowitz Algorithm	19
2.4.2.2 Applications to deposition	19
2.4.3 Tricks of the trade	20
2.4.3.1 PBC and Minimum Image	20
2.4.3.2 Truncated Potentials	22
2.4.3.3 Verlet List	23
2.4.3.4 Cell linked lists	26
2.4.3.5 Long Ranged Forces -Electrostatics	29

2.4.3.6	Hoshen Kopelman Algorithm	30
2.4.3.7	Non-Lattice Hoshen Kopelman Algorithm	31
2.4.4	Model silica systems	33
2.4.4.1	Overview of Force Fields	33
2.4.4.2	Simulation applications	35
2.4.5	Characterisation of free space	37
2.4.5.1	Pore Size Distribution	37
2.4.5.1	Curve smoothing and differentiation	43
2.5	Transport in Nanopores	44
2.6	CVD results	45
3	Simulation of Adsorption and Diffusion in a Model Silica Pore Structure	48
3.1	The Model Pore Structure	48
3.2	Simulation Methods	52
3.3	The Diffusion Model	53
3.4	Results and Discussion	57
3.4.1	Equilibrium Adsorption	57
3.4.2	Diffusion Studies	58
3.4.2.1	Einstein Diffusion	58
3.4.2.2	Colour Diffusion	59
3.4.2.3	Pozhar-Gubbins Theory	62
3.5	Summary	71

4	Exploratory Studies of Diffusion in Dense Silica Films: Background, Methodology and Results	74
4.1	Background	74
4.2	Simulation Methodology	81
4.2.1	Low-to-Moderate Density Silica Structures	81
4.2.2	The Molecular Dynamics Method and Potential Functions	90
4.3	Modelling	94
4.4	Results and Discussion	98
5	Kinetic Monte Carlo Simulation of the Formation of Thin Solid Films of Silica via Chemical Vapour Deposition: Methodology	115
5.1	The Substrate Material	115
5.2	Reaction Kinetics	116
5.3	The Kinetic Monte Carlo Algorithm	125
5.3.1	The Reaction Frequencies and Reagent Partitioning	125
5.3.2	Reagent Accessibility and Percolation	131
5.3.3	The Bortz-Kalos-Lebowitz KMC Algorithm	137
5.3.4	Structural Relaxation via Canonical Monte Carlo	138
6	Kinetic Monte Carlo Simulation of the Formation of Thin Solid Films of Silica via Chemical Vapour Deposition: Results and Discussion	141
6.1	Film Growth Rates	141
6.2	Film Mass and Number Density Profiles	145
6.3	Pore Size Distributions and Void Accessibilities	155
7	Conclusions and Recommendations	171

List of Figures

2.1	Confined motion inside a molecular matrix	10
2.2	Overview of fluid theory	13
2.3	Examples of some collision types	14
2.4	Schematic showing periodic boundary conditions in 2D	21
2.5 (a)	Verlet neighbour list	24
2.5 (b)	Arrays for storing the Verlet neighbour list	25
2.6 (a)	Two dimensional illustration of the cell list	27
2.6 (b)	Linked list chain of atoms in cell	28
2.6 (c)	Linked list data structure	29
2.7 (a)	Simple network of 16 nodes and 24 links	31
2.7 (b)	Cluster labels for nodes and links	34
2.8	Definition of pore size	38
2.9	Pore size distribution algorithm	41
3.2(a)	Single lattice unit of the crystalline structure of the pore wall	49
3.1(b)	The fundamental unit cell	50
3.2	The grid structure for sampling collisions	53
3.3	Equilibrium adsorption isotherms	59
3.4	Snapshots of the formation of the adsorbed	61
3.5	View along the pore axis for $\mu_{\text{ex}}/kT = -14$ at 130K	62
3.6 (a)	The self-diffusion averaged over the pore volume as a function of pore loading for $T = 130$ K	63

3.6 (b)	The self-diffusion averaged over the pore volume as a function of pore loading for $T = 110\text{ K}$	63
3.7	Reduced pore fluid density and colour mole fraction profiles	64
3.8	Colour mole fraction profiles for $\langle n_f^* \rangle = 0.3875$ and $T = 130\text{K}$	65
3.9	The particle flux as a function of time	66
3.10	Snapshots of the adsorbed particles	70
3.11	Volume-averaged fluid-wall and fluid-fluid collision frequencies	71
3.12	Hard sphere pore averaged self-diffusion coefficients	72
4.1	SEM image of a thin film of SiO_2 and schematic drawing of a permselective membrane	75
4.2	Inverse mean square displacements (MSDs) of the centre of mass of the trace gas species as functions of $1/t^{2/d_w}$	79
4.3	Average percolation cluster size for gases as functions of the relative density of the nanoporous silica medium	80
4.4	2D representations of periodically replicated clusters	82
4.5 (a)	Etching algorithm (part a)	84
4.5 (b)	Etching algorithm (part b)	85
4.6	Determining the bonds which cross the system boundaries	87
4.7	Boundary crossing bond in a 2D representation of clusters	87
4.8	Clusters found for different periodic boundary conditions	88
4.9 (a)	‘Superconducting’ clusters / poor conductor mixture	95
4.9 (b)	Schematic of MSD of a random walker diffusion	95
4.10 (a)	MSD of helium atoms in nanoporous silica at 473K	99
4.10 (b,c)	MSD of helium atoms in nanoporous silica at 673K , 873K	100
4.11 (a, b)	MSD of N_2 molecules in nanoporous silica at 473K , 673K	101

4.11 (c)	MSD of N ₂ molecules in nanoporous silica at 873K	102
4.12 (a, b)	MSD of CO ₂ molecules in nanoporous silica at 473K, 673K	103
4.12 (c)	MSD of CO ₂ molecules in nanoporous silica at 873K	104
4.13	Nonlinear regression in Mathematica	104
4.14	Helium diffusivity as a function of temperature	105
4.15	Deconvolution of the MSD	108
4.16	Fickian diffusivity as a function of density	109
4.17	Fickian diffusivity as a function of temperature	110
4.18	Percolation cluster size as a function of temperature	113
5.1	Snapshot of the initial amorphous substrate used for deposition	117
5.2	Layer-averaged equilibrium adsorption/reaction term	120
5.3	Hypothetical formation of a strained two-membered oxygen ring during silanol condensation	125
5.4	Grid of subcells used in the KMC deposition algorithm	126
5.5	Cell connectivity on the 3D lattice	135
5.6	2D example of the deposited layer	136
6.1	SiO _x film growth rate as a function of precursor pressure	143
6.2	SiO _x film growth rate as a function of temperature	145
6.3 (a)	Mass density as a function of layer depth at 473K	148
6.3 (b, c)	Mass density as a function of layer depth at 673K, 873 K	149
6.4	Average mass density as a function of deposition pressure	150
6.5	Oxygen atomic number density profiles with Si(OH) ₄ precursor	151
6.6 (a)	Oxygen and carbon atomic number density profiles with TEOS at 473K and a precursor pressure of 1.42 torr	152
6.6 (b)	Oxygen and carbon atomic number density profiles with	153

	TEOS at 873K and a precursor pressure of 2.84×10^{-4} torr	
6.7	Ethyl number fraction in the 3.5 nm thick surface layer of the TEOS based CVD films as a function of precursor pressure	154
6.8 (a)	Pore size distributions for CVD layers formed at 473K	156
6.8 (b)	Pore size distributions for CVD layers formed at 873K	157
6.9	Average pore radius for the simulated nanoporous layers as a function of precursor pressure	159
6.10	Parity plot for the accessible pore volumes	161
6.11	Predicted permeances and permselectivity as a function of the membrane thickness based on assumptions (1) and (2).	166
6.12	Predicted permeances and permselectivity as a function of the membrane thickness based on assumptions (1) and (3).	167

List of Tables

2.3	Transport mechanisms	8
2.2	Cluster labels for nodes and links	34
4.1	The number fractions of silicon, siloxane (doubly bonded) oxygens, silanol groups and the average pore radii of the silica structures employed in the MD simulations	89
4.2	Lennard-Jones and Coulombic partial charge parameters	92
4.3	Bonded intramolecular potential parameters	93
4.4	MSD Nonlinear fitting parameter estimates	106
5.1	Chemical Reactions for SiO ₂ deposition from TEOS	121
5.2	Arrhenius Parameters for deposition reactions	122
5.3	TEOS LJ and Coulombic partial charge parameters	131
5.4	Potential parameters used for relaxation of the deposited solid films	140
6.1	Comparison of morphological properties of structures formed by etching and those computed from thin films formed via Si(OH) ₄ CVD.	162
6.2	Experimental permeances and selectivities for membranes fabricated via CVD using TEOS as precursor.	168

Chapter 1. Introduction

The increase in the concentration of CO₂ in the atmosphere over the last 200 years since the start of the industrial revolution is currently believed to be a major contributor to global warming, and the capture and storage of CO₂ has been proposed as a possible solution to this problem. Thus the separation and removal of CO₂ from large point sources such as the products of power plant combustion gases or small point sources (e.g. transport systems and/or domestic users) is a crucial step.

Bredesen et al (2004) have surveyed the possible uses of high-temperature membranes for integration into power generation cycles with CO₂ capture. They identified the following three concepts for the capture of CO₂ from power generation processes using fossil fuels:

(a) *Post-combustion capture* where the CO₂ in the exhaust gas from a standard gas turbine combined cycle or a coal-fired steam power plant is captured through physical or chemical solvents. Current processes such as amine scrubbing can only handle CO₂ separation at (relatively) low temperatures and from an exhaust gas with low CO₂ concentration. They also require large scale plant and significantly reduce the thermal efficiency of the power plant as they consume process heat.

(b) *Oxy-fuel combustion* where O₂ is used instead of air as the fuel oxidizing agent produces a flue gas primarily composed of CO₂ (and H₂O) suitable for sequestration. Flue gas recirculation of CO₂ is required to lower the combustion temperature to an acceptable level.

(c) *Pre-combustion fuel decarbonisation* where the fuel carbon is removed before combustion using, for example, gasification or natural gas steam reforming at high

temperature and pressure. The syngas (mostly H_2 and CO) can then be further treated in a water gas shift reactor, to produce CO_2 and H_2 . The CO_2 is then captured from the resulting gas by scrubbing or by other means, and generally much smaller equipment is required as the CO_2 concentration and pressure are higher.

Each of the above processes requires separation of gas mixtures. As explicitly state in (a) CO_2 is captured by separation from a stream which is largely composed of N_2 . In (b) the O_2 required must either be obtained by cryogenic distillation of air (large-scale systems such as utility scale power plant) or possibly via other techniques for smaller scale operations. In (c) the goal is to separate gas mixtures of CO_2/H_2 . One field in separations technology which is growing in importance is in the application of inorganic membranes which have the potential to provide solutions which are more energy efficient, compact, and possibly more economical than current technologies (Scholes et al (2008)).

Molecular simulation provides a means to gain an understanding of the functioning of membrane materials of the kind central to the separation technologies outlined above. Hedin et al (2010) have reviewed nanoscale sorbent materials for CO_2 capture from flue gas with emphasis on simulation results and models that been developed towards providing a theoretical basis for the functioning of these materials in CO_2 separation, particularly from N_2 -rich flue gases. Some of the silica based materials which have been investigated are zeolites and all-silica microporous solids, amine modified mesoporous silicas and MCM-41 silica.

In this thesis various aspects of diffusion in model silica systems are studied via molecular simulation with the aim of understanding the fundamental processes of diffusion in inhomogeneous systems and the mechanisms by which they can be used as membranes for adsorption and separation. In chapter 3 of this work self-diffusion within a simple fluid confined in a model nanopore qualitatively similar in structure to MCM-41 is investigated using both equilibrium and non-equilibrium simulation techniques. Recent experimental work by Belmabkhout and Sayari (2009) using pressure swing adsorption with a medium pressure desorption process has shown that MCM-41 silica could be a competitive material for CO₂ separation from industrial gases such as flue gas, biogas and syngas compared to other CO₂ physical adsorbents (such as activated carbons, zeolites and metal-organic frameworks), and has the benefit of being affordable, easily recyclable, and having thermal and mechanical stability. One of the objectives of this study is to demonstrate that linear response theory provides accurate results for the self-diffusivity in a nanopore system which is strongly inhomogeneous in the principle direction of transport. In addition, the recently developed quasi-hydrodynamic theory of Pozhar and Gubbins (1993, 1997) for confined fluids is stringently tested over a wide range of loadings with the principal objective of evaluating its ability to quantitatively predict self-diffusion within nanopore fluids.

In chapter 4 diffusion studies of CO₂, N₂ and He are undertaken for model moderate-to-high density nanoporous silica media which are considered to be representative of the barrier layers formed during composite membrane fabrication processes (e.g. via sol-gel synthesis or chemical vapour deposition). The objective in this work is to understand the nature of the transport process itself and hence the

selectivity mechanism in such media, and a model for this selectivity is proposed which follows on from prior work by the molecular simulations and experimental group at University College Dublin (MacElroy (2002), Mooney et al (2004), Cuffe et al (2006) McCann (2010) and Akter (2010)).

Finally in Chapters 5 and 6 the research is focused on one of the processing techniques now widely used in the fabrication of membranes. To date, membranes which could be used to separate gas mixtures at high temperatures (notably process gas streams at temperatures $T > 750\text{K}$) have only been developed with limited success and it is apparent that this modest pace of growth is, in part, due to a lack of a detailed understanding of the membrane fabrication process at an atomistic level. With the aim of gaining a better understanding of how process conditions affect the structures of deposited membranes, the creation of silica films via direct simulation of the CVD process at intermediate-to-high temperatures is studied, focusing on the deposition of silicic acid ($\text{Si}(\text{OH})_4$) and TEOS (tetraethoxysilane).

Before reporting on the methods employed and the outcome of this research, an overview of current developments in the literature as well as important work of historical significance is presented in next chapter.

Chapter 2. Literature Survey

2.1 Gas separation in porous membranes

In this section the basic definitions, and features of gas separation are introduced, and, in particular, the so-called ‘solution-diffusion’ approach to transport is reviewed.

The flux, J , in the x direction for gas diffusion across a membrane is given by Fick’s law as

$$J = -D \frac{dc}{dx}$$

where the driving force for diffusion is the concentration gradient dc/dx and D is the diffusivity. Taking the average gradient across the length of the membrane L , gives,

$$J = -D \frac{\Delta c}{L}$$

The permeability which is the molecular flux through a unit area of the membrane subject to a unit pressure gradient is given by,

$$P = \frac{JL}{\Delta p} = \frac{\Delta c}{\Delta p} D$$

In the SI system the units of the permeability are mol/(m.Pa.s), however the barrer unit is often found in the literature where $1 \text{ barrer} = 10^{-10} \text{ cm}^3(\text{STP})\text{cm}/(\text{cm}^2.\text{s}.\text{cmHg})$

If the sorption isotherm can be represented by Henry's law then the permeability may be expressed as the product of the solubility, S , (an equilibrium component) and the diffusivity (a dynamic component).

$$P = SD$$

The selectivity (ideal separation factor) $\alpha_{A/B}$ for a binary mixture of species A and B may be defined as

$$\alpha_{A/B} = P(A) / P(B)$$

Thus the selectivity may be due to diffusivity selectivity $D(A)/D(B)$ and/or solubility selectivity $S(A)/S(B)$. In membrane science this formalism is known (Wijmans and Baker (1995) as the solution-diffusion mechanism and is frequently used to model gas phase diffusion in these systems.

When gas mixtures permeate across a membrane, the permeation of the different species may not be independent and in this case the ideal selectivity determined from pure gas measurements may differ from the actual selectivity which will also depend on the composition and the pressure on either side of the membrane.

2.1.1 Activated diffusion

If the gas molecules are hindered by a geometric constriction then in order to make a diffusive jump over the energy barrier (activated diffusion) the gas molecule must have sufficient kinetic energy, or the atoms at the constriction must have sufficient kinetic energy to move enough to allow the gas molecule to pass.

In gas permeation the diffusion coefficient can be taken to be independent of the penetrant concentration in the membrane and the temperature dependence of the diffusion coefficient can be expressed in the Arrhenius form,

$$D_A = D_A^* \exp(-\Delta E_A / RT)$$

while the solubility coefficient is given by the van't Hoff equation:

$$S_A = S_A^* \exp(-\Delta H_a / RT)$$

where $\Delta H_a < 0$ is the enthalpy of sorption. Substituting the two equations above into Eqn. 1.4 gives the temperature dependence of the permeability,

$$P_A = P_A^* \exp(-\Delta E_p / RT)$$

where $\Delta E_p = \Delta E_a + \Delta H_a$.

Some of the various transport mechanisms (Merkel et al (2003), Rao and Sicar (1996), Way and Roberts (1992), Yampol'ski et al (2006)) of gases in porous and non-porous media are show in Table 2.1 below.

2.1.2 Molecular Sieving

For very narrow pores, selectivity is based on size (sieving mechanism) while for larger pores surface diffusion and Knudsen diffusion occur. In the case of molecular sieving, the pore width is similar to that of the gas molecules and selection is based on the kinetic diameter which is a measure of the smallest effective diameter of the molecule.

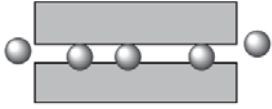
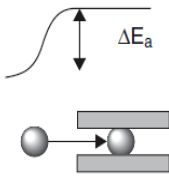
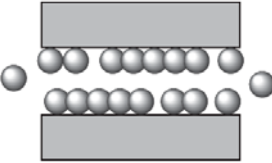
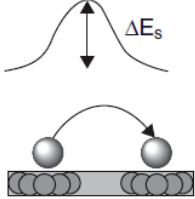
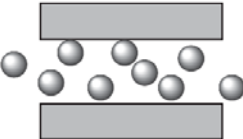
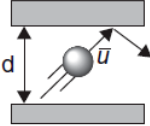
Mechanism	Schematic	Process	
Activated diffusion (size sieving)			Constriction energy barrier
Surface diffusion			Adsorption-site energy barrier
Knudsen diffusion			Direction and velocity

Table 2.1 Transport mechanisms (Thornton et al (2010))

2.1.3 Surface diffusion

For a pore size such that the gas permeability coefficient exceeds the value for free molecular flow (Knudsen diffusion), surface diffusion may become the dominant transport mechanism. Surface diffusion is a form of activated diffusion, where the energy barrier ΔE_s is the energy required for the molecule to jump from one adsorption site to the next. Gilliland et al (1974) provide the following equation for the surface diffusion coefficient

$$D_s = D_s^* \exp\left(-\frac{aq}{RT}\right)$$

where a is a proportionality constant ($0 < a < 1$) and q (> 0) is the heat of adsorption. The energy barrier between the surface adsorption sites is aq .

The gas concentration can be described by Henry's law $c = Kp$, where K depends on temperature:

$$K = K_0 \exp\left(\frac{q}{RT}\right)$$

where K_0 is a proportionality constant.

If the molecules are condensable then further layers of molecules can adsorb until the pore is entirely filled resulting in capillary condensation. In this case the condensable component can block the pores and thus have increased selectivity.

2.1.4 Knudsen diffusion

Knudsen diffusion occurs when the mean free path of the molecules in the gas phase λ is much larger than the pore diameter d . The Knudsen diffusion coefficient may be written as,

$$D_K = \frac{d}{3\tau} \bar{v}$$

where the average molecular speed, \bar{v} , is obtained from the Maxwellian distribution as,

$$\bar{v} = \sqrt{\frac{8RT}{\pi M}}$$

The flux in the Knudsen regime may be expressed as (Mulder (1996)),

$$J = n\pi d^2 \frac{\Delta p D_K}{4RTL}$$

where n is the surface concentration of the pores.

In the Knudsen regime the permeation rate of a molecule is inversely proportional to the square root of its molecular weight, so that the selectivity is given by,

$$\alpha_{A/B} = \sqrt{\frac{M_B}{M_A}}$$

2.1.5 Transition State Theory

The diffusion of molecules in porous networks such as microporous silica can be modelled by the transition state theory of Gusev and Suter (1993). In this model, illustrated in figure 2.1 below, diffusion is considered to occur as a sequence of successive infrequent jump events.

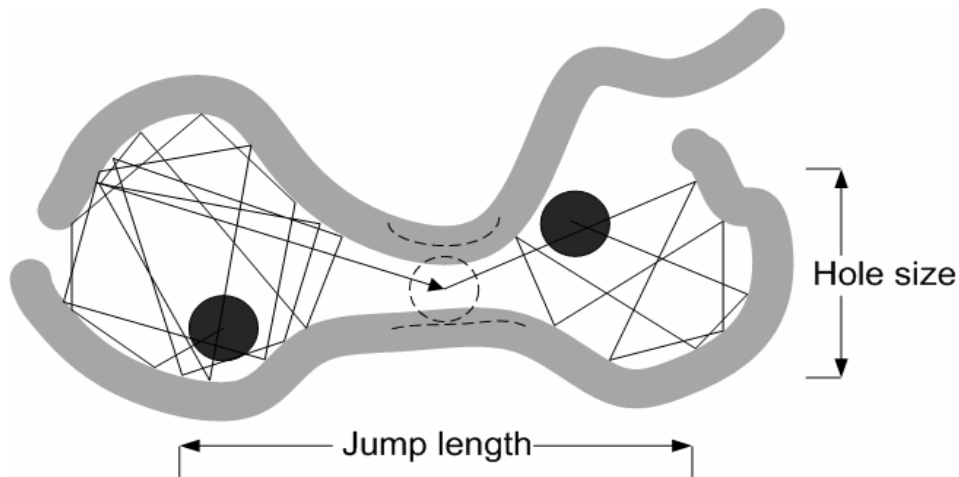


Figure 2.1. Confined motion inside a molecular matrix (adapted from Smit et al (1992)). The dashed lines indicate the opening of the tunnel which allows the diffusing molecule to jump through to the next hole.

This model allows the calculation of the diffusivity by the following method.

- (1) Through a geometric/energetic analysis of an atomistic model of the system, the states where the polymer and penetrant spend most of their time are located, and the reaction paths along which transitions between neighbouring states take place are identified;
- (2) The rate constant for each reaction path is calculated;
- (3) Reaction jumps are carried out following a Poisson process, and the diffusivity is measured by tracking the movement of the penetrant.

Smit et al (1992) were among the first to visualize jump-like motion for CO₂ inside a polyimide matrix created using a softcore method. They identified three types of motion: jumping, continuous, and trapped, and their visualization of individual trajectories showed that molecules spent long periods bouncing around inside holes at high frequency, before finally making rapid, approximately 10Å, jumps. Such jumps were assumed to occur when a tunnel was momentarily large enough to let the CO₂ pass as depicted in Figure 2.1. Thus the diffusion was determined by the slower movement of the matrix. Odagaki and Hitwari (1990) reported a similar jump mechanism at the glass transition and divided the time of the penetrant into a residence time (trapped) and flying time. Since then Gusev et. al. (1994) have found excellent agreement between TST calculations and explicit molecular dynamics simulations of Helium diffusion in bisphenol-A-polycarbonate.

The TST allows the diffusion within a porous network to be expressed as,

$$\begin{aligned}
D &= \text{the probability that the molecule will travel towards a transition } (\rho_g) \\
&\times \text{the probability that the molecule will pass through the transition } (\rho_E) \\
&\times \text{the velocity of the molecule through the transition } (u) \\
&\times \text{the jump length from the reactant cavity to the product cavity } (\lambda). \\
&= \rho_g \rho_E u \lambda
\end{aligned}$$

2.2 Overview of liquid state theory

The kinetic theory of gases was first taken from speculation to a precise mathematical formulation by Clausius and Maxwell in the middle of the nineteenth century. Following further major contributions by Boltzmann, van der Waals and Gibbs, the subject continues to be developed (though there have been lean periods) (Rowlinson (1988)) to the present day, particularly with regard to the difficult problem posed by dense inhomogeneous systems. Therefore a vast literature now exists on atomistic approaches to the theory of fluids and no attempt is made to summarise it here – however some brief remarks will be made on some issues pertinent to a sophisticated recent theory which is subjected to investigation by molecular simulation in Chapter 3 of this work. Figure 2.2 is modified from Mason and Viehland (1978) and shows the relation among the various statistical mechanical theories relevant to membrane transport (source materials to the various methods may be found in the references therein or in any of the numerous texts related to the subject (see, for example, Hansen and McDonald (2006), Boon and Yip (1980), Sone (2002), Egelstaff (1992) and Chapman and Cowling (1970))).

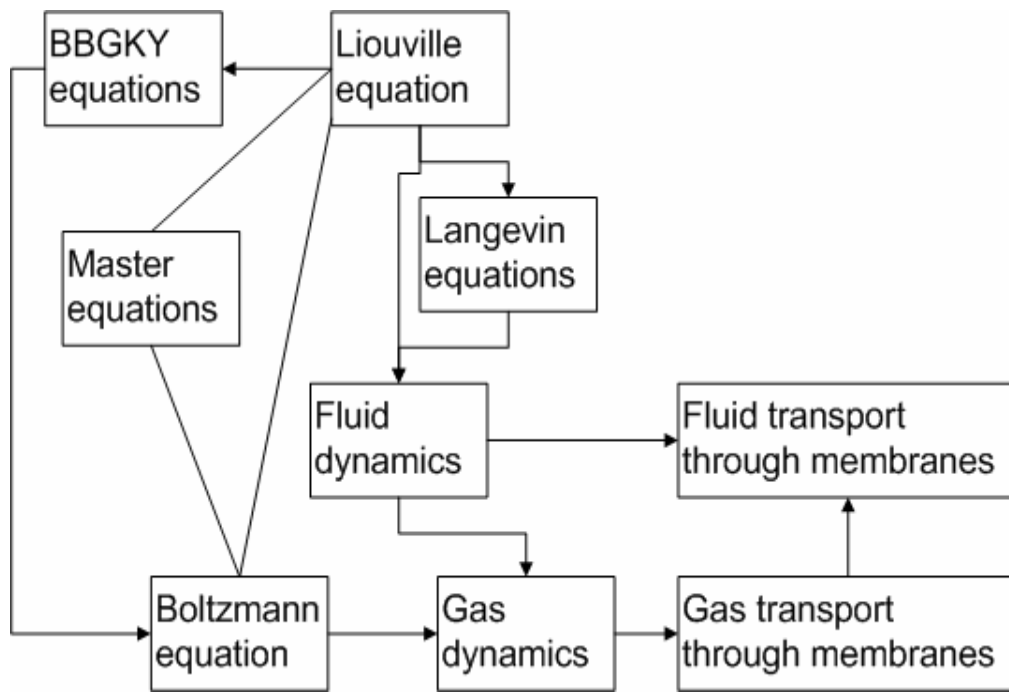


Figure 2.2 Overview of fluid theory

The theory (Pozhar and Gubbins (1993), (1997)) which is examined in Chapter 3 follows from the Liouville equation, via generalized Langevin equations to a quasi-hydrodynamical theory. It is noted here that in order to proceed from a purely mechanical, and time reversible equation such the Liouville equation, which applies to the evolution of the entire phase space, of a system of particles under classical mechanics, to a kinetic theory, many simplifying assumptions must be made. In order to extend the Enskog equation result for self-diffusion to a higher density region it is necessary to account for re-collisional effects – as a tagged particle travels through the fluid it experiences a sequence of binary collisions such as those illustrated in Figure 2.3 below. However the assumption of molecular chaos is not valid here as these sequences are correlated (Hansen and

McDonald (2006)). Other effects which become important in dense fluids include *cage diffusion* where a particle rattles around in a cage of its nearest neighbours (de Schepper and Cohen (1980), Cohen (1992)) resulting in a sequence of highly correlated collisions, and *vortex diffusion* which is caused by the backflow of momentum and energy generated by a moving particle which gives rise to so-called ring collisions.

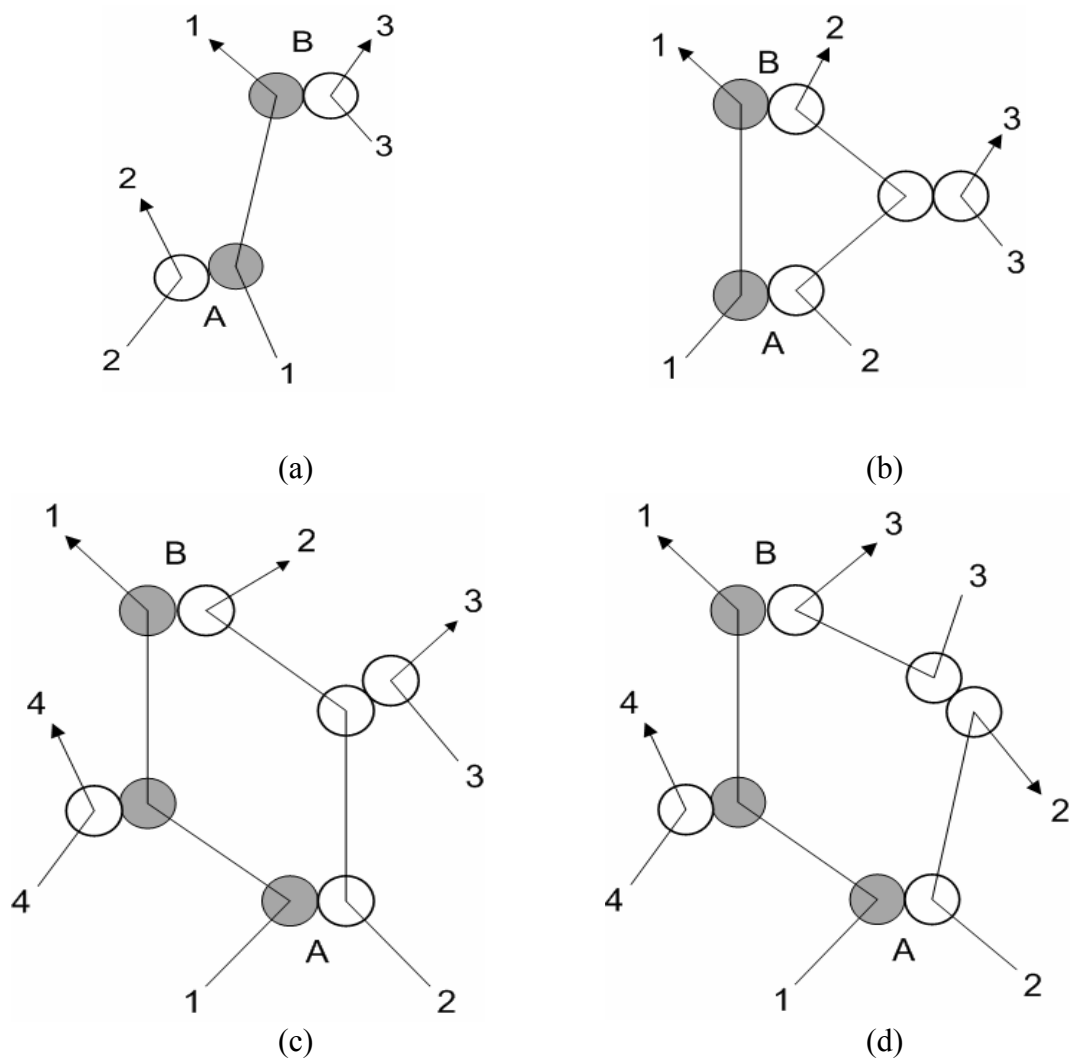


Figure 2.3 Examples of some binary collision types (a) correlated, (b, c, d) uncorrelated (from Hansen and McDonald (2006))

2.3 Lattice diffusion

Pandey et al. (1984) carried out MC simulations for classical diffusion (random walks) on simple cubic lattices (the so called “ant-in-the-labyrinth”). They studied systems below, at, and above the percolation threshold and confirmed the validity of the scaling theory approach of Gefen et al. (1983) who derived the following equation for the mean squared displacement of a walker on a percolation cluster containing s sites

$$\langle r^2(t) \rangle_s = A^2 t^{2/(2+\theta)}$$

based on a scaling description of the diffusion coefficient $D_s = 1/2 \times d \langle r^2(t) \rangle_s / dt$. This result which is valid below and above the percolation threshold implies that the effective dimensionality (Hughes et al (1981)) of the random walk is $d_{\text{rw}} = 2 + \theta$ (for Fickian diffusion the value is $d_{\text{rw}} = 2$). Roman (1990) has extended the MC simulations to larger systems and Condamin et al (2008) have developed a theoretical framework that allows the calculation of mean first-passage times, splitting probabilities, and occupation time distributions in disordered media. These tools make it possible to discriminate between the two possible microscopic mechanisms of sub-diffusion in disordered media considered by the authors, which were diffusion on fractals and continuous time random walks with long tailed waiting times.

2.4 Simulation

2.4.1 Molecular dynamics

The classical molecular dynamics method essentially involves propagating a system of particles to give a trajectory which obeys the laws of classical mechanics. Newton's law relating the acceleration to the force on particle i is given by

$$m_i \ddot{\mathbf{r}}_i = \mathbf{f}_i$$

The force on particle i due to its interactions with the other particles in the system is given by taking the gradient of the potential energy with respect to the coordinates of particle i ,

$$\mathbf{f}_i = -\nabla_{\mathbf{r}_i} V$$

where V is the potential energy of the system which is a function of the configuration of the entire system. Modern computer algebra systems make checking that the correct functional form has been derived for the force a trivial matter.

The equations of motion are solved numerically using an integration scheme such as the velocity Verlet method

$$\mathbf{r}(t + \delta t) = \mathbf{r}(t) + \delta t \mathbf{v}(t) + \frac{1}{2} \delta t^2 \frac{\mathbf{f}(t)}{m}$$

$$\mathbf{v}(t + \delta t) = \mathbf{v}(t) + \frac{\delta t}{2m} [\mathbf{f}(t) + \mathbf{f}(t + \delta t)]$$

The algorithm is implemented in two stages during each time step δt : firstly, the new positions at time $t + \delta t$ are found using the first of the above expressions and the velocities at mid-step are calculated using

$$\mathbf{v}(t + \frac{1}{2}\delta t) = \mathbf{v}(t) + \frac{\delta t}{2m}\mathbf{f}(t)$$

The forces at time $t + \delta t$ are then computed, since the positions $\mathbf{r}(t + \delta t)$ are known, and the velocity move is completed

$$\mathbf{v}(t + \delta t) = \mathbf{v}(t + \frac{1}{2}\delta t) + \frac{\delta t}{2m}\mathbf{f}(t + \delta t)$$

Although simple, the velocity Verlet algorithm is perfectly suitable for most MD applications where extremely accurate trajectories are not the goal as the systems are usually chaotic and thus trajectories diverge exponentially from the true trajectory. It also possesses the important property that it is time reversible, and has the property that it preserves the phase space volume as required by Hamiltonian dynamics where Liouville's theorem requires that the phase space flow be incompressible. Such phase space volume preserving algorithms are at least compatible with the absence of long term energy drift (Frenkel and Smit (2002)). Considerable advances have been made in deriving rigorous time reversible algorithms using the Liouville formulation (Tuckerman et al (1992)) including algorithms formulated for constant pressure/temperature ensembles. The state of the art in MD integrators, so called geometric integrators which exactly satisfy conservation laws have been described in the book by Leimkuhler and Reich (2004).

2.4.2 Kinetic Monte Carlo

The kinetic Monte Carlo method was first developed by Bortz et al (1975), and independently by Gillespie (1977) though basic features of the method were also used by Young and Elcock (1966) and Beeler (1966). The method was placed on a rigorous foundation by Fichtorn and Weinberg (1991) though it was widely used before then and continues to be an important method due to its ability to simulate processes where the timescales are well beyond those that can be reached by other methods such as molecular dynamics. A general overview of the method is given by Voter (2005).

Unlike the standard (Metropolis) Monte Carlo, where events are chosen at random and then may be rejected by considering the Boltzmann factor of the energy difference (Allen and Tildesley (1987)), in KMC the events are chosen not at random but in proportion to the frequency at which they occur. The method thus requires as input, the rates of the events which are to be considered.

2.4.2.1 Bortz-Kalos-Lebowitz algorithm

For reference purposes with the version of the KMC algorithm employed in this work and which will be described later in Chapter 5, the general outline of the so called ‘n-fold way’ algorithm of Bortz et al (1975) is given in this section. The Bortz-Kalos-Lebowitz KMC algorithm allows the propagation of a system from its current state to the next possible state assuming that the transfer rates between the initial state and all possible subsequent states are known. The general form of the algorithm for simulating the time evolution of a system where some processes

can occur with known rates r may be written as:

1. Set the time $t = 0$;
2. Form a list of all possible rates in the system r_i ;
3. Calculate the cumulative function $R_i = \sum_{j=1}^i r_j$ for $j = 1, \dots, N$ where N is the total number of transitions;
4. Get a uniform random number $u \in [0,1]$;
5. Determine the event to carry out i by finding the i for which $R_{i-1} < uR_N \leq R_i$;
6. Carry out event i ;
7. Recalculate all rates r_i which may have changed due to the transition. If appropriate, add new transitions i . Update N accordingly;
8. Obtain a new uniform random number $u' \in [0,1]$;
9. Update the time with $t = t + \Delta t$ where $\Delta t = R_N^{-1} \ln(1/u')$;
10. Recalculate all rates r_i which may have changed due to the transition. If appropriate, add new transitions i . Update N and the list of events accordingly;
11. Return to step 2.

2.4.2.2 Applications to deposition

Battaile and Srolovitz (2002) have reviewed some of the major approaches using KMC for modelling chemical vapour deposition (CVD) though their focus is on lattice methods applied to diamond CVD. Clarke et al (1996) developed a hybrid KMC/MC off-lattice method for diamond CVD. Schumacher et al (2006) have developed an off-lattice KMC procedure for modelling the silica sol-gel process in the presence of templating micelles.

2.4.3 Tricks of the trade

2.4.3.1 Periodic Boundary Conditions and Minimum Image Convention

As only a finite number of particles can be simulated it is necessary to have appropriate boundary conditions so that the simulated system is not dominated by boundary effects and matches as closely as possible the physical system being modelled. For this reason periodic boundary conditions are frequently employed: in three dimensions to model a bulk system, in two dimensions to model surfaces, and in one dimension to model infinitely long channels. The simulation box is replicated throughout space in the periodic dimensions so that the coordinates of particles in the replica cells are computed from the central cell coordinates by adding or subtracting integral numbers of box lengths.

In addition to periodic boundary conditions it is usual to apply the minimum image convention. As illustrated in Figure 2.4, in this convention atom i in the central cell is assumed to interact with only the closest one, of the infinitely many images of any other particle. There are many ways of implementing periodic boundary conditions, for example considering the x component of a position vector (or the x component of a separation vector) one can use,

$$x = x - L_x \times \text{anint}(x / L_x)$$

or

$$\text{if } \left(\text{abs}(x) > \frac{L_x}{2} \right) x = x - \text{sign}(L_x, x)$$

where $\text{anint}(A)$ returns the nearest integer to A , and $\text{sign}(A,B)$ returns A with the sign of B are standard Fortran functions. Although these and other forms (Allen and Tildesley (1987)) are equivalent, the speed of compiler implementations can vary considerably, and considering that the PBC calculation of distances and separation vectors usually takes place at the heart of deeply nested force or energy calculation loops, the particular method chosen can have a significant impact on the simulation speed. For this reason it is worthwhile implementing the PBC calculation as a function which compilers can be instructed to inline aggressively (thus removing the function call overhead), and the various forms can then be tested for speed by simply changing the definition of the PBC function.

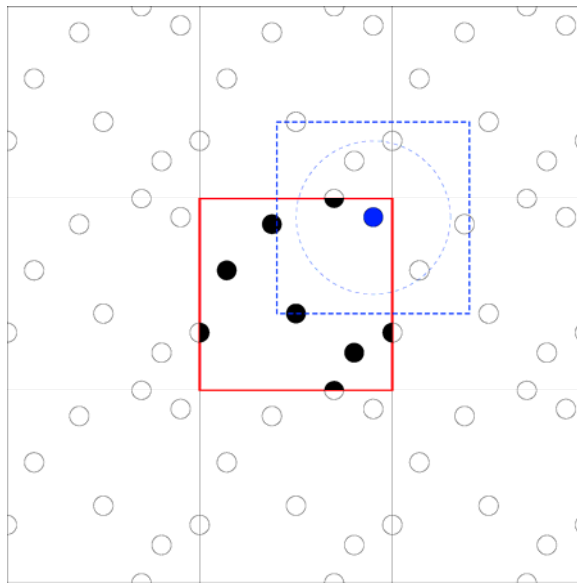


Figure 2.4. Schematic showing periodic boundary conditions in 2D. The dashed blue box illustrates the minimum image condition; the particles in this box, which is centred on the blue particle, are the minimum image neighbours of the blue particle.

2.4.3.2 Truncated Potentials

In the minimum image convention the calculation of the pair-wise forces between particles involve $N(N-1)/2$ terms, which for a given simulation box can be a large number. If the forces are short ranged, i.e. if the potential function is approximately zero at some distance r_c , then if r_c is much less than the length of the box, one can save considerable time by only considering those pairs of atoms which are within a distance r_c of each other. In this case it is usual to truncate the short range potential so that $u(r) = 0$ for $r \geq r_c$, and a spherical cutoff is then applied at the cutoff distance r_c .

Such a cutoff introduces a discontinuity where the potential function is abruptly truncated at distance r_c (which can cause problems, especially in molecular dynamics calculations where energy conservation is required) which can be removed by shifting the potential function $u(r)$ by $u(r_c)$ giving

$$u^s(r) = \begin{cases} u(r) - u(r_c) & r \leq r_c \\ 0 & r > r_c \end{cases}$$

Although the above potential is suitable for Monte Carlo simulations where only the energy needs to be calculated, the shifted potential still contains a discontinuity in its first derivative with respect to r so that the force between two particles at separation r_c is discontinuous. This can cause instability in the solution of simulation trajectories, and to avoid this a linear term can be added which makes the force zero at the cutoff giving the shifted force potential,

$$u^{\text{SF}}(r) = \begin{cases} u(r) - u(r_c) - \frac{du(r)}{dr} \Big|_{r=r_c} (r - r_c) & r \leq r_c \\ 0 & r > r_c \end{cases}$$

Note that the above potentials are not the real potentials, though the thermodynamic properties of fluids with the original potential can be recovered from simulation results for the shifted force potential (Powles (1984), Nicholas et al (1979)). For systems with many different atom types, switching functions are often used instead (Leach (2001)). The various switching function forms are not relevant to this work and details can be found in many of the now standard texts on molecular simulation (Leach (2001), Schlick (2010)).

2.4.3.3 Verlet list

Verlet (1967) introduced a bookkeeping technique to skip those pairs of atoms separated by a distance greater than r_c which can be ignored when the potential is cutoff at r_c . For each atom i the list maintains a list of neighbouring atoms (the non-bonded neighbour list) within a distance r_v of i . The Verlet radius r_v is greater than the cutoff radius r_c such that the cutoff sphere around each atom is surrounded by a skin of thickness $r_v - r_c$ as shown in Figure 2.5(a).

The thickness of this skin should be such that the neighbour list does not have to be updated too frequently, and should be thick enough such that a particle just outside the outer skin such as the red atom labelled g in Figure 2.5(a) will not cross the skin and enter the inner cutoff sphere between updates to the neighbour list. There are many improvements to the basic algorithm, for example allowing

the automatic updating of the list, and the selection of the optimum skin thickness, such as those by Thompson (1983) and Chialvo and Debenedetti (1991).

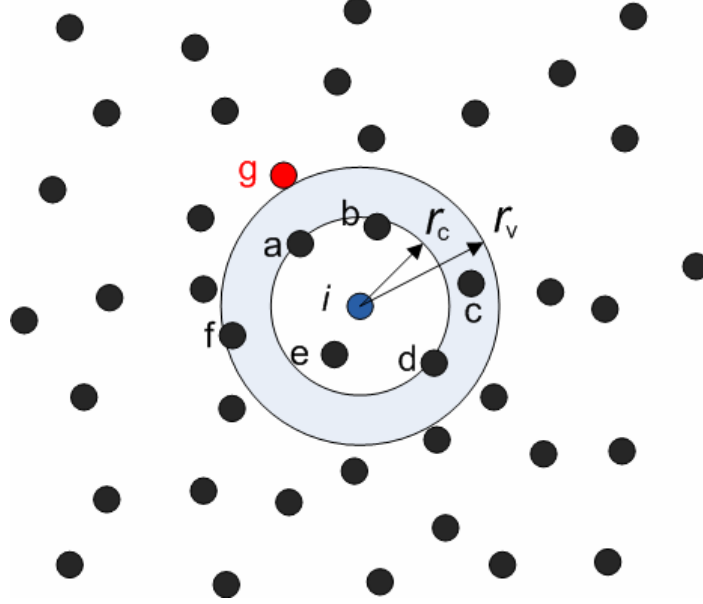


Figure 2.5(a) The Verlet neighbour list for atom i .

The neighbour list may be conveniently stored in two one dimensional arrays as shown in Figure 2.5(b) (a two dimensional array can also be used). The pointer array P stores atom indices for the neighbour list array L , such that $P(i)$ points to the position index in L where the first atom in the neighbour list of atom i is stored, and the last element in the neighbour list for atom i is stored in $P(i+1)-1$, so the neighbours of atom i are stored in the slice $L(P(i):P(i+1)-1)$. For the case where atom i in Figure 2.5(a) is actually $i = 1$, Figure 2.(b) shows the storage in L of the neighbour list includes atoms a, b, c, d, e, f. While looping through the neighbour list to calculate the force on atom $i = 1$, all 6 neighbours are considered, though only those less than r_c (a,b, and e) at a given step actually contribute. For

the case where all atom pairs are considered at each step such as in the molecular dynamics method, where Newton's third law can be used to obtain the force on i due to j at the same time as the force on j due to i , some storage space can be saved by only considering the neighbours j of i where $j > i$ as $j < i$ will appear in the neighbour list for j . In the Monte Carlo method this is not possible as atoms i and j move independently and the neighbour list for i must contain all its neighbours.

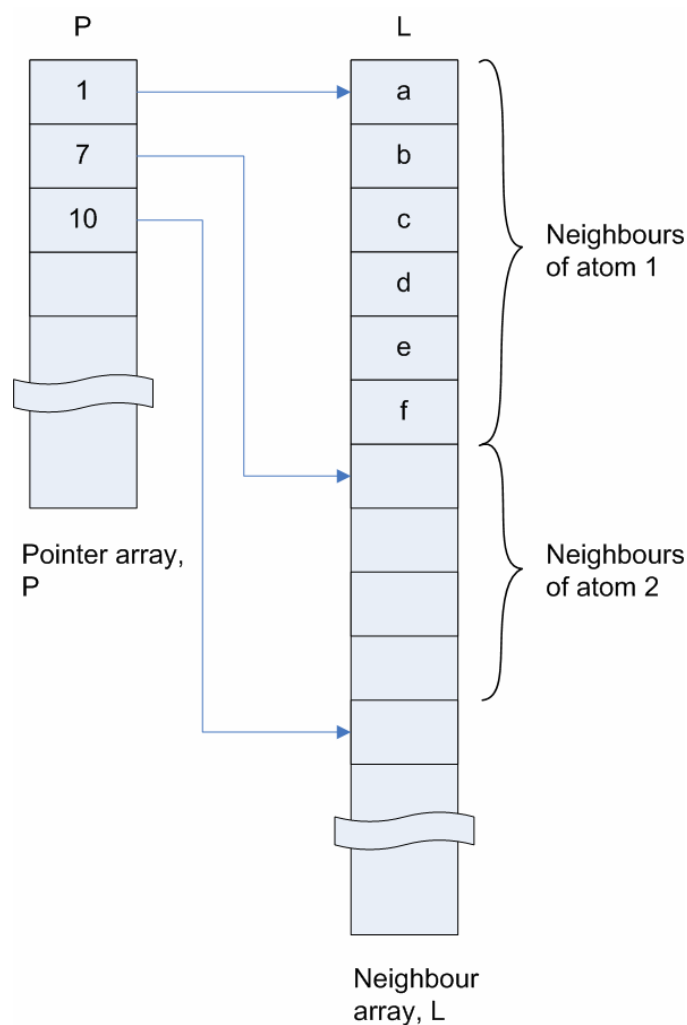


Figure 2.5(b) Two one dimensional arrays for storing the Verlet neighbour list.

2.4.3.4 Cell linked lists

The cell linked list method introduced by Hockney and Eastwood (1981) is useful for systems where the number of particles N is large as it scales with $O(N)$. It may be used on its own, or combined to speed up the otherwise slow $O(N^2)$ update step for the Verlet list considered above, where, if the size of the system is much larger than the cutoff distance r_c , then the cell link will be much faster. The cell list method involves dividing the box into cells of width equal to or slightly larger than the cutoff distance r_c as shown in Figure 2.6(a) below. Each particle in a cell now only interacts with particles in the same cell, and its neighbouring cells; this is illustrated in Figure 2.6(a) where atom i is at the centre of cell number 13 and its cutoff sphere is represented by the dashed red circle, while the light blue circles represent the cutoff spheres for particles placed at the extreme positions of the corners of the cell. It can be seen that only the shaded central cell 13, and its neighbours (7, 8, 9, 12, 14, 17, 18, 19) need to be considered as long as the cell width is at least equal to the cutoff distance.

To calculate the interaction on particle i one therefore needs a way to store the lists of atoms in the cells: this may be done using a linked list structure which is illustrated in Figures 2.6 (b) and 2.6(c) below. The linked list can be implemented using two one-dimensional integer arrays (Allen and Tildesley (1987)), a pointer (index) array called *HOC* (“Head Of Chain”), and a linked list array, *LL*. *HOC*(i) stores the number of the “first” atom in cell i . *HOC*(i) is then used to index *LL*, so that *LL*(*HOC*(i)) is the number of the next atom stored in the cell list, and each element of *LL* gives the index of the next atom stored in the cell list. It is therefore possible to iterate over the atoms in a cell by following the list of linked list

references, until the last element is reached (which links to zero) as illustrated in Figures 2.6(b) and 2.6(c).

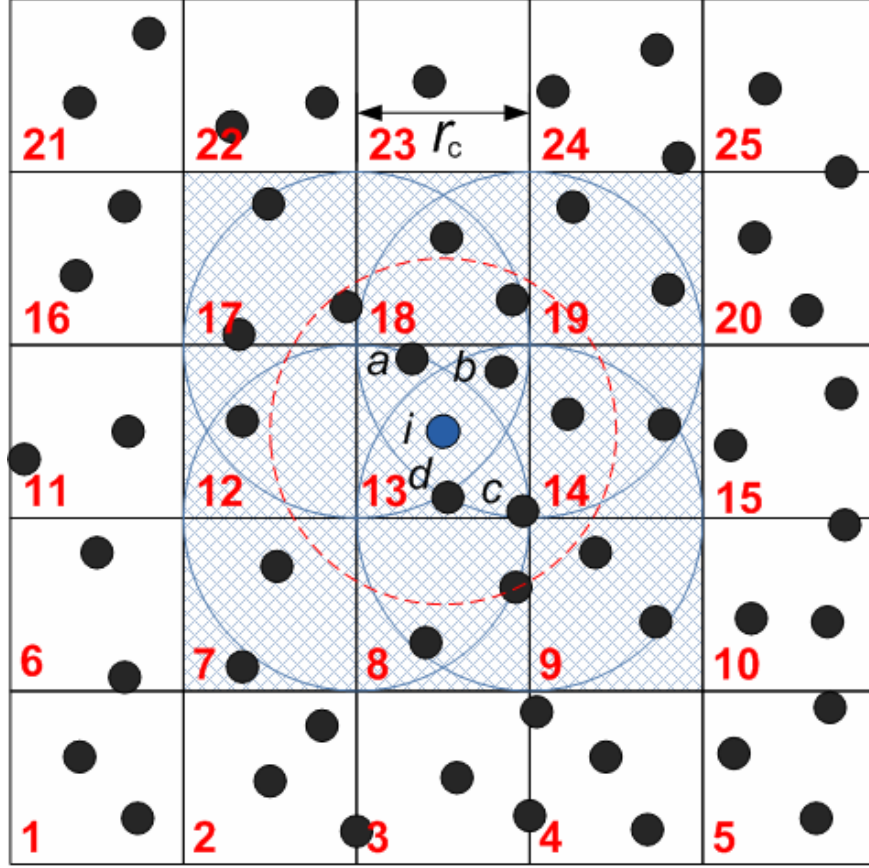


Figure 2.6(a) Two dimensional illustration of the cell list: the simulation box is divided into 25 cells of width r_c such that particle i in a given cell only interacts with particles in the same cell and neighbouring cells. The cell numbers are the red numbers in the bottom left hand corner of each cell. The central cell number 13, contains atoms i , a , b , c , and d , where atom number $i > d > c > b > a$ so that when the list of atoms in the cell is constructed i is added last and is thus the number of the pointer ($HOC(13) = i$) into the list of atoms in the cell as shown in figure 2.6(b).

As in the case of the Verlet list, for molecular dynamics it is possible to traverse both the cells and the linked lists within them in such a way that interaction ij need only be calculated once (Allen and Tildesley (1987)). As noted above, the cell list method may be combined with the Verlet list to improve performance – Frenkel and Smith (2002) provide further analysis of the relative speeds, of the Verlet list, cell list, and a combination of the two for various numbers of Lennard-Jones particles.

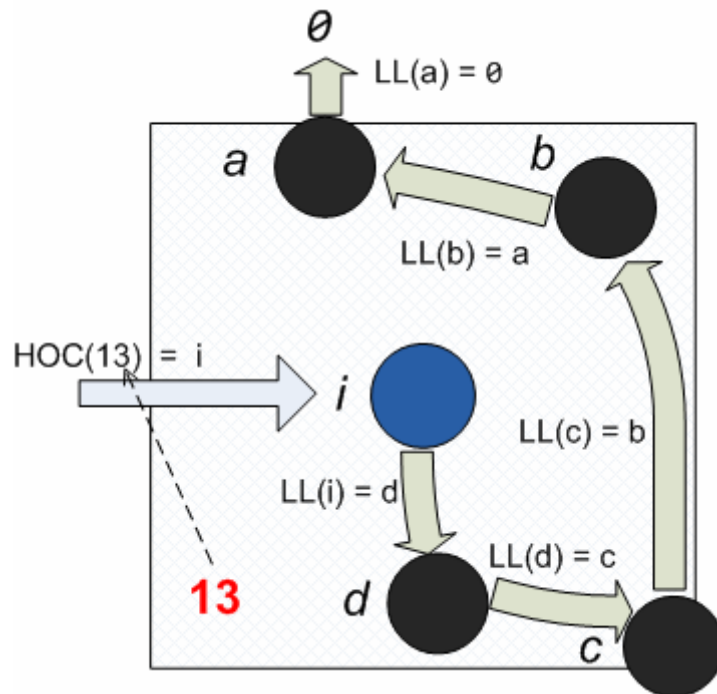


Figure 2.6(b) Linked list chain of atoms in cell. The storage of the list of atoms in cell 13 of figure 2.6 (a) is illustrated. *HOC*, the “head of the chain” for cell 13 points to atom i . The remaining atoms are then found by following the linked list LL for the remaining atoms in the cell, until the terminating atom (which points to zero) is reached.

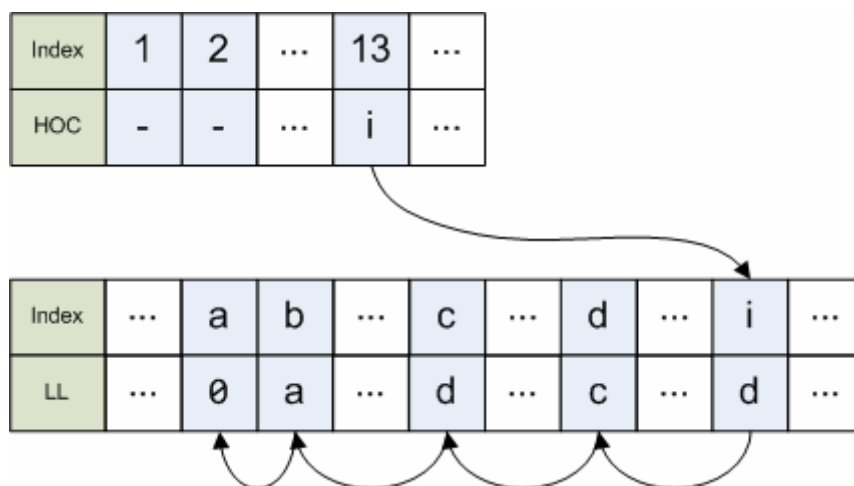


Figure 2.6(c) Linked list data structure showing the storage of the linked list of atoms in cell 13, as shown in figure 2.6 (a).

2.4.3.5 Long-range Forces - Electrostatics

A broad literature already exists on methods for handling the long range nature of the electrostatic interactions. It would not be relevant to summarise them here, as recent survey articles exist (see Karttunen et al (2008), Koehl (2006)). Instead, some of the most important recent work is mentioned and some brief comments are made on some aspects of methodology which will be covered again in later chapters.

Hedman and Laaksonen (2006), developed a highly efficient (scaling as $O(N \log N)$) algorithm combining aspects of the traditional Ewald method and the Fast Fourier Transform, yielding the so-called ENUF (Ewald with Non-Uniform Fourier) method. The method conserves both energy and momentum and would appear to be the current state of the art. Other notable work includes the method developed by Lekner (1989) and extended by Grønbech-Jensen and co-

workers (Grønbech-Jensen (1997), Grønbech-Jensen et al (1997)), and the so called MMM2D method of Arnold and Holm (2002) for two dimensionally periodic systems.

If for reasons of computational necessity, a simple Coulomb potential with the minimum image convention is used, then electroneutral group based cutoffs should be used (Leach (2001)). Recently there has been much development (e.g. Fennell and Gezelter (2006), Carré et al (2007)) of ideas originally proposed by Wolf (1999) allowing the use of short range cutoff approaches to be applied for the electrostatics in disordered systems – this will be covered further in Chapter 5.

In the case where dummy point charges are used, where the position of the point charge is a function of the coordinates of other atoms, then it is necessary to transfer the force on the dummy charge back to the atoms from which its coordinates are derived. For the general case, the x-component of force on atom i due to the force on dummy atom d is given by (Feenstra et al (1999),

$$\mathbf{F}'_{ix} = -\frac{\partial \mathbf{r}_d}{\partial x_i} \frac{\partial V}{\partial \mathbf{r}_d} = \frac{\partial \mathbf{r}_d}{\partial x_i} \mathbf{F}_d$$

2.4.3.6 Hoshen-Kopelman Algorithm

The original Hoshen and Kopelman (1976) algorithm allows the efficient labelling of clusters on a regular network of cells which may be either occupied or unoccupied, where labelling means identifying the clusters of contiguous occupied cells and giving each cell a number which identifies the cluster it belongs to.

2.4.3.7 Non-Lattice Hoshen-Kopelman Algorithm

Al-Futaisi and Patzek (2003) developed a generalization of the original HK algorithm to non-lattice environments which can be used for continuum systems or disordered networks. By using general data structures for describing the network connectivity (which are presented below) the algorithm can handle any arbitrarily connected bonds and sites on any lattice or non-lattice environment of any dimensionality.

The algorithm is illustrated by showing the result of its application to a simple network of 16 nodes and 24 links as given by Al-Futaisi and Patzek (2003) and shown in Figure 2.7(a) below.

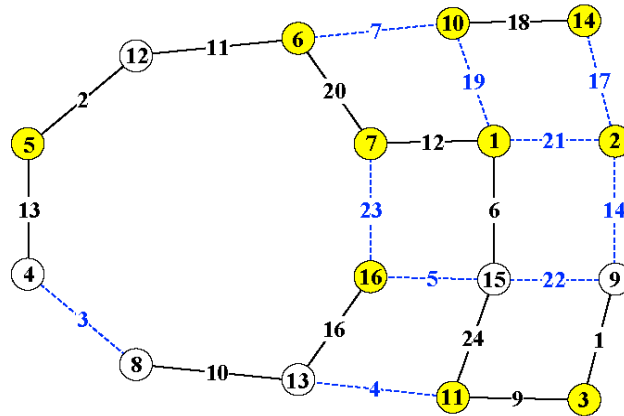


Figure 2.7(a). Simple network of 16 nodes and 24 links (redrawn from Fig. 1 of Al-Futaisi and Patzek (2003)). The yellow disks and full black lines represent occupied nodes and links respectively, while the white disks and dashed blue lines represent empty nodes and links. Each disk/line is labelled with its node/link number.

It can be seen from Figure 2.7(a) that both nodes and links may be either occupied or empty. The six data structures needed to fully describe this network are:

(1) the array of node numbers

$$Node = (1, 2, 3, 4, 5, 6, 7, 8, 9, 10, 11, 12, 13, 14, 15, 16),$$

(arbitrary labels, although shown here as increasing numbers this is not required), and

(2) the occupancy of each node

$$NodeS = (1, 1, 1, 0, 1, 1, 1, 0, 0, 1, 1, 0, 0, 1, 0, 1)$$

where $NodeS(i)$ is 1 if node i is occupied and 0 if it is empty.

(3) the link numbers (again, arbitrary labels)

$$Link = (1, 2, 3, 4, 5, 6, 7, 8, 9, 10, 11, 12, 13, 14, 15, 16, 17, 18, 19, 20, 21, 22, 23, 24)$$

and

(4) the occupancy of each link (again 1 if occupied and 0 if empty)

$$LinkS = (1, 1, 0, 0, 0, 1, 0, 0, 1, 1, 1, 1, 0, 0, 1, 0, 1, 0, 1, 0, 0, 0, 1)$$

Next one requires two data structures to describe the connectivity of the network, they are (5) *NodeNext* which stores the connectivity of the nodes, and (6) *LinksOfNode* which stores the links which are attached to each node. *NodeNext* (see overleaf) is a connectivity array of dimension number of nodes by maximum connectivity or coordination number (4 in this network) such that forrow i , $NodeNext(i,:)$ contains the neighbour nodes of node i and $NodeNext(i,j)$ is set to zero for j greater than the maximum connectivity of node i . For example *node* 3 has two neighbour *nodes* 11 and 9 corresponding to row 3 (11, 9, 0, 0) of *NodeNext*.

$$\begin{array}{l}
NodeNext = \begin{bmatrix} 7 & 15 & 2 & 10 \\ 1 & 9 & 14 & 0 \\ 11 & 9 & 0 & 0 \\ 8 & 16 & 5 & 0 \\ 4 & 7 & 12 & 0 \\ 12 & 7 & 10 & 0 \\ 5 & 6 & 1 & 6 \\ 13 & 4 & 0 & 0 \\ 15 & 3 & 2 & 0 \\ 6 & 1 & 14 & 0 \\ 13 & 3 & 15 & 0 \\ 5 & 6 & 0 & 0 \\ 8 & 11 & 16 & 0 \\ 2 & 10 & 0 & 0 \\ 16 & 11 & 9 & 1 \\ 4 & 13 & 15 & 7 \end{bmatrix}
\end{array}
\qquad
\begin{array}{l}
LinksOfNode = \begin{bmatrix} 12 & 6 & 21 & 9 \\ 21 & 14 & 17 & 0 \\ 9 & 1 & 0 & 0 \\ 3 & 8 & 13 & 0 \\ 13 & 15 & 2 & 0 \\ 11 & 20 & 7 & 0 \\ 15 & 23 & 12 & 20 \\ 10 & 3 & 0 & 0 \\ 22 & 1 & 4 & 0 \\ 7 & 19 & 18 & 0 \\ 4 & 9 & 24 & 0 \\ 2 & 11 & 0 & 0 \\ 10 & 4 & 16 & 0 \\ 17 & 18 & 0 & 0 \\ 5 & 24 & 22 & 6 \\ 8 & 16 & 5 & 23 \end{bmatrix}
\end{array}$$

The *LinksOfNode* array has the same dimensions as *NodeNext* and its rows are stored in the same order, so for example, taking row 3 of *LinksOfNode* (9,1,0,0), it is seen that *node* 3 has two neighbour *links*, 9 and 1.

The application of the clustering algorithm results in seven clusters shown in Table 2.2 below and depicted in Figure 2.7(b).

2.4.4 Model silica systems

2.4.4.1 Overview of Force Fields

There have been a number of review articles on the available silica potentials including a major review of the available potentials for silicon and all forms of silicon dioxide by Schaible (1999), a comparative study of realistic models for

Cluster	Nodes	Links
1	1, 6, 7	6, 11, 12, 20
2	2	
3	3, 11	1, 9, 24
4	5	2, 13
5	10, 14	18
6	16	16
7		10

Table 2.2 Cluster labels for nodes and links as shown in Figure 2.7(b) for the network shown in Figure 2.7(a)

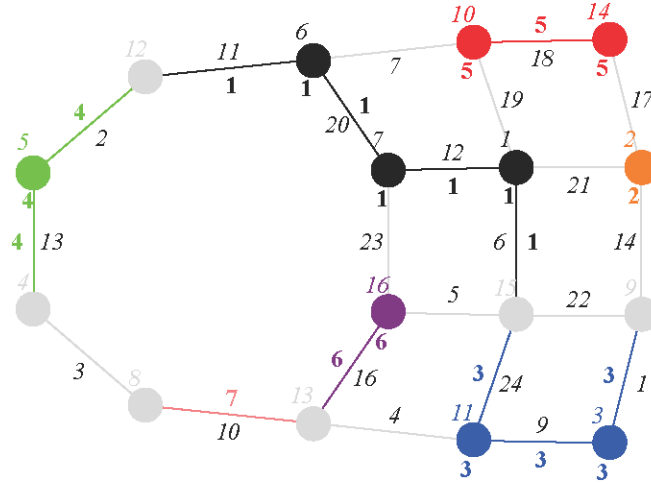


Figure 2.7(b). The labels which have been assigned to the network by the non-lattice Hoshen-Kopelman algorithm. Each occupied node and link is given a unique colour depending on the cluster it belongs to. The **bold** coloured labels give the cluster numbers of the nodes and links while the *italic* labels are the node/link numbers. The light grey elements are empty (nodes or links) and so have no cluster numbers.

amorphous silica by von Alfthan et al (2003), and a comparison of potentials for molecular dynamics simulation of silica by Herzbach and Binder (2005). The complexity of amorphous silica is due in part to the dual ionic/covalent nature of the SiO bond where the ionic nature of the bond has been taken to be between 40% (Brucker (1997)) and 50% (Catlow and Cormack (1987)). Many of the available potentials do not have an explicit covalent component (i.e. they lack explicit bond stretch and bond angle bending terms) but may include a three-body term to handle the covalent bending and stretching, however even with the addition of a three-body term defects (over coordination or under coordination) are allowed. If a fully coordinated structure with no defects is required then the Keating type potential form assessed by von Alfthan et al (2003) is required. von Alfthan et al found that the Keating potentials they studied did not give realistic descriptions of amorphous silica, particularly with regard to matching the experimental Si-O-Si bond angle distribution. However, they provided a reparameterization which, they concluded was able to create amorphous silica models with the WWW (Wooten et al (1985)) method which had realistic short and medium range structure.

2.4.4.2 Simulation applications

Gulmen and Thompson (2006) developed a method for creating model silica pores with controllable surface chemistry in that they allowed the total surface OH density and its component densities S1 (silanol groups) and S2 (silanediol or germinal groups) to be tuned. The method involved annealing a sample of molten SiO₂ around a “repulsive resist” which was a collection of purely repulsive “bead”

particles which were arranged to form a cylindrical template. The SiO₂ was modeled using the following modified form of the BKS (van Beest et al (1990)) potential

$$V = \alpha e^{-\beta r/r_m} - \frac{\gamma}{[(r/r_m)^2 + d^2]^3}$$

The original BKS potential is of Born-Mayer form $V = Ae^{-Br} - C/r^6$ which diverges to $-\infty$ as $r \rightarrow 0$. The modified form above preserves the well depth and the position of the minimum but introduces a steeper repulsive wall and a slight distortion to the long range attraction. It was found that $d = 0.2$ was sufficient to prevent unphysical collapse at 8000K.

The repulsive bead had a potential form of $V = C_{12}/r^{12}$ with the C_{12} parameter chosen so that the interaction of the bead and silica atoms at the intended surface would be less than $k_B T$ at room temperature. In order to tune the OH surface concentration of the resulting silica pores certain SiO bonds were selected for hydrolysis. To achieve OH surface tuning two parameters were considered: r_s a cutoff value for the radius from the centre of the pore which was taken to control the depth of H₂O penetration and r_b the length which an SiO bond length must be greater than for it to be considered for hydrolysis i.e. the most stressed SiOSi unit bonds are cleaved to form additional OH groups. This method allowed a wide range of OH surface types (OH concentrations of 0.6nm⁻²-4.7nm⁻²) to be produced with densities of 2.26 g/cm³ with a standard deviation of ~0.25 g/cm³ extending into the interior of the silica.

2.4.5 Characterisation of free space

2.4.5.1 Pore Size Distribution

Lastoskie and Gubbins (2001) have reviewed the characterization of porous materials using molecular theory and simulation, and found that model disordered adsorbents created using quench molecular dynamics simulations had pore size distributions that closely resembled those of actual porous glasses. They defined the pore volume function $V(r)$ as the volume of void space “coverable” by a sphere of radius r . A point X is in $V(r)$ if one can construct a sphere of radius r that overlaps X but does not overlap any of the pore atoms. Figure 2.8 below shows a two dimensional representation of the geometric derivation of the pore size distribution; points in the narrower regions of the pore are only accessible to smaller spheres (than in the wider regions), however for a given point, P , by determining the largest spheres which can cover this point, the cumulative pore volume curve can be obtained.

This is equivalent to the volume of void space enclosed by the pores’ “Connolly surface” (Connolly (1983)). $V(r)$ is equivalent to the cumulative pore volume and dV/dr is the fraction of volume coverable by spheres of radius r but not $r + dr$ and is therefore a direct definition of the pore size distribution,

$$P(r) = -\frac{dV(r)}{dr}$$

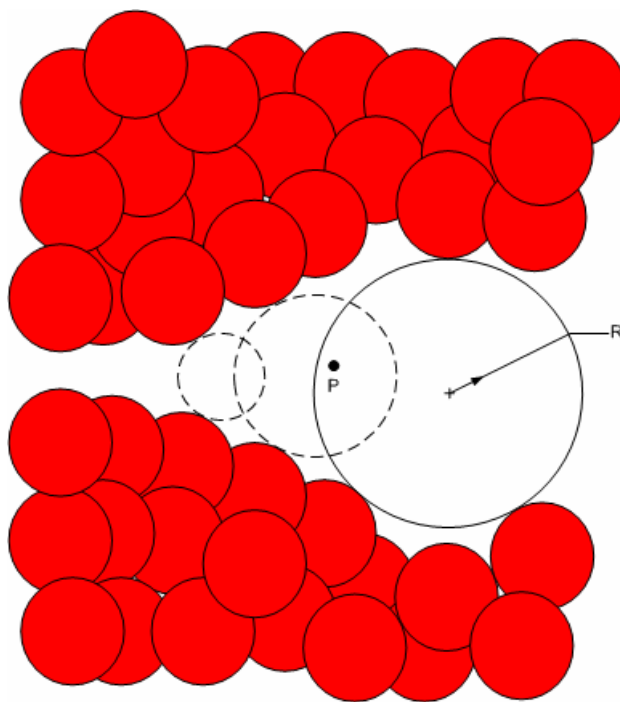


Figure 2.8. Definition of the pore size used by Bhattacharya and Gubbins (2006). The pore wall atoms are the red disks. The circle shown with radius R represents the largest sphere covering point P in the pore.

The pore volume function $V(r)$ may be determined by a Monte Carlo volume integration (Allen and Tildesley (1987)) as used by Gelb and Gubbins (1999) where the calculated geometric pore size distributions for models of porous Vycor glass were compared with pore size distributions extracted from simulated adsorption isotherms in order to determine how the geometric definition could be related to the experimental pore size distributions determined from adsorption isotherms. The adsorption isotherms were generated using the Grand Canonical Monte Carlo procedure (Norman and Filinov (1969), Adams (1975), Nicholson and Parsonage (1982) and Frenkel and Smit (2002)) and the pore size distributions were extracted from the isotherms using a slightly modified form of the Barrett-

Joyner-Halenda method (Barrett et al (1951)). For the systems considered (porosities near 30% and pore sizes of approximately 3.3, 3.9, 4.5, and 5.0 nm diameters) it was found that the adsorption isotherm derived distributions had peaks located at approximately 1 nm smaller diameters, with the isotherm derived peaks also tending to be narrower and the pore size distributions noisier than the geometric curves. The authors concluded that the close agreement of the two methods was exceptional considering the complexity of the pore geometry and the assumptions made in using the isotherm data. Ban (2009) has similarly defined a geometric pore size distributions based on the definition that the pore size of a cavity is the size of the maximum sphere that can be located in that cavity and gives details of an algorithm based on placing test particles on a fine grid of size 0.01nm. For 40 zeolite frameworks (of pore radius of approximately 0.5 nm to 1.3 nm), Ban (2009) also computed isotherms using GCMC and fitted adsorption isotherms of Ar using the Dubinin-Astakhov equations to model the pore filling. It was possible to identify the pore volumes and the pore sizes directly from the corresponding Ar adsorption isotherm and the fitted results of zeolite microporosities agree well with those directly calculated from purely geometric considerations.

Bhattacharya and Gubbins (2006) have given an efficient algorithm for calculating the pores size distribution of a molecular system. Rather than using MC integration as was done in the results reported above, they considered the finding of the largest sphere that could be placed at a certain point in the pore as a constrained non-linear optimization problem and solved it using a suitable nonlinear optimization algorithm.

The algorithm is described by the flowchart shown in Figure 2.9(a) – a point P is picked at random, and the pore radius is computed, and added to a cumulative histogram H , where bin $H(i)$ stores the values of $V(r)$ between $V(i \times \Delta r - \Delta r)$ and $V(i \times \Delta r)$, where Δr is the resolution to which the PSD is required. The values of $P(r)$ for each of the bins, $PSD(i)$, are then calculated by taking the finite difference approximation to the derivative,

$$PSD(i) = \frac{H(i-1) - H(i+1)}{2\Delta r}$$

The algorithm proceeds until the average error in the PSD (averaged over several Monte Carlo blocks) fall below a required tolerance, where the error, calculated as the average of the relative errors between the old and new distribution, is given by,

$$err = \left\langle \frac{PSD_{\text{new}}(R) - PSD_{\text{old}}(R)}{PSD_{\text{old}}(R)} \right\rangle.$$

Figure 2.9(b) depicts the problem of finding the maximum sphere which covers a given point P in the pore, but does not intersect any of the surrounding atoms. The variables involved in the nonlinear optimization are more clearly shown in the two dimensional representation given in Figure 2.9(c).

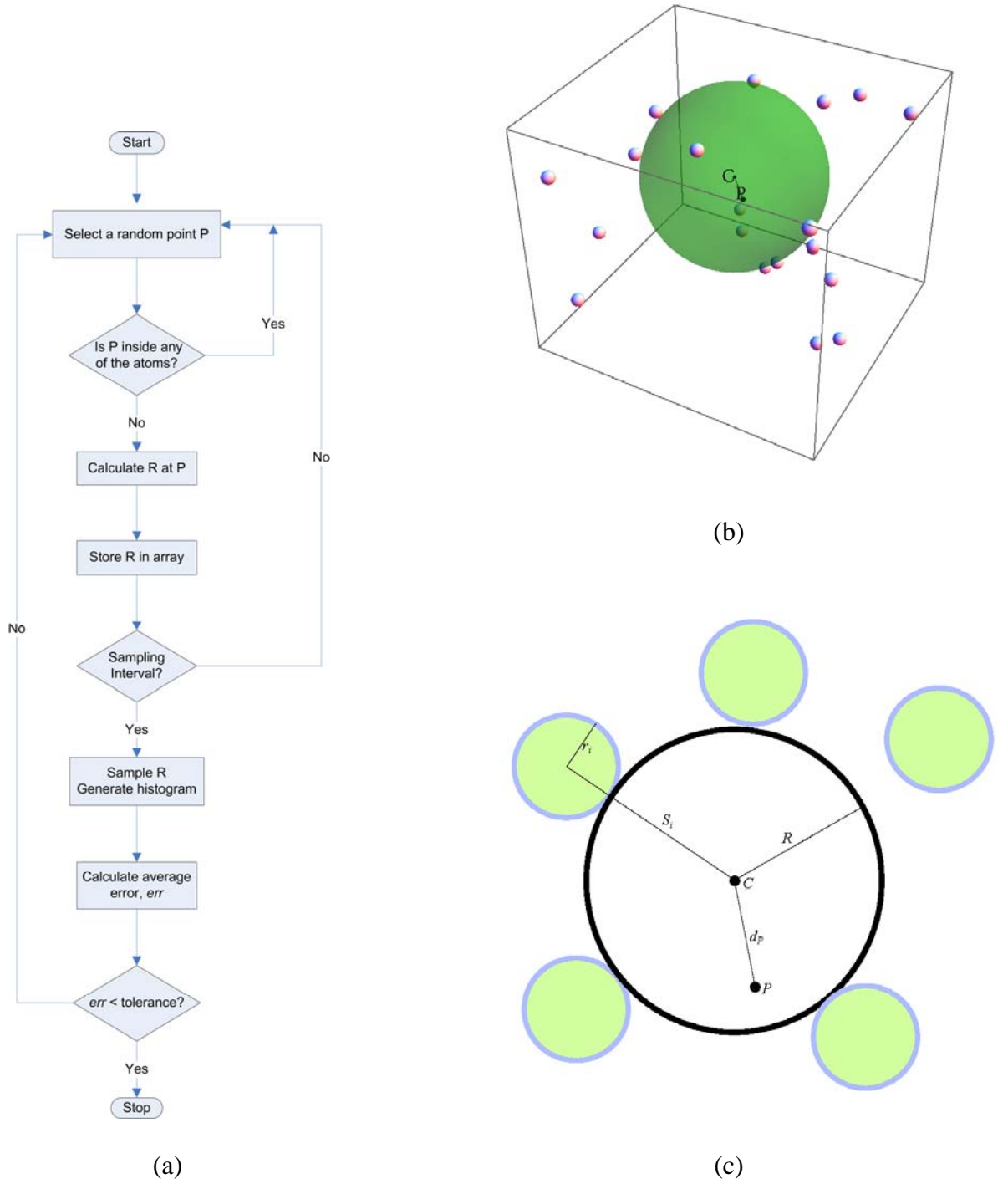


Figure 2.9. (a) Flowchart for the PSD calculation (b) The green sphere is centred at C and is the largest sphere covering point P which does not intersect the atoms. (c) A 2D representation of the system show in b , C is the largest circle, radius R , containing point P but not intersecting any of the disks (atoms) of radius r_i . The distance from C to the centre of atom i is s_i and from C to P is d_p .

If $P(P_x, P_y, P_z)$ is the point where the pore size is to be measured then the centre $C(C_x, C_y, C_z)$ of the sphere whose radius, R , is to be maximized, overlaps P , but does not overlap any of the n spherical atoms of radius r_i which make up the system. The distance between C and P is denoted d_p , and the distance between C and the centre of atom i is denoted s_i .

Now since the radius R , which the sphere at C can have without touching any of the atoms, clearly depends on the position of C ,

$$R(C) = \min(S_i) - r_i, \quad i = 1, \dots, n$$

The required radius R , must therefore be the maximum possible, such that the sphere contains the point P , i.e.

$$d_p \leq R(C)$$

Therefore the nonlinear optimization problem to be solved is,

$$\text{MAXIMISE } R(C) = \min(S_i) - r_i \quad \text{subject to the constraint } d_p - R(C) \leq 0$$

Bhattacharya and Gubbins (2006) used a nonlinear optimization program called SOLVOPT (Kappel and Kuntsevich (2000)) which implements Shor's r -algorithm (Shor, 1985) algorithm. The Shor algorithm is particularly suitable for this problem as it can handle non-smooth objective functions and is thus able to handle the constraints in the above problem. The constraint $d_p \leq R(C)$ is expressed in the form $d_p - R(C) \leq 0$ in the optimization problem above as SOLVOPT implements constraints using penalty functions and requires the

constraints to be given in the form of a function which calculates the maximum residual from a set of constraints at a given point.

Bhattacharya and Gubbins validated this algorithm by using it for a model system with a constructed Gaussian pore size distribution (mean 20Å, standard deviation 3.33 Å). They found good agreement (mean 20.51Å, standard deviation 5.42 Å) and concluded that the bias (0.51 Å) was due to the fact that when generating pore cavities some of the smaller cavities were engulfed by the larger ones. However, the bias of 0.51 Å is almost identical to the bin width of the histogram which can be seen in figure 5 of the original paper (Bhattacharya and Gubbins (2006)), and the original C++ code for the algorithm (<http://supriyo.net/research/psd/psd.htm>) appears to contain an off by one error (possibly as a result of translation from Fortran to C++ where Fortran arrays usually start at 1 where C++ arrays must start at 0), which would account for the discrepancy reported, as the histogram has been effectively shifted by one bin width. Taking this into account, it can be concluded that the algorithm is both highly efficient and accurate.

2.4.5.2 Curve smoothing and differentiation

In cases where curves which contain random errors (noise) must be differentiated to obtain a required function, numerical differentiation can be unstable and risky as it may greatly amplify the noise. Savitzky and Golay (1964) introduced a very popular method for smoothing and (if required) differentiation

to higher orders which involves automatically performing a running least squares polynomial fit on the data.

The method was originally used for correctly visualizing noisy spectroscopic data by preserving both the relative widths and heights of spectral lines. Note that a simple averaging over neighbouring points (while preserving the area under a distribution) has the undesirable effect of lowering the peak height and widening the width of the distribution (Press et al (2003)). Thus this method is particularly useful for distributions such as the cumulative pore size distribution curve described in the previous section, as the numerically differentiated form of the PSD can have much amplified noise as in the case where the central difference is used the variance in the differentiated curve (the PSD) $\dot{\sigma}^2$ is related to the variance in the original cumulative distribution, σ^2 , by (Staggs (2005)),

$$\dot{\sigma}^2 = \frac{\sigma^2}{2(\Delta r)^2}$$

and it is required to recover the original PSD (from the underlying noise) while preserving the shape, both peak widths and heights, of the underlying PSD. With a suitable choice of filter coefficients and the width of the filter window (Press et al (2003)) the Savitzky-Golay algorithm can be very successful in this regard.

2.5 Transport in nanopores

Takaba et al (1998) investigated the permeation of He, CO₂ and N₂ through a thin silica membrane using MD. The equilibrium structure had an effective pore diameter of an equivalent capillary of 8Å and a thickness of 14Å. The pore surface

was not circular but had a rugged surface and the pore atoms were fixed. Their Helium permeance was in good agreement with the value estimated from Knudsen flow while CO₂ showed higher permeance than Knudsen flow. The CO₂ molecules tended to be adsorbed parallel to the pore wall (favourable for diffusion) while the N₂ tended to assume an orientation perpendicular to the wall which decreased its diffusion. Although the O-C-O length is longer than the N-N length, inside the pore the apparent size of N₂ was larger than that of CO₂ and for a mixed CO₂/N₂ gas selective CO₂ permeation was observed. The relative permeability $\alpha_{N_2/CO_2} = 0.22$ at 500K was in good agreement with experimental values reported by Li and Huang (1992).

2.6 Results from chemical vapour deposition (CVD)

Tsapatsis and Gavalas (1994) prepared Hydrogen-permselective membranes by CVD (at atmospheric pressure and temperatures between 873K and 1023K) of SiO₂ layers in porous Vycor tubes using SiCl₄ and H₂O. The deposit was found to be mechanically stable (to stresses caused by thermal cycling) when confined inside the Vycor pores but to be susceptible to crack formation when significantly outside the supporting matrix.

These deposits were annealed at 823 K under dry nitrogen for up to 21 days leading to a reduction in the hydrogen permeance by a factor of about 1.5 to 2.0. The reduced permeance was considered to be caused by a densification of the system due to the removal of silanol groups and the creation of additional Si-O-Si bonds. Water vapour strongly catalyses the rearrangement of these siloxane bonds

and the accelerated densification was confirmed by the ten fold decline of the permeance in the separation layer following thermal treatment in the presence of 3 atm of water vapour (hydrothermal treatment).

Their deposit had a region of approximately 500 nm thickness adjacent to the support tube which had a maximum density and accounted for the permselectivity. This region had a voidage of approximately 10%. The authors provided a qualitative percolation analysis by considering the separation layer to be composed of two phases:

1. Dense SiO₂ with low diffusivity
2. Porous inclusions with much higher diffusivity

The permeability was estimated by considering the composite system to be a random 3D bond conductivity network (with bonds of low conductivity, σ_1 , and high conductivity σ_2 , corresponding to the phases of low and high diffusivity) at the percolation threshold where the total conductivity is given by a power law (Strayley (1977))

$$\langle \sigma \rangle \sim \sigma_1^{1-u} \sigma_2^u$$

or

$$\frac{\langle \sigma \rangle}{\langle \sigma \rangle_2} = \left(\frac{\sigma_1}{\sigma_2} \right)^{1-u}$$

where $\langle \sigma \rangle_2$ is the total conductance when all bonds have conductivity σ_2 . This analysis suggested that trapped porosity near the percolation threshold significantly increases the permeability.

Chapter 3. Simulation of Adsorption and Diffusion in a Model Silica Pore Structure

As outlined in Chapter 2, the quest for a general tractable mathematical model for adsorbing gas transport within porous media has resulted in numerous proposals over the last century or more. The implementation of modern computational techniques in Monte Carlo and molecular dynamics simulation over the last three decades has provided a direct window onto the efficacy and accuracy of many of the models which have been suggested. One of the most recent, and quite sophisticated approaches is the non-equilibrium statistical mechanical method developed by Pozhar and Gubbins (PG) (1993, 1997). In this chapter the simulation methodology employed to test this theory and the results obtained from these computations are detailed for adsorption and diffusion of methane in a model silica nanopore in the vicinity of the capillary fluid critical point.

3.1 The Model Pore Structure

The crystalline nanopore employed as the confining medium was generated by 'etching' an hexagonal capillary within the β -cristobalite (SiO_2) crystal structure parallel to the (111) oxygen crystal plane. The resulting structure (a unit axial cell of which is shown in Figure 3.1(a)), with cross-section dimensions characterized by the distances 3.968 nm, 3.968 nm and 4.582 nm between apex oxygen atoms on opposite sides of the pore, is qualitatively similar to the structure of MCM-41 which is composed of straight non-interconnected, pores of nearly uniform pore size in the range 1.5 – 10 nm (Gelb and Gubbins (1999), Gelb et al (1999)).

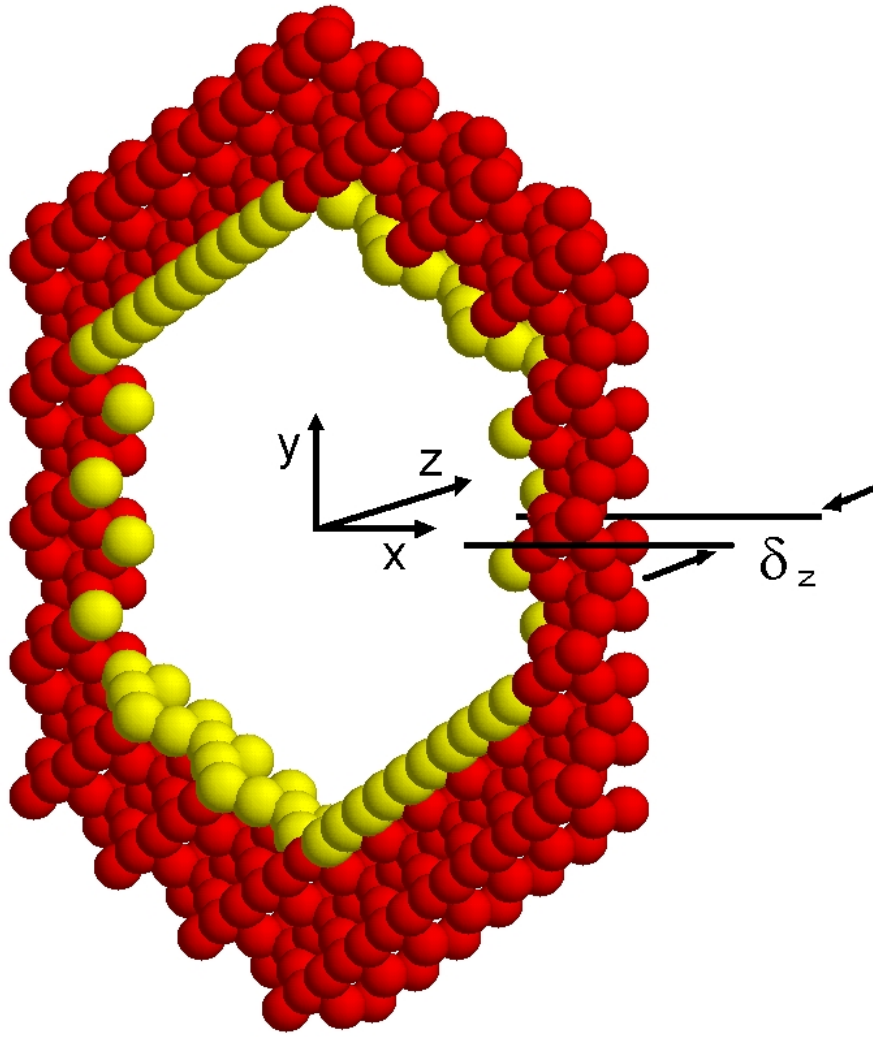


Figure 3.1(a) Single lattice unit of the crystalline structure of the pore wall

The etching process entails the removal of all silicon and oxygen atoms within the x-y boundaries indicated in Figure 3.1(a) and during this process the oxygen atoms within the remaining solid structure are either doubly bonded (siloxane linkages) or singly bonded to the substrate silicon atoms. The doubly bonded oxygens are depicted as red in the figure and the singly bonded oxygens are shown as yellow. In the simulations the latter are treated as united atom hydroxyl groups.

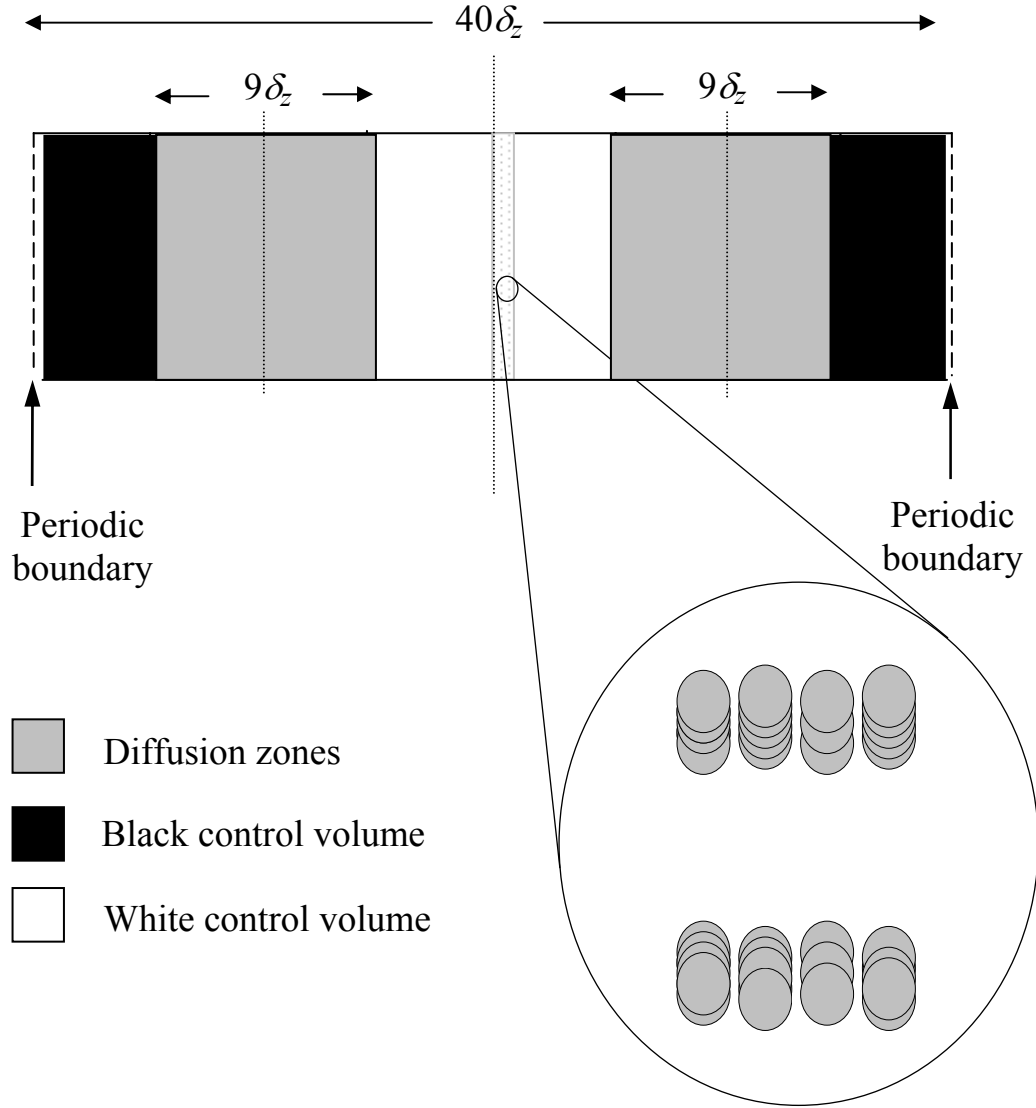


Figure 3.1(b) The fundamental unit cell (total length $40\delta_z$ where $\delta_z = (2\sqrt{2})\lambda_{\text{SiO}}$ and $\lambda_{\text{SiO}} = 1.62\text{\AA}$ is the equilibrium silicon-oxygen bond length in silica).

The axial length of the fundamental cell of the pore is $40\delta_z$ (see Figure 3.1(b)) where δ_z is the repeating unit of the crystalline structure in the z direction (Figure 3.1(a)). $\delta_z = (2\sqrt{2})\lambda_{\text{SiO}}$ and $\lambda_{\text{SiO}} = 1.62\text{\AA}$ is the equilibrium silicon-oxygen bond length in silica)

The model fluid investigated was that introduced by Sung and Dahler (1984) which is a combination of the soft potential of the Weeks-Chandler-Andersen (WCA) theory (1971) with a Hard Core (HC). The soft potential of the WCA theory is the attractive contribution of the Lennard-Jones 12-6 potential. The shifted force form of this potential with parameters chosen to represent a united atom (spherical) representation of methane has been employed in this work. The interactions within the fluid (hereafter referred to as WCA/HC methane) and between the fluid and the individual oxygen and united atom hydroxyl sites are given by

$$\begin{aligned}
\phi_{ij}^{SF}(r_{ij}) &= \phi_{ij}(r_{ij}) - \phi_{ij}(r_{cut}) - \left(\frac{d\phi_{ij}(r_{ij})}{dr_{ij}} \right)_{r_{cut}} (r_{ij} - r_{cut}) \quad \text{for } r_{ij} \leq r_{cut} \\
&= -\varepsilon_{ij} \quad r_{ij} \leq 1.002(2^{1/6} \sigma_{ij}) \\
&= \infty \quad r_{ij} < \sigma_{ij} \\
&= 0 \quad r_{ij} > r_{cut}
\end{aligned} \tag{3.1}$$

where $\phi_{ij}(r_{ij})$ is the Lennard-Jones (12-6) potential

$$\phi_{ij}(r_{ij}) = 4\varepsilon_{ij} \left[\left(\frac{\sigma_{ij}}{r_{ij}} \right)^{12} - \left(\frac{\sigma_{ij}}{r_{ij}} \right)^6 \right]$$

For reasons given by MacElroy and Raghavan (1990) explicit interactions between the fluid particles and the silicon atoms of the solid were omitted in the simulations and the potential parameters for the fluid-fluid and fluid/solid site (oxygen or united atom hydroxyl group) interactions employed in the computations were: $\sigma_{ff} = 0.3817$ nm, $\varepsilon_{ff}/k = 148.2$ K, $\varepsilon_{OO}/k = \varepsilon_{OH,OH}/k = 228.4$ K and the siloxane oxygen and united atom hydroxyl group diameters were taken to be

$\sigma_{OO} = 0.27 \text{ nm}$ and $\sigma_{OH,OH} = 0.3 \text{ nm}$. The Lorentz-Berthelot rules were used to estimate the cross interaction parameters and the cut-off distance r_{cut} was $2.4\sigma_{ij}$.

3.2 Simulation Methods

Grand canonical Monte Carlo (GCMC) simulations were conducted for a broad range of conditions to obtain the low temperature coexistence points for the open pore fluid and to locate the capillary critical temperature for the system. To ensure adequate sampling of the high density states of the system the configurational bias method proposed originally by Mezei (1980) was employed and Markov chains containing at least 10^8 MC events in length were generated for each selected state point.

In addition to providing the coexistence diagrams, the equilibrium configurational states obtained from these simulations are used as input data for the molecular dynamics (MD) simulations. The WCA/HC fluid particle trajectories were computed using the Verlet-Sturmer finite difference method (Verlet (1967)) supplemented with an *a posteriori* collision procedure (see McNeil and Madden (1982)) to determine the hard core collision sequence for each fluid particle in the system. In all cases the time step employed was 1.25 fs and the dynamical properties of the pore fluid were evaluated at selected state points for trajectories up to 20 ns in length. In a number of cases pure hard sphere simulations were also conducted for comparative purposes at the same total loadings employed in the WCA/HC fluid MD computations.

3.3 The Diffusion Model

The properties evaluated during the simulations included the local densities in each of the x , y and z directions and the local collision frequencies of the fluid particles within the fluid and with the sites in the pore walls. These quantities were determined on 120000 grid points distributed within the pore space of each of the 40 individual lattice units making up the fundamental cell (see Figure 3.1 and Figure 3.2).

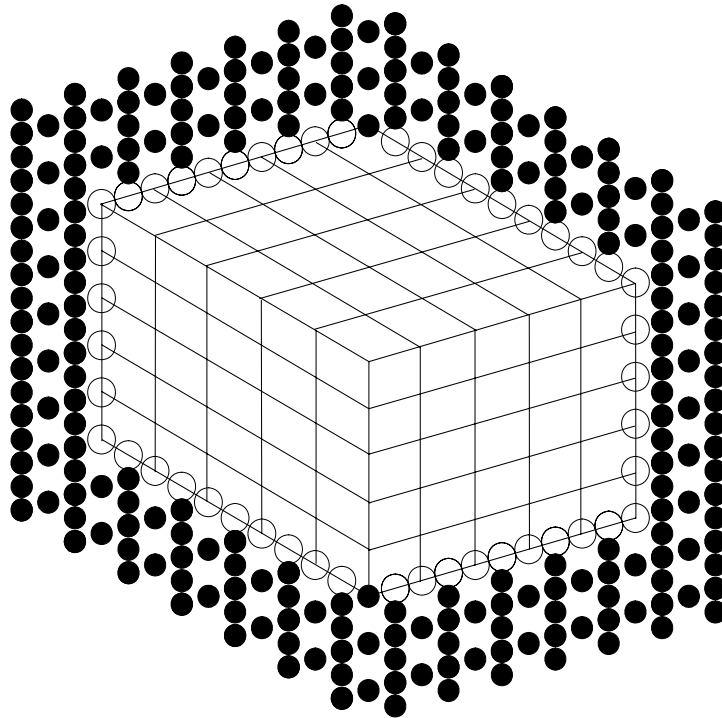


Figure 3.2 The grid structure employed in x - y directions for sampling collisions. The individual lattice units shown in Figure 3.1(a) contain 75 sub-units each of which is further subdivided into 100 elements and the axial z -direction is divided into 16 elements.

The axial self-diffusion coefficients were also computed using the Einstein equation

$$\tilde{D}_{1^*,E}^z = \lim_{t \rightarrow \infty} \frac{1}{2} \frac{d \langle (z_{1^*}(t) - z_{1^*}(0))^2 \rangle}{dt} \quad (3.2)$$

where the tilde indicates a volume average over inhomogeneous length scales within the pore. The 1* subscript refers to the trace component which, in this case, has the same properties as the solvent, component 1 (overall fluid properties are designated with a subscript *f*). In recent work (MacElroy et al (2001)) questions have been raised concerning the interpretation of the self-diffusivity defined in Equation (3.2). In particular, in view of the strongly inhomogeneous structure of fluids confined within very narrow pores, the following question is posed: can one reasonably assume that the quasi-homogeneous definition provided in Equation (3.2) is in one-to-one correspondence with the diffusivity appearing in the expression

$$\bar{J}_{1^*}^z = -\tilde{D}_{1^*,F}^z \frac{d\tilde{n}_{1^*}}{dz} \quad (3.3)$$

Equation (3.3) is simply the pore averaged (coarse-grained) Fickian flux of a trace component diffusing in the axial direction within the pore and it is this mathematical form which is widely employed in scientific and engineering modeling of transport in porous media. In Equation (3.3) the overbar on the flux represents averaging over the pore cross-section and at steady-state this flux is independent of *z*.

To test the validity of the equivalence of the diffusivities in Equations (3.2) and (3.3) for the pore employed in this work non-equilibrium MD colour diffusion simulations were also conducted during the computations. The procedure employed

is illustrated schematically in Figure 3.1(b). The pore, in which the fluid as a whole is at equilibrium, is separated into four zones: a central control volume of length $11\delta_z$ in which the fluid particles are tagged as ‘white’ and a control volume (also of total length $11\delta_z$) on the periphery to the left and right connected through the periodic boundary in which the fluid particles are tagged as ‘black’. The two ‘grey’ zones are regions in which the black and white particles counterdiffuse. The computations, which were conducted during the course of the EMD simulations, were initiated in two independent ways:

(a) The fluid particles within the diffusion zones were initially segregated in equal parts to the left and right of the dashed lines shown in Figure 3.1(b) and tagged with the colour appropriate to the adjacent control volume. The concentration gradient was then allowed to relax and the particle fluxes were monitored as the system approached steady state. During the simulations any white particles which entered the black particle control volume were automatically switched in colour; a similar process occurred if a black particle entered the white particle control volume.

(b) The procedure described in (a) was employed in the initial phase of the simulations reported in this work and would normally correspond to the approach one might employ to investigate interdiffusion of dissimilar species. However, as the tagged particles are identical in the present studies, the equilibrium colour mole fraction profiles obtained from the simulations become linear at steady state, and in view of the computational time required for the equilibrium profile to develop, the following initial condition was also used. A linear profile in the mole fraction of each colour component was imposed initially within the diffusion zones. The system was then tracked in time using the same procedure as in (a) above to verify

that the linear profile of the two species was maintained during the course of the simulation.

The rate of colour flow, R_c (particles/ps), was simply determined in both cases as the number of black or white colour particles crossing the centrelines in both of the diffusion zones shown in Figure 3.1(b) per unit time. The Fickian diffusivity was then estimated using Equation (3.3) in the form

$$\tilde{D}_{1^*,F}^z = R_c \frac{L_{DZ} L_{CV}}{\langle N \rangle_{CV}} \quad (3.4)$$

where $L_{DZ} = 9\delta_z$ is the length of the individual diffusion zones, $L_{CV} = 11\delta_z$ is the length of the control volumes and $\langle N \rangle_{CV}$ is the ensemble average number of fluid particles within the respective control volumes (see Heffelfinger and van Swol (1994) and MacElroy (1994)).

In addition to the MD simulation results for self-diffusion, the corresponding diffusivities predicted by PG theory (Pozhar and Gubbins (1993, 1997)) are also reported. The model fluid and the nature of the fluid/wall interactions employed in the current work conform to the decomposition of the particle-particle interaction potential explicitly employed by Pozhar and Gubbins and the expression for the self-diffusion coefficient given by this theory is (see MacElroy et al (2001) for details)

$$\frac{1}{D_{1^*}(\mathbf{r})} = \frac{2}{3} \sqrt{\frac{m\beta}{\pi}} \left[\sigma_{ff}^2 \int d\mathbf{k} n_f(\mathbf{r} - \sigma_{ff}\mathbf{k}) g_{ff}(\mathbf{r}, \mathbf{r} - \sigma_{ff}\mathbf{k}) + \sqrt{2} \sigma_{fw}^2 \int d\mathbf{k} n_w(\mathbf{r} - \sigma_{fw}\mathbf{k}) g_{fw}(\mathbf{r}, \mathbf{r} - \sigma_{fw}\mathbf{k}) \right] \quad (3.5)$$

or

$$\frac{1}{D_{1*}(\mathbf{r})} = \frac{2m\beta}{3} \left[\omega_{1*}^{ff}(\mathbf{r}) + 2\omega_{1*}^{fw}(\mathbf{r}) \right] \quad (3.6)$$

where $\beta = 1/kT$, m = particle mass, σ is the hard core codiameter appearing in Equation (3.1) (subscript f referring to the fluid particles and w referring to the wall atoms), n is the dimensional number density, \mathbf{r} is the coordinate within the fluid, g_{ij} is the hard sphere contact pair correlation function for the pair ij , \mathbf{k} is the unit vector along the line of centers of the colliding pair (fluid-fluid or fluid-wall atom), $d\mathbf{k}$ is the solid angle, and in Equation (3.6) $\omega_{1*}^{ij}(\mathbf{r})$ is the local collision frequency of the trace species for fluid-fluid collisions ($i, j = f$) or fluid-wall collisions ($i = f, j = w$).

The second of these expressions, which gives the local self-diffusivity in terms of the local fluid-fluid and fluid-wall hard core collision frequencies, was readily evaluated during the EMD simulations and avoids the much more difficult computation of the local contact pair distribution functions required in the solid angle integrals of Equation (3.5).

3.4 Results and Discussion

3.4.1 Equilibrium Adsorption

The equilibrium isotherms computed at three temperatures for the model system described above are illustrated in Figure 3.3. Two of the temperatures are subcritical and in both cases the hysteresis loops are very narrow or non-existent (in the vicinity of $\mu^{\text{ex}}/kT = -11$ at 90K and $\mu^{\text{ex}}/kT = -9$ at 110K).

At low loadings the individual isotherms exhibit comparatively sharp knees at $\langle n_f^* \rangle \sim 0.1$ with less distinct jumps occurring at $\langle n_f^* \rangle \sim 0.2$ and 0.3 . In the case of the two lower loading steps these correspond to supercritical monolayer wetting transitions taking place on distinct faces of the pore wall. This is clearly illustrated in Figure 3.4 where the cross-sectional views of the pore at three loadings are explicitly shown. The sparse distribution of fluid particles at low densities is shown in perspective view in Figure 3.5.

The capillary condensation processes shown at 90K and 110K occur when essentially the first two layers have filled and, in agreement with observations reported recently (see for example Libby and Monson (2003)) this pore filling takes place in the absence of the pre-condensation necking suggested by the earlier classical theory of capillary condensation (Everett (1967)).

3.4.2 Diffusion Studies

3.4.2.1 Einstein Diffusion

The volume-averaged self-diffusion coefficients determined using the Einstein relationship and colour diffusion (see Section 3.3) are reported in Figure 3.6 at the supercritical temperature of 130K (Figure 3.6(a)) and at the sub-critical temperature of 110K (Figure 3.6(b)). In both cases there is excellent agreement between the two methods validating the use of linear response theory in this inhomogeneous pore structure.

The very sharp variations in the overall fluid axial density profiles reported in Figure 3.7 for a sample density profile at $T = 130\text{K}$ and $\langle n_f^* \rangle = 0.3875$ demonstrate

the extent to which this pore is inhomogeneous in the z -direction. Each ‘large spike - small spike’ pattern occurs in one repeat unit (width δ_z) of the wall lattice.

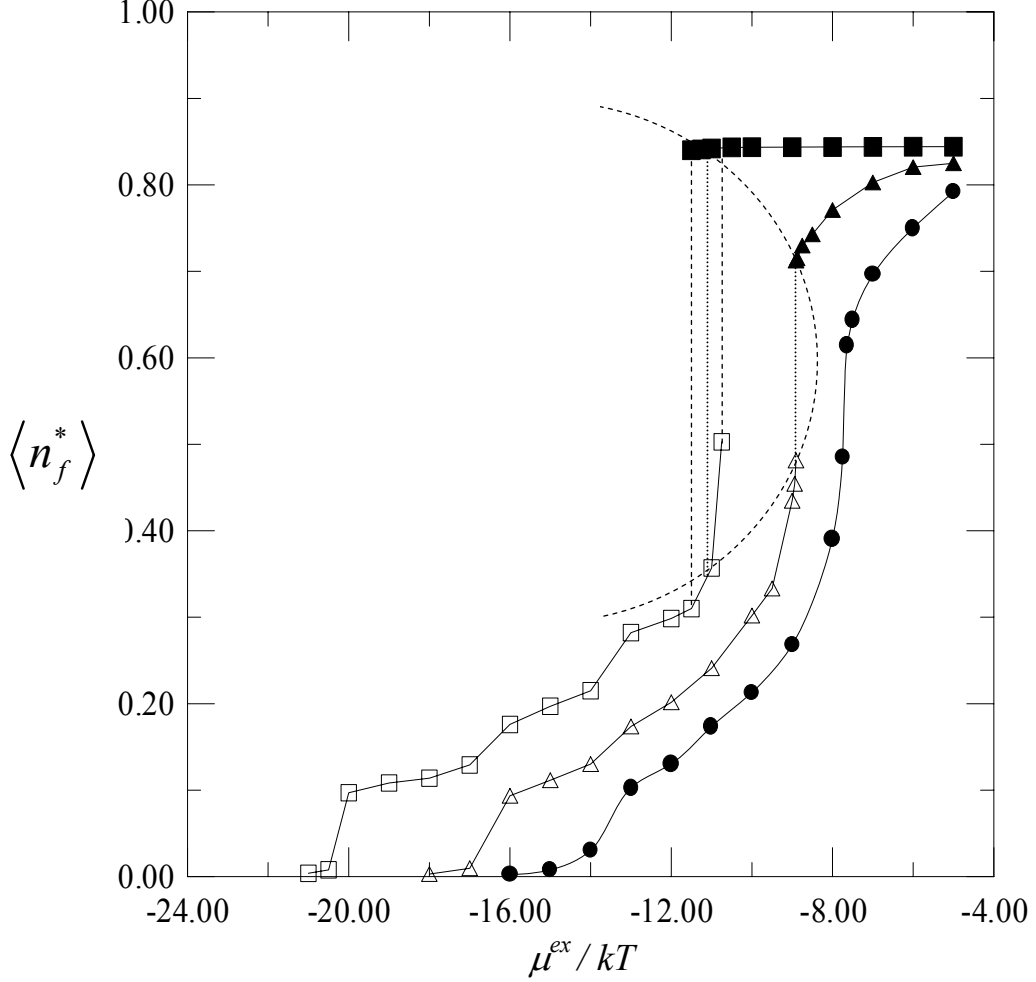


Figure 3.3. Equilibrium adsorption isotherms. $\langle n_f^* \rangle$ is the reduced average fluid number density $\langle n_f \delta_{ff}^3 \rangle$ within the pore and the three isotherms are: \square 90K; Δ 110K; \bullet 130K. The dotted lines correspond to the coexistence tie-lines and the dashed curve is a guide-to-the-eye indicating the position of the two-phase region.

3.4.2.2 Colour Diffusion

The method employed to determine the colour diffusion coefficients requires some discussion. In initial computations (method (a) as described above in Section

3.3) the flux and profile measurements were obtained by starting directly from a step profile located at the mid-point within the diffusion zones shown in Figure 3.1(b).

The computer time required to reach steady state concentration profiles in these simulations was, however, very large. In Figure 3.8 the colour profiles resulting from an initial step profile are shown for the time range 4-8 ns in a 20 ns run at conditions corresponding to $\langle n_f^* \rangle = 0.3875$ at $T = 130\text{K}$. It is clear that even though \tilde{D}_{1*} is at its maximum value under these conditions the colour profiles at intermediate times for an initial step profile are only partially developed. Interestingly the fluxes for this 20 ns run settled to steady state fairly quickly as shown in Figure 3.9 for the time range 0 – 2 ns.

Also shown in Figure 3.8 are the profiles obtained during the same time period (4-8 ns) with an imposed initial condition corresponding to the linear colour mole fraction profiles of the known steady state. These profiles clearly retain their linear structure whereas the ‘kinks’ in the concentration profiles for initial step conditions are a result of the very slow interchange of coloured particles adsorbed in deep sites at the pore walls with fluid particles nearer the center of the pore. Results not shown here for the time range 16-20 ns for both methods ultimately resulted in coincident linear profiles. The flux for the system with initial linear profiles is also shown in Figure 3.9 and as expected the results coincide with the flux based on an initial step profile except at short times.

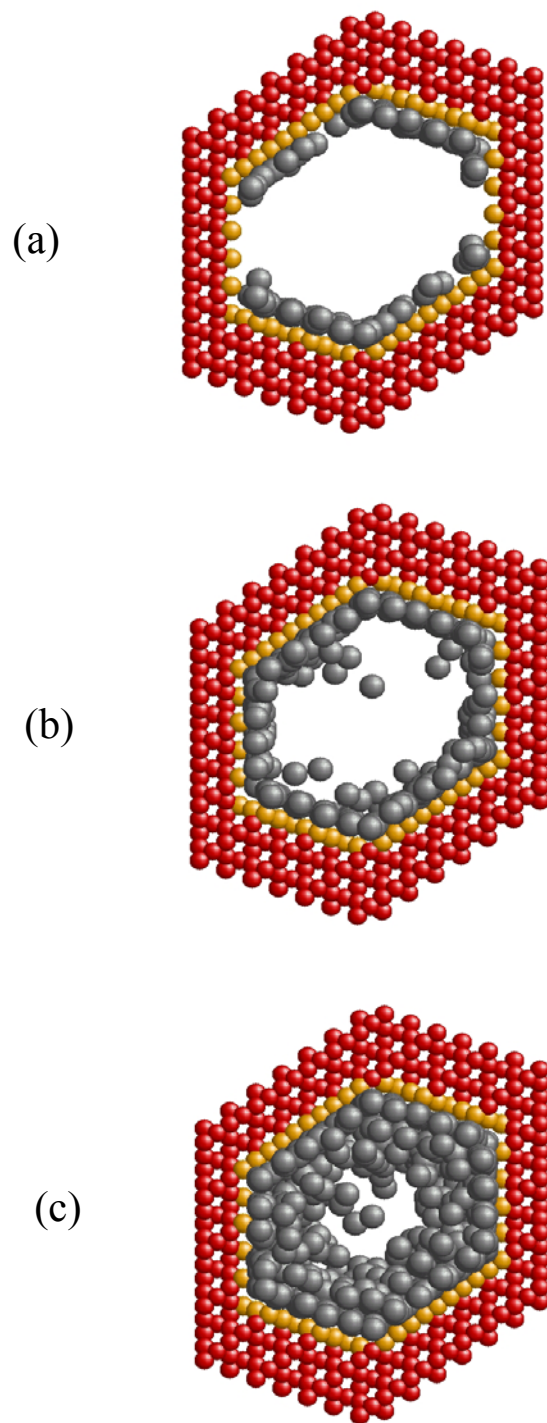


Figure 3.4. Snapshots of the formation of the adsorbed layer within the crystalline silica pore under capillary supercritical conditions ($T = 130\text{K}$). These results correspond to the three points at $\mu^{\text{ex}}/kT = -13$ (a), -10 (b) and -8 (c) in Figure 3.3.

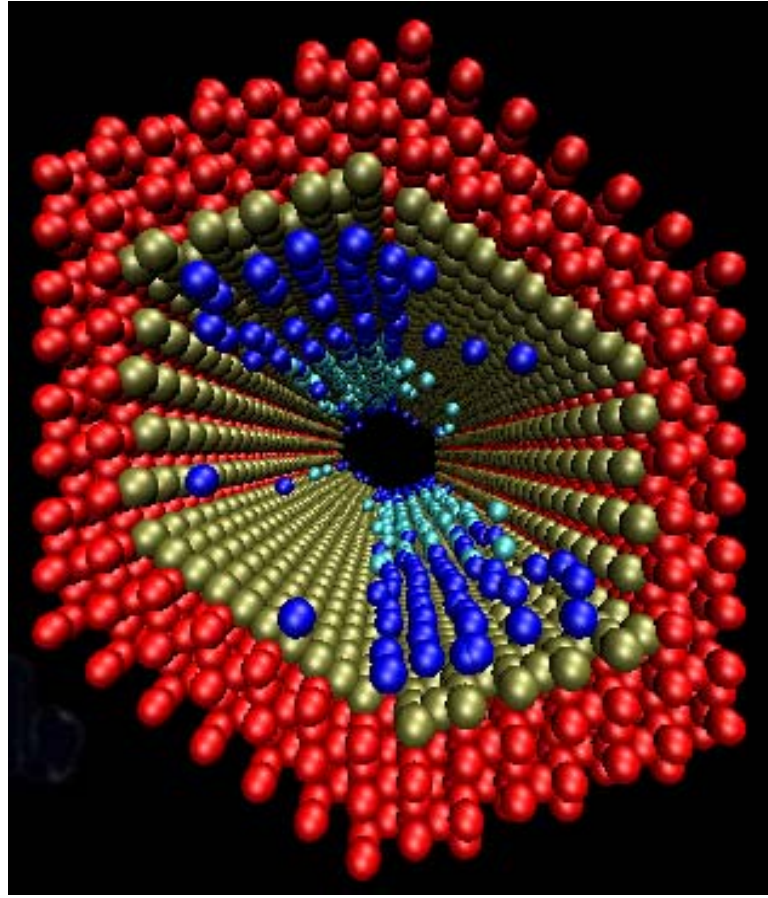


Figure 3.5. View along the pore axis for $\mu^{\text{ex}}/kT = -14$ at 130K.

3.4.2.3 Pozhar-Gubbins Theory

Also shown in Figure 3.6 are the results for the pore averaged self-diffusion coefficient predicted by PG theory. The manner in which these results were obtained differs slightly from the procedure described earlier by MacElroy et al (2001). The expression for the local cross-sectional averaged flux expression provided by PG theory (within the scope of the pseudo-homogeneous approximation discussed in MacElroy et al (2001)) is given by

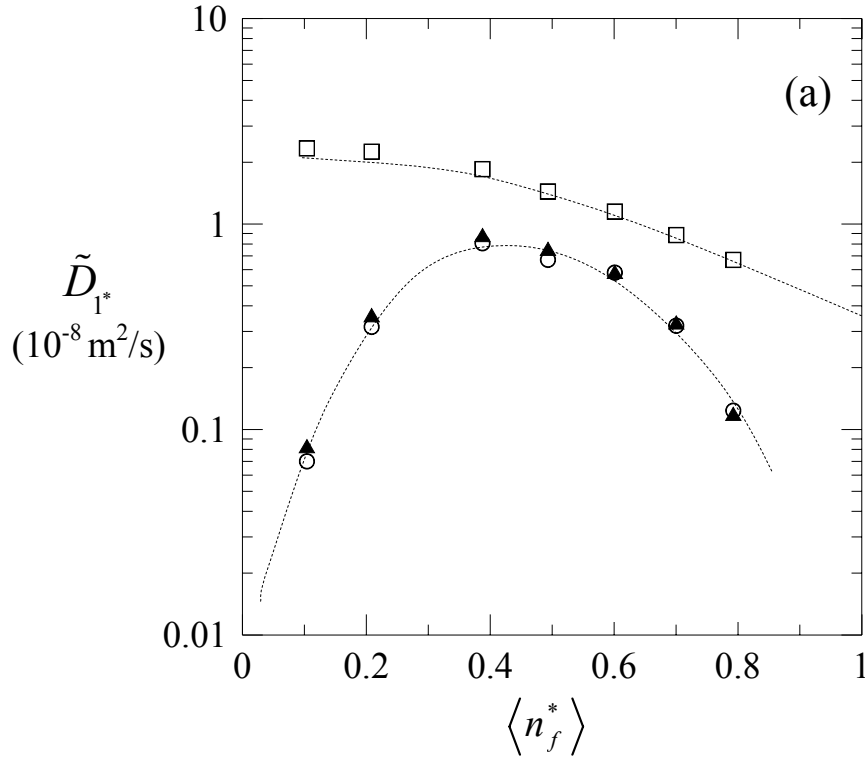


Figure 3.6(a) The self-diffusion averaged over the pore volume as a function of pore loading for $T = 130\text{K}$. \blacktriangle From Einstein's relation, equation (2); \circ colour self-diffusivities, Equation (3.4); \square PG theory, Equation (3.11) (see below).

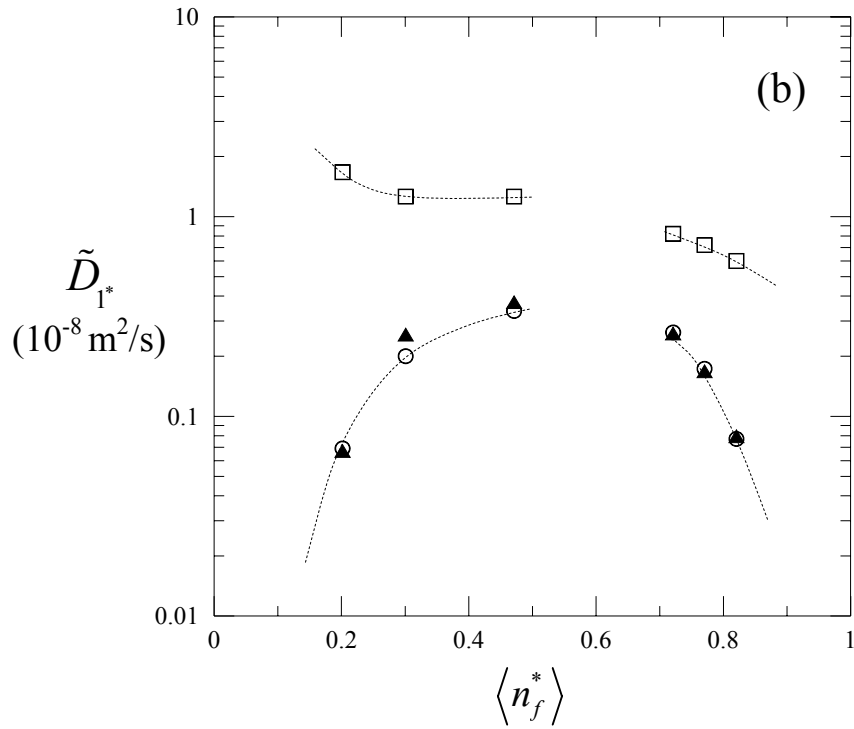


Figure 3.6(b). As in (a) for $T = 110\text{K}$. In both cases the dashed lines are guides to the eye and the gaps shown in (b) are indicative of the coexistence region.

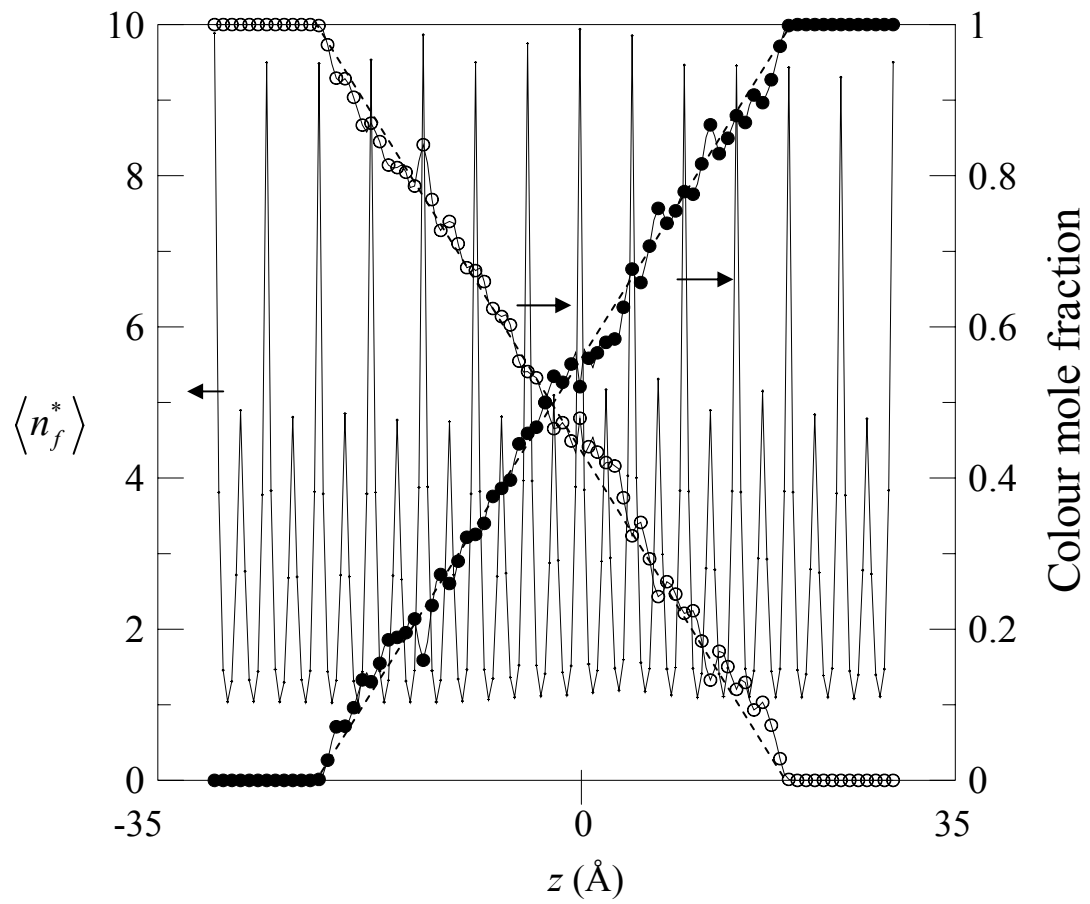


Figure 3.7. The reduced pore fluid density (the continuous sharply spiked line) and the individual colour mole fraction profiles within the diffusion zones shown in Figure 3.1(b). The profiles in both diffusion zones have been averaged and the axial origin of the system has been translated to the profile centerline.

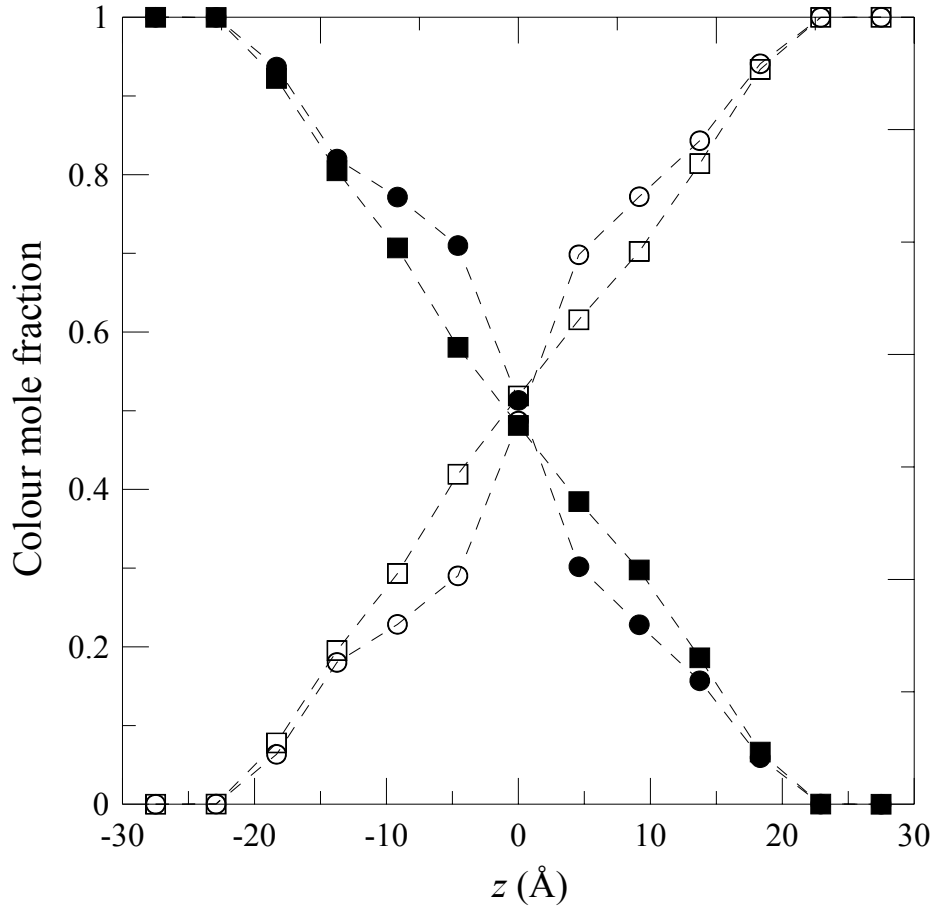


Figure 3.8. Colour mole fraction profiles for $\langle n_f^* \rangle = 0.3875$ and $T = 130\text{K}$ within the diffusion zones shown in Figure 3.1(b). The open (‘white’ profile) and filled (‘black’ profile) circles correspond to the averaged profiles obtained during the period 4-8 ns with an initial step profile at $t = 0$ (all ‘black’ for $z < 0$ and all ‘white’ for $z > 0$). The open (‘white’) and filled (‘black’) squares are for the same time range but with initial linear mole fraction profiles imposed on the system.

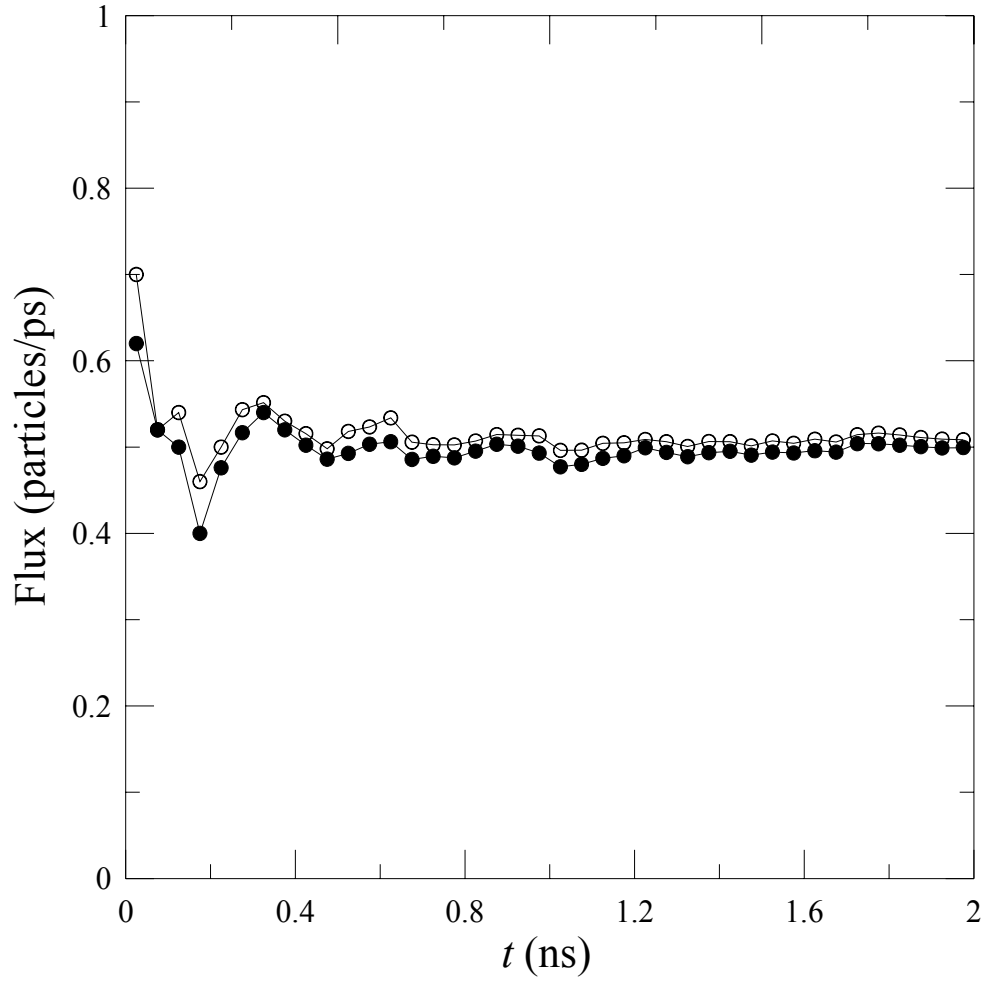


Figure 3.9. The particle flux as a function of time within the diffusion zones for the same conditions as in Figure 3.8 (O initial step profiles; ● initial linear profiles).

$$\begin{aligned}
 \bar{J}_{1*}^z &= \frac{1}{A} \int J_{1*}^z dx dy \\
 &= - \left[\frac{\int D_{1*}(\mathbf{r}) \frac{\partial \delta n_{1*}(\mathbf{r})}{\partial z} dx dy}{\int \frac{\partial \delta n_{1*}(\mathbf{r})}{\partial z} dx dy} \right] \frac{1}{A} \int \frac{\partial \delta n_{1*}(\mathbf{r})}{\partial z} dx dy \\
 &= - \bar{D}_{1*}(z) \frac{\partial \delta \bar{n}_{1*}(z)}{\partial z}
 \end{aligned} \tag{3.7}$$

where $D_{1*}(\mathbf{r})$ is given by Equation (3.5) and $\delta n_{1*}(\mathbf{r})$ is the fluctuation of the local concentration of the tracer from its equilibrium value. Note that the area averaged tracer diffusion coefficient $\bar{D}_{1*}(z)$ is a function of z within the individual lattice units shown in Figure 3.1(b) since the corresponding area averaged fluctuation $\delta \bar{n}_{1*}(z)$ is in general a (unknown) nonlinear function of z . In MacElroy et al (2001) it was assumed that the gradient of the concentration fluctuation was independent of x and y leading to

$$\bar{D}_{1*}(z) = \frac{1}{A} \int D_{1*}(\mathbf{r}) dx dy \quad (3.8)$$

This simplified result however leads to a physical inconsistency in the limit $n(\mathbf{r}) \rightarrow 0$. Equation (3.5) demonstrates that, for those regions within the pore that are distant from the pore wall atoms, the local diffusivity simplifies to

$$\frac{1}{D_{1*}(\mathbf{r})} = \frac{2}{3} \sqrt{\frac{m\beta}{\pi}} \left[\sigma_{ff}^2 \int d\mathbf{k} n_{ff}(\mathbf{r} - \sigma_{ff} \mathbf{k}) g_{ff}(\mathbf{r}, \mathbf{r} - \sigma_{ff} \mathbf{k}) \right] \quad (3.9)$$

At low pore loadings the fluid density in the vicinity of the pore centerline will be very small and in this region the local diffusivity will be commensurately large. In this case Equation (3.8) would imply that the average diffusivity would be very large. This is counterintuitive, however, in view of the backscattering one would anticipate arising from the atomically ‘rough’ surface of the pore walls, i.e. one would at least expect to observe Knudsen-like diffusion in this limit modified to some extent by the attractive (adsorptive) interactions of the pore wall (which appear indirectly through the pair correlation functions). A consistent result for the

cross-sectional averaged diffusivity may be obtained by noting that in the trace limit $n_{1*} \rightarrow 0$ (i.e. the mole fraction $x_{1*} \rightarrow 0$) then

$$d\delta n_{1*}(\mathbf{r}) = n_f(\mathbf{r})d\delta x_{1*}(\mathbf{r}) \quad (3.10)$$

Now, while the local number density of the fluid and the tracer will generally be a strong function of position within the pore, it is physically reasonable to assume that the mole fraction of the species (and fluctuations of these quantities) will vary much more slowly in space (see Figure 3.7 for example). Substituting Equation (3.10) into Equation (3.7) gives

$$\bar{D}_{1*}(z) = \left[\frac{\int D_{1*}(\mathbf{r})n_f(\mathbf{r})\frac{\partial \delta x_{1*}(\mathbf{r})}{\partial z}dxdy}{\int n_f(\mathbf{r})\frac{\partial \delta x_{1*}(\mathbf{r})}{\partial z}dxdy} \right] = \frac{\int D_{1*}(\mathbf{r})n_f(\mathbf{r})dxdy}{\int n_f(\mathbf{r})dxdy} \quad (3.11)$$

The last expression on the right is obtained by assuming the mole fraction fluctuation is essentially independent of x and y which is a more reliable premise than assuming $\delta n_{1*}(\mathbf{r})$ is independent of x and y as employed in Equation (3.8). Equation (3.11) also leads to a physically realistic estimate of the hard sphere diffusivity at low loadings (the Knudsen limit) for this pore structure as will be shown below. It should also be noted that at high densities the simulation results suggest that there are only minor differences between the estimates provided by both Equations (3.7) and (3.11) which explains the good agreement reported in MacElroy et al (2001) between simulation and PG theory.

From Figure 3.6 it is observed that PG theory is in fair agreement (within 50%) with molecular simulation in the vicinity of the capillary critical density although

there is significant overestimation of the self-diffusivity at both high and low densities. The observations at high density are consistent with comparable effects in Enskog or modified-Enskog hard sphere fluids which arise due to cageing and backscattering at such densities. The disagreement at low densities however was unexpected. At this time some uncertainty exists with regard to the influence of the approximations made in the formulation of Equation (3.7) (see MacElroy et al (2001) for details).

However one insight is provided in Figures 3.10 and 3.11. In Figure 3.10 snapshots of the WCA/HC methane particles adsorbed at the lowest loading at $T = 130\text{K}$ are shown at five different times (0.0, 1.0, 2.0, 3.0, and 4.0 ns). The darker particles correspond to those which have not moved more than 20 \AA in the given time period and the lightly shaded spheres are the faster diffusing particles.

While a multi-frame film of this system illustrates the process more clearly the five frames shown in Figure 3.10 demonstrate that many of the particles are effectively trapped in high energy sites for significant periods of time and undergo repeated collisions with the *same* wall atoms during this time. Re-collisional memory effects of this kind with stationary wall particles can lead to a very significant reduction in the diffusivity (as evidenced, for example, in Lorentz gases (Park and MacElroy (1989))) and this is believed to be the primary reason for the large discrepancies between PG theory and simulation. The far greater prevalence of fluid-wall collisions over those between the gas phase fluid particles themselves (for which the Boltzmann molecular chaos Ansatz may be assumed to hold quite well) in the first monolayer next to the pore wall is illustrated in Figure 3.11. This

also serves to emphasise the relative importance of re-collisional events with the static wall particles.

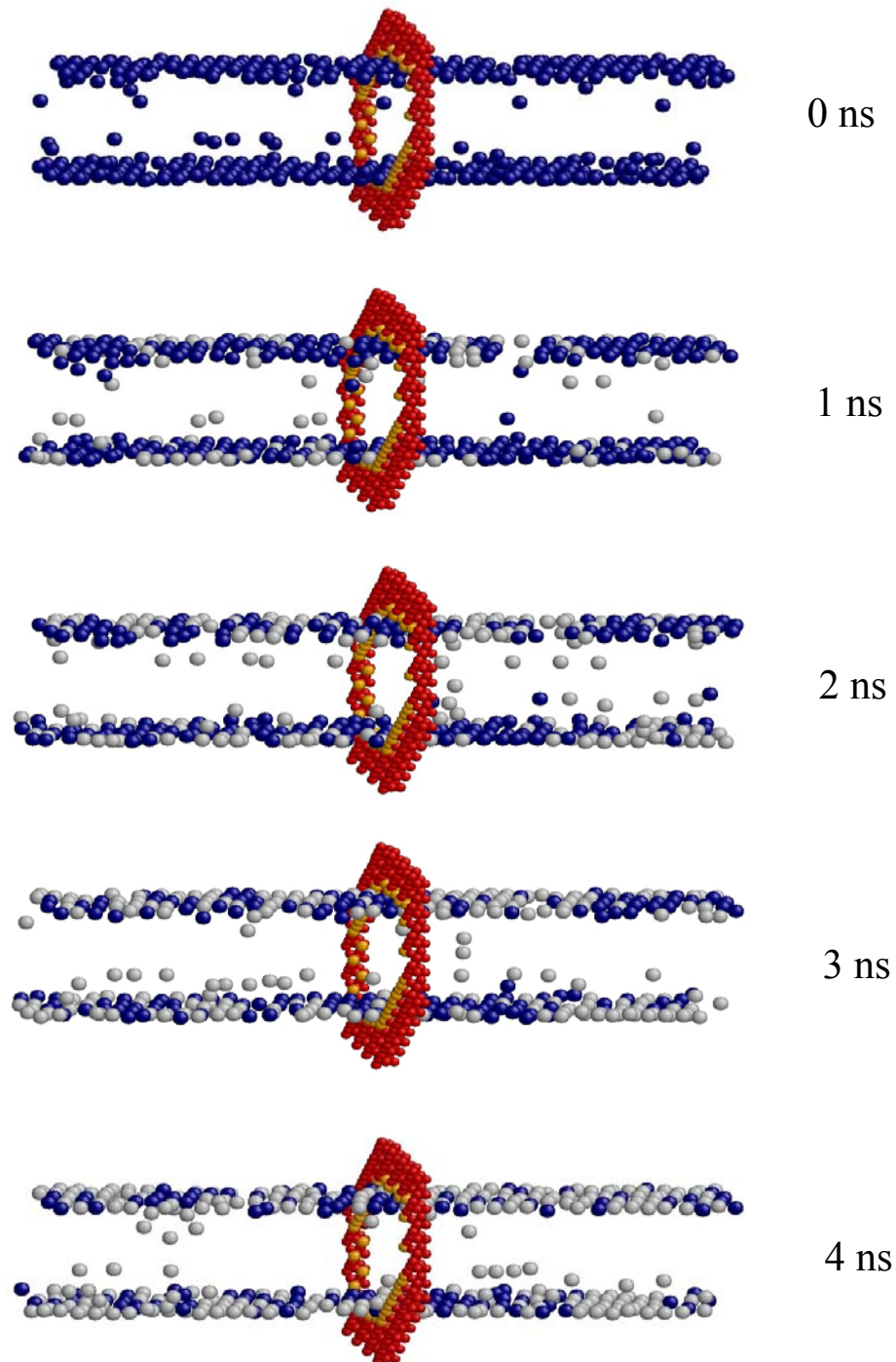


Figure 3.10. Snapshots (taken at times of 0, 1, 2, 3, and 4ns) of the adsorbed particles for the system with the lowest loading at $T = 130\text{K}$. The dark spheres are the particles that have not moved more than 20\AA up until the time corresponding to the frame. Only one solid lattice unit is shown for reference.

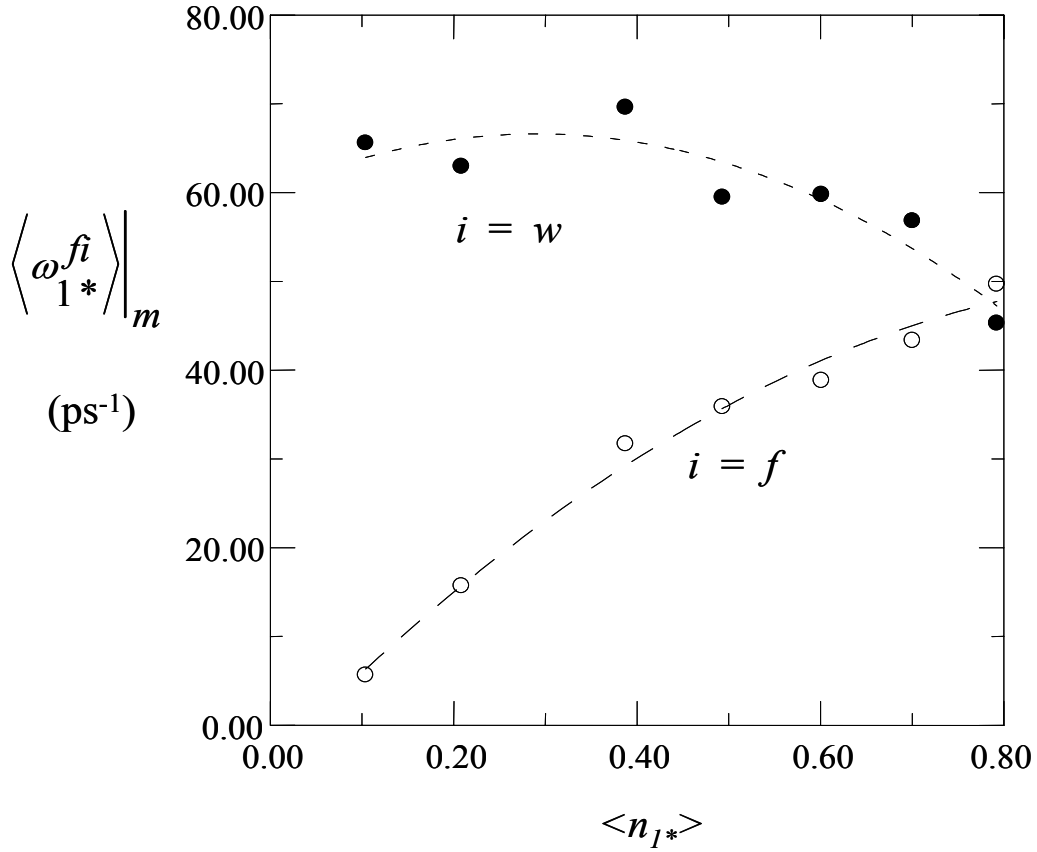


Figure 3.11. Volume-averaged fluid-wall and fluid-fluid collision frequencies within the monolayer nearest the wall as functions of the pore loading under supercritical conditions.

In support of the above suggestion, pure hard sphere simulations were also conducted and the results at the same set of densities as in the supercritical isotherm are shown in Figure 3.12. In this case surface trapping due to adsorption is not present and there is now much better agreement between theory and simulation.

3.5 Summary

While questions have been raised recently concerning the applicability of the pseudo-homogeneous expressions provided by linear response theory for the

diffusion fluxes within strongly inhomogeneous systems, the results reported in this work support the validity of this approach. Furthermore, in view of the long-range correlations synonymous with the capillary critical region the results obtained in this work are believed to serve as a stringent test of this assumption.

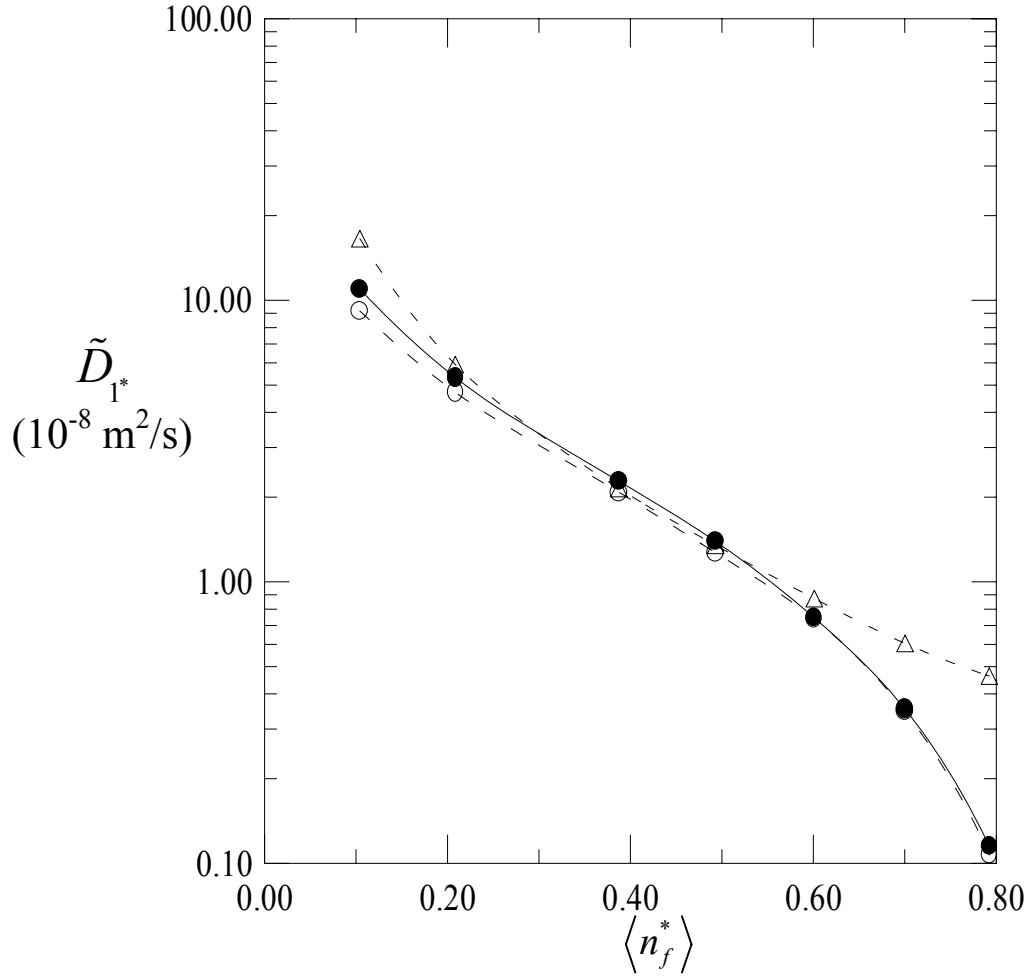


Figure 3.12. The self-diffusion coefficient averaged over the pore volume for the hard sphere system under the same conditions as in Figure 3.7(a). ● From Einstein's equation; ○ colour self-diffusivities; Δ PG theory.

An analysis of the quasi-hydrodynamic theory of Pozhar and Gubbins for self-diffusion suggests that, while the emphasis of this theory on the importance of fluctuation phenomena around the equilibrium state is well founded, there would appear to be significant discrepancies at both high and low loadings. At this time it is suggested that the primary origin for this rests with the assumption that recollisional dynamical events which are present to a great extent at the stated conditions are not accounted for within the theory.

Finally, irrespective of the approach employed, the results of this work demonstrate that self or tracer diffusion within a nanopore fluid at or just above the capillary critical temperature exhibits a maximum. This observation may have technological implications for adsorption/desorption processes in chromatography and supercritical extraction of trace compounds and, in principle, this could be used to advantage in enhancing the transport rates of trace species within microporous materials.

Chapter 4. Exploratory Studies of Diffusion in Dense Silica Films: Background, Methodology and Results

A major field of ongoing study in gas mixture separation technology involves the development of novel composite ceramic membranes suitable for use across a broad range of process conditions. A common theme in these studies is the use of support membranes composed of a mesoporous/microporous substrate materials (e.g. α -alumina/ γ -alumina, Vycor etc) with a minimum pore size of approximately 5 nm, in some cases supplemented with a further metal or silicon oxide microporous layer with pore dimensions of 1-3nm, upon which is deposited a submicron thick permselective layer of silica containing pores in the Angstrom range (see for example Lee et al (2004), Cuffe et al (2006), Araki et al (2007) and McCann (2010)). The latter layer is the selective coating which itself is typically 30-100 nm thick. While it is generally assumed that the transport process of the gas species within this selective layer is activated in nature, there are anomalies with this simplified picture. In order to more fully understand the transport mechanisms within these composite materials and, in particular, how one may develop the optimum conditions for both maximum permselectivity and maximum capacity, exploratory simulation studies are reported in this work in which the time evolution of the trajectories and, most notably, the free particle mean-square displacements are evaluated for the diffusing species within model dense silica media over a range of temperatures.

4.1 Background

Figure 4.1 provides an illustrative example of the kind of composite films of interest here. In this figure the image on the left is a scanning electron micrograph

of a thin film of silica which has been deposited onto a mesoporous/microporous substrate material (McCann (2010)). The thin 100 nm film shown to the right of the SEM image was fabricated via atmospheric pressure plasma liquid deposition (APPLD) and was reported by McCann (2010) to have an ideal permselectivity for the gases Helium and Nitrogen of $\text{He}/\text{N}_2 = 55$ and an estimated nominal pore size of 0.4 nm.

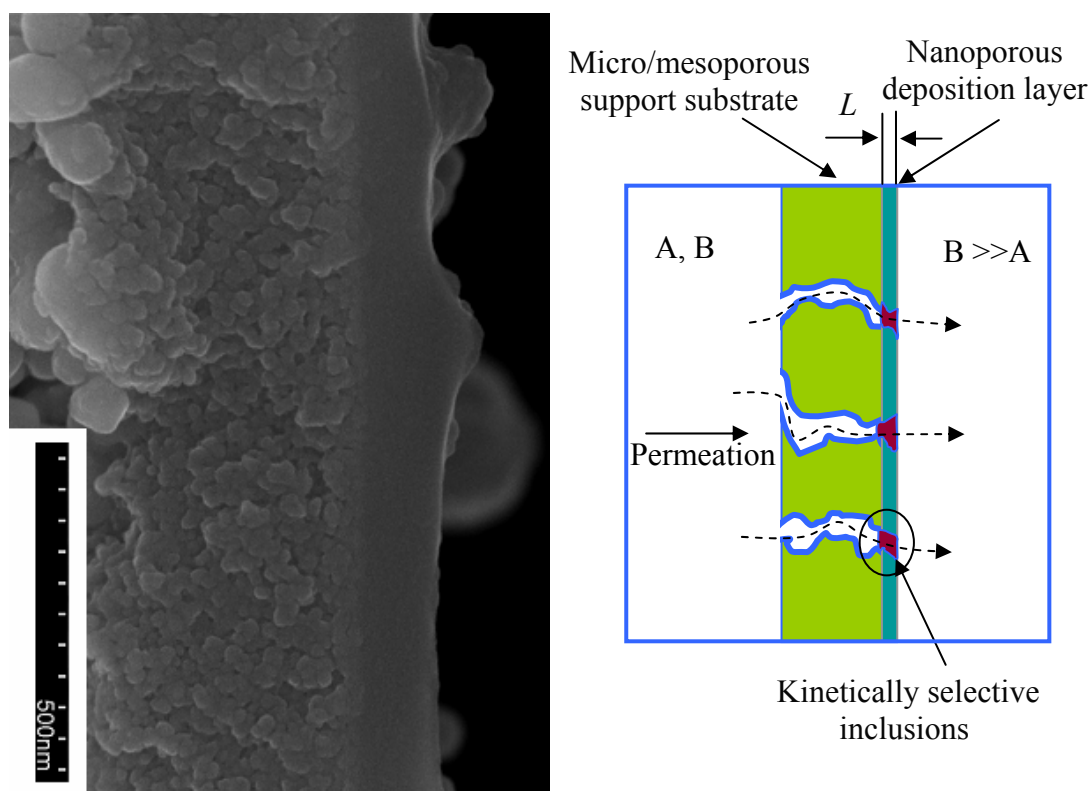


Figure 4.1 (Left) SEM image of a thin film of SiO_2 deposited onto a substrate composed of a secondary 500 nm SiO_2 layer (nominal pore size 1 nm), a microporous γ -alumina (nominal pore size 5-7nm) and a mesoporous α -alumina (nominal pore size in the micron range). The outermost layer on the right of the SEM image is the primary permselective SiO_2 film which is 100 nm in thickness with a nominal pore size of 0.4 nm. (Right) A schematic drawing of the principal elements of a permselective membrane.

In recent work on permeation within composite thin silica membranes (Lee et al (2004) and Araki et al (2007)) very similar to those depicted in Figure 4.1, two important observations may be drawn from the reported results:

- (1) For a range of simple gases (He, H₂, CO, CO₂ and CH₄) their permeance within composite films of silica prepared via chemical vapour deposition of alkoxysilanes decreased exponentially with increasing thickness of the deposited film.
- (2) All gases indicated a finite, non-zero permeance for the thickest SiO₂ films deposited.

In these studies and in other work reported earlier by Gavalas and coworkers (1994, 1995, 1997 and 1998) the primary goal has been to develop the fabrication protocols for composite membranes whose end use is for the separation of H₂ from high temperature process gas streams. Since the focus has been on Hydrogen, which has a small kinetic diameter relative to the other process gases, the objective of high permselectivity has been achieved with relative ease. However, the results reported by Lee et al (2004) and Araki et al (2007) clearly suggest that if optimally designed membranes are to be fabricated for gas mixture separation (and particularly for ‘difficult’ mixtures such as CO₂, O₂ and N₂ in high temperature post-combustion or oxy-fuel carbon capture technologies) then *ultrathin* permselective coatings as shown in Figure 4.1 with thicknesses less than 25-50 nm will need to be produced. This will require an understanding of the underlying mechanism for the observed exponential dependence of the permeance on membrane thickness as mentioned above in point 1 (for example it is noted that

the CO₂, CO and CH₄ permeances reported by Lee et al (2004) varied by 5-6 orders of magnitude as the thickness of the deposited nano-membrane increased from 0 to 30nm. Very similar results were reported by Araki et al (2007) and no explanation for this was offered by either source).

In prior studies (MacElroy (2002), Cuffe et al (2006)) of diffusion and mobility within moderately dense silica media the permselective characteristics of CO₂, O₂ and N₂ were investigated. In this work it was shown that if the density of the silica medium is high enough the material becomes non-percolating for a silica system which is of infinite extent. The methods employed involved molecular dynamics simulation of fully atomistic models of the gas molecules diffusing through the interstices of static amorphous silica structures (also atomistically modelled). A set of results (Mooney et al (2004)) for the mean-square displacements of the molecular centres-of-mass of the trace gas species as a function of time, t , is reproduced in Figure 4.2 to illustrate this behaviour and the lines drawn in this figure correspond to a scaling theory approximation proposed by MacElroy (2002) (see also MacElroy et al (1999))

$$\left\langle |\Delta \mathbf{r}(t)|^2 \right\rangle \sim \frac{At^{2/d_w}}{1 + (A/6\ell^2)t^{2/d_w}} \quad (4.1)$$

The coefficient d_w is the fractal dimension of the random walk undertaken by a given particle ($d_w = 2$ for Fickian conditions) and the parameter ℓ characterises the maximum range of the particle displacements under nonpercolating conditions and is here referred to as the mean percolating cluster size. The parameter ℓ was estimated for a wide range of conditions and the results obtained are reproduced in

Figure 4.3 (Cuffe et al (2006)). The key point to note from these results is the existence of percolation thresholds for each of the three gases in the density region $0.52 < \rho_{SiO_2} / \rho_{Bulk SiO_2} < 0.56$ where $\rho_{Bulk SiO_2} = 2.2$ g/cc.

A more detailed non-equilibrium molecular dynamics analysis (MacElroy (2002)) of the steady state permeation characteristics of the three gases through membranes of *finite* thickness and densities greater than 56% of the bulk silica density demonstrated that the permeance of the gases are well described by the simple expression

$$P_i = \left[\chi_i \sqrt{1/2\pi M_i RT} \exp(\delta_i/\ell_i) \right] \exp(-L/\ell_i) \quad (4.2)$$

where χ_i is the nanopore accessibility coefficient for the distribution of molecules of species i between the bulk gas and the membrane surface (this is distinct from the adsorption equilibrium coefficient) and M_i is the molecular weight of the gas. The parameter δ_i represents the length scale of the interfacial inhomogeneities which exist at the surface of the membrane and are of order 0.3-0.6 nm for the membranes models employed by MacElroy (2002).

Equation (4.2) can provide a partial explanation for the observations reported by Lee et al (2004) and Araki et al (2007) but there are issues which need to be resolved. It is known that the densities of thin selective silica films of the type shown in Figure 4.1 formed by CVD or related methods lie in the range 2.0-2.2 g/cc (McCann (2010)). Furthermore, since the permeance of the membranes reported by Lee et al (2004) and Araki et al (2007) for molecular species such as

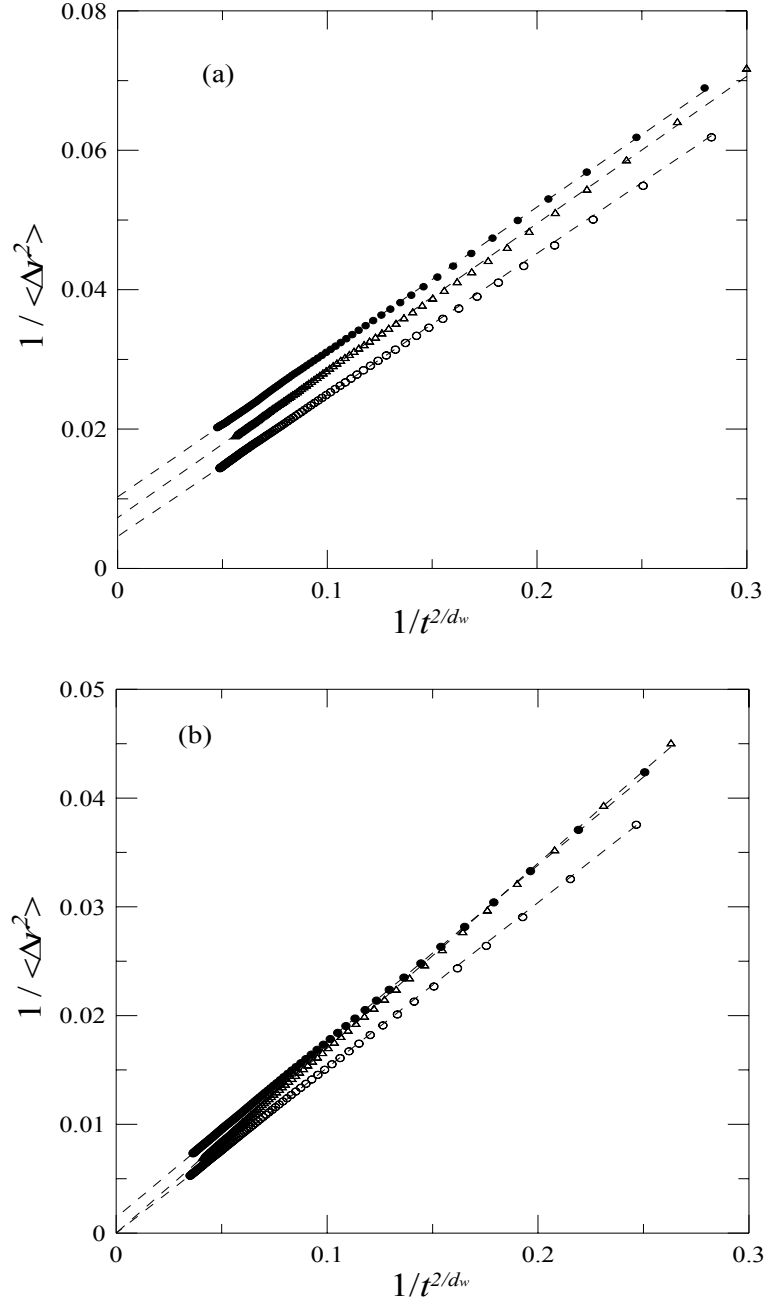


Figure 4.2: Inverse mean square displacements (MSDs) of the centre of mass of the trace gas species as functions of $1/t^{2/d_w}$. (a) $\rho_{SiO_2} / \rho_{Bulk SiO_2} = 0.6476$, \bullet N_2 ($d_w = 3.62$), \circ O_2 ($d_w = 3.65$), Δ CO_2 ($d_w = 3.82$); (b) $\rho_{SiO_2} / \rho_{Bulk SiO_2} = 0.5496$, \bullet N_2 ($d_w = 3.33$), \circ O_2 ($d_w = 3.29$), Δ CO_2 ($d_w = 3.45$). The dashed lines in each case represent the non-linear regression fits of Equation (4.1) (Reproduced from Mooney et al (2004)).

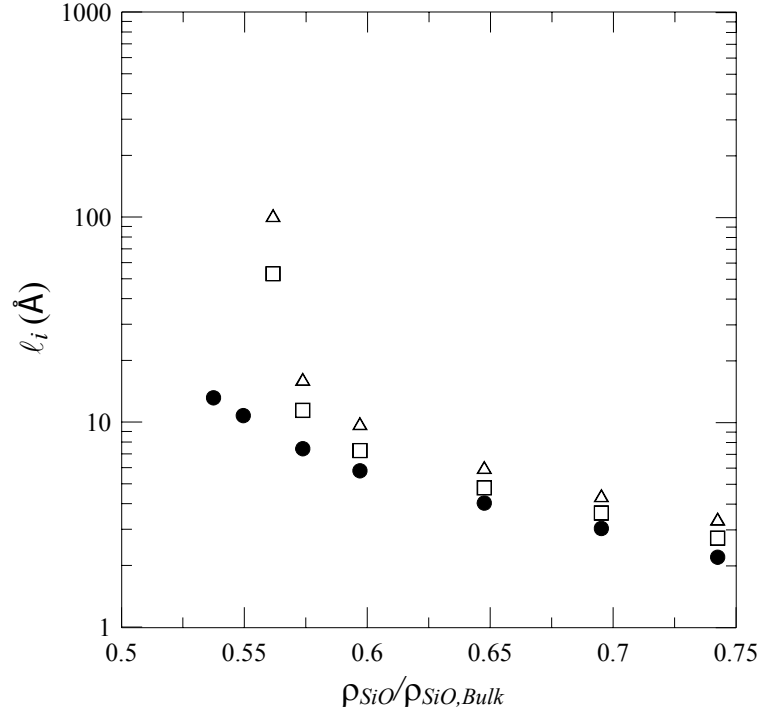


Figure 4.3. The average percolation cluster size for O_2 (Δ), CO_2 (\square) and N_2 (\bullet) as functions of the relative density of the nanoporous silica medium (reproduced from Cuffe et al (2006)).

CO_2 and N_2 are implied, by extrapolation, to be non-zero at infinite thickness, Equation (4.2) is incomplete.

There were two major assumptions inbuilt in the silica models investigated by MacElroy (2002), Mooney et al (2004) and Cuffe et al (2006):

(1) The porous silica media were generated by randomly etching bulk amorphous silica of density 2.2 g/cc. During the etching process care was exercised vis-à-vis the creation of surface silanols however the resulting porous medium was otherwise random. No criterion to ensure bond connectivity within the network of silica tetrahedra was included and it is known that a random structure of this type

with isolated clusters of silica can display percolation thresholds for diffusion which are at significantly lower densities than might be expected (Park and MacElroy (1989)).

(2) To simplify the computation, the silica models employed in this earlier work were static. This is a condition which cannot be assumed to hold for small molecule transport within pores which are very close to the size of the gas molecule itself.

In this chapter, the above assumptions are addressed and molecular dynamics simulations have been performed to recompute the MSDs for three gas species (He, N₂ and CO₂) diffusing within silica media composed of bonded networks of fully mobile atomistic SiO_x ($x > 2$ in view of the presence of OH groups within the systems investigated).

4.2 Simulation Methodology

4.2.1 Low-to-Moderate Density Silica Structures

The primary issue involved in the creation of atomistic models of moderate density solid substrates is the problem of maintaining the bond connectivity of the structure within the fundamental cell and across the system periodic boundaries as well as identifying ‘floating’ components of the structure (groups of atoms which have become detached from the main structure). This is solved here using a non-lattice version of the Hoshen-Kopelman (1976) cluster counting algorithm (see Chapter 2). The creation of lower density structures is carried out in two parts:

(a) Removal of atoms until a specified density is reached, ensuring that the system remains fully coordinated (no dangling bonds), and fully connected (no floating clusters).

(b) Checking that if the structure is periodically replicated in the x, y, and z directions there is only one connected molecular network.

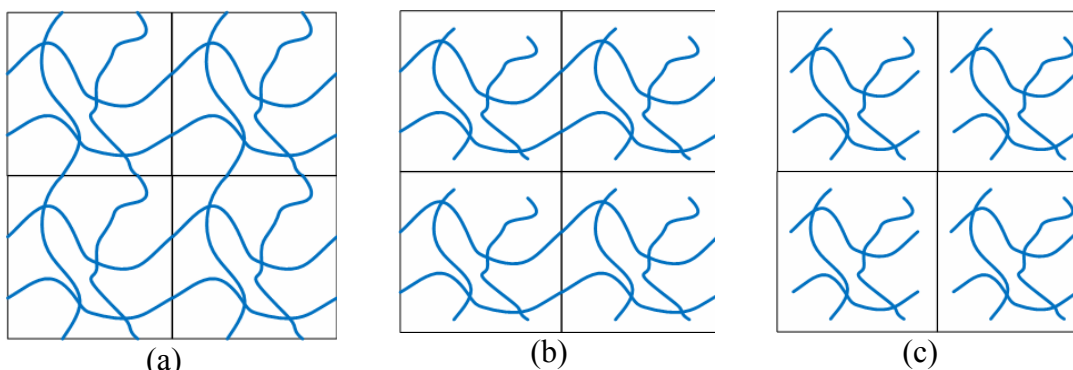


Figure 4.4. Two dimensional representations of periodically replicated clusters (a) spanning x and y dimensions, (b) spanning x dimension only (slabs), (c) isolated, does not span x or y dimensions (islands).

The condition to be satisfied in part (b) above is illustrated in Figure 4.4 where the required structures are those illustrated in Figure 4.4 (a) which span across all the periodic boundaries. Structures which are disconnected in one or more of the periodic dimensions, would result in the replicated system being composed of separated slabs, columns, or isolated islands as illustrated in Figures 4.4 (b) and (c), and are not allowed.

Pseudo code describing the etching in part (a) is given in Figure 4.5(a) below. Note that the full version of the non-lattice Hoshen-Kopelman algorithm is not required to check the connectivity of the molecular network – only the nodes

(corresponding to the atoms here) in the original algorithm are used with the links may be omitted and use a simplified form of the algorithm. Hence the labeling algorithm HKNonLattice required for the etching process only requires the atom connectivity table (and the number of atoms) as input.

The pseudo code for part (b) is given in Figure 4.5(b) below. The list of bonds which cross the period boundaries of the system are easily obtained by considering if the components of the separation vector \mathbf{r}_{ij} are greater than half the box length L as shown in Figure 4.6. Figure 4.7 shows a two dimensional illustration of the lists of boundary crossing bonds, and some examples of molecular clusters found in the system when the periodic boundary conditions have been switched off. For example cluster A crosses the periodic boundary in the x direction through the bond between atoms 1 and 8. Cluster B1, B2, and B3 cross the boundaries in the x and y directions in such a way that when the periodic boundary conditions are taken into account they are seen to belong to the one cluster as illustrated in Figure 4.8 where the simulation box from Figure 4.7 is shown surrounded by the neighbouring periodically imaged cells.

Figures 4.6, 4.7, and 4.8 show that in order to determine if a molecular cluster spans the simulation box in a particular dimension the periodic boundary conditions in that dimension can be switched off (keeping the periodic boundary condition in the other dimensions) with a subsequent check if the atoms in the boundary crossing bond still have the same cluster number. For example, consider the three clusters B1, B2, B3 shown in Figures 4.7 and 4.8 which are found when the periodic boundary conditions are switched off in both the x and y directions.

```

ETCHING_PROCEDURE_A Removes atoms to create a required lower density structure
                                ensuring that the final structure is fully connected.
i.e.
                                there are no isolated (floating) clusters of atoms.

INPUT:
    Natom    Number of atoms in the structure
    L        Length of the sides of the cubic box
    rxyz     Positions of the atoms in the system
    atom     List of the type of each atom in the system
    connectivity Connectivity table for the system
    frem     Fractional density (weight) required for initial etching

OUTPUT:
    Final structure (atom coordinates, atom types, and connectivity table),
    and density of etched system

REQUIRED FUNCTION:
    HKNonLattice(N,connectivity,n_cluster,atomL)
        ! A non-lattice cluster labeling algorithm
        INPUT:    N, connectivity Connectivity table of size N
        OUTPUT:  n_cluster Number of clusters
        atomL List of cluster labels

BEGIN:

    Label atoms and count clusters using the connectivity table.
    Store the silicon atom numbers in a list.
    Check that there is initially only one cluster.

    ! Perform the etching
    etching: do

        Pick a random Silicon to delete from the silicon list
        Store the old configuration !(as we may have to undo this removal)
        Delete the chosen silicon atom
        Remove any unconnected oxygens
        Convert any singly bonded oxygens to OH oxygens
        Label the atoms and count the clusters.

        if more than one cluster then
            ! We cannot remove the selected silicon so it is removed
            ! from the list
            Remove the selected silicon from the silicon list.
            Restore the previous configuration.
            Jump back to the top of this etching loop
        end if

        Check the structure is still consistent.
        Calculate the new fractional mass density.
        if the density is low enough then exit this loop

    end do etching

END

```

Figure 4.5 (a). Etching algorithm (part A)

ETCHING_PROCEDURE_B *Checks the input structure to find spanning clusters which cross all the periodic faces so that when the structure is imaged in a given dimension there is still only one connected structure. The structure composed of the first spanning cluster found is returned.*

INPUT:

Natom *Number of atoms in the structure*
 L *Length of the sides of the cubic box*
 rxyz *Positions of the atoms in the system*
 atom *List of the type of each atom in the system*
 connectivity *Connectivity table for the system*

OUTPUT:

Final structure (atom coordinates, atom types, and connectivity table), and density of etched system.

MAIN WORK ARRAYS REQUIRED:

crossbond_x *A List of bond numbers cross the x-z faces of the cube. As these bonds are broken when the PBC in the x-direction is removed they are named crossbond_x*
 crossbond_y *The y periodic crossbonds*
 crossbond_z *The z periodic crossbonds*
 cluster_list_x *A List of the cluster labels which span the x-direction*
 cluster_list_y *A List of the cluster labels which span the y-direction*
 cluster_list_z *A List of the cluster labels which span the z-direction*
 connectivity_nopbc *The connectivity table when the Periodic Boundary Conditions (PBC) are switched OFF*
 ibond *An array holding the atom numbers of each bond*

REQUIRED FUNCTION:

HKNonLattice: *A non-lattice cluster labeling algorithm (as in part A).*

BEGIN:

Label atoms and count clusters using the connectivity table.
 Store the silicon atom numbers in a list.
 Create a bond list array ibond.
 Check the distance between bonded atoms with the PBC switched OFF and generate the lists crossbond_x, crossbond_y, crossbond_z, of the bond numbers which cross the faces of the simulation box, and the connectivity table connectivity_nopbc for the non periodic system.
 Label atoms and count clusters for this non periodic connectivity.
 Make a list of those cluster labels which span the x periodic dimension by checking the atom cluster labels of the atoms in each crossbond_x.
 If both atoms in a crossbond_x have the same cluster number then that cluster spans the x dimension and the cluster number is added to the list cluster_list_x
 Repeat the previous step to generate the list cluster_list_y of n_cluster_y cluster labels and cluster_list_z of n_cluster_z labels
 Examine the three spanning cluster label lists to find the cluster which spans all three dimensions.
 If no spanning cluster was found then report failure and stop.
 Relabel the atom clusters, this time with the PBC switched back ON.
 Delete all atoms that are not in the spanning cluster.
 Check and save the structure.
END

Figure 4.5(b) Etching algorithm (part B)

To check for connectivity in the y direction, the case where only the y periodic boundary condition is switched off is examined. In this case B3 is connected to B2 (through bond 5 - 12) and B2 to B1 (through bond 10 - 3) and so B1, B2, and B3 are a single cluster, although atoms 11 and 4 are no longer connected (since the y periodic boundary is removed) they have the same cluster number and hence this cluster spans the simulation cell in the y dimension. Now consider the case where the x periodic boundary condition is removed (and y switched back on). It is observed that B1 and B3 form a single cluster, but this is disconnected from B2, so that these clusters do not span the simulation cell in the x direction. Similarly it is noted that clusters C1 and C2 (which were a single cluster crossing the periodic boundary in the x direction) are now disjoint clusters and so do not span the simulation cell in the x direction.

To check structures of lower but not very low density (down to 70% say) it is usually not necessary to carry out a detailed analysis to check the spanning in each dimension (turning off one periodic boundary condition at a time) and instead all the periodic boundary conditions may be switched off and one can check for a cluster that still spans all three dimensions.

Starting with a periodically imaged, amorphised silica structure of density 2.2 g/cc (see MacElroy and Raghavan (1990)) and dimensions 3.56643^3 nm^3 , the above algorithm has been applied to generate silica structures with densities 1.73 g/cc, 1.86 g/cc, 1.97 g/cc and 2.03 g/cc. Initial etching runs were conducted (with

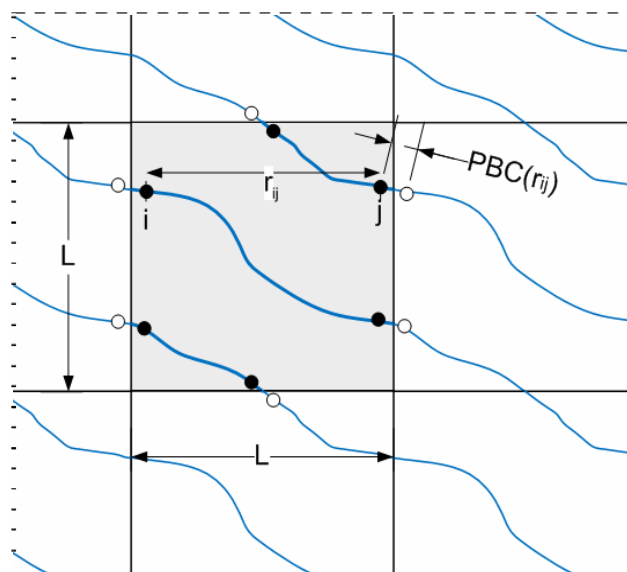


Figure 4.6 A two dimensional representation of the periodic system showing the variables required for determining the bonds which cross the system boundaries. The cluster shown spans both the x and y periodic dimensions, however if the x periodicity is switched off then the resulting two clusters (the top and bottom clusters are joined in the y periodic dimension) do not span the y periodic dimension, but do span the x periodic dimension.

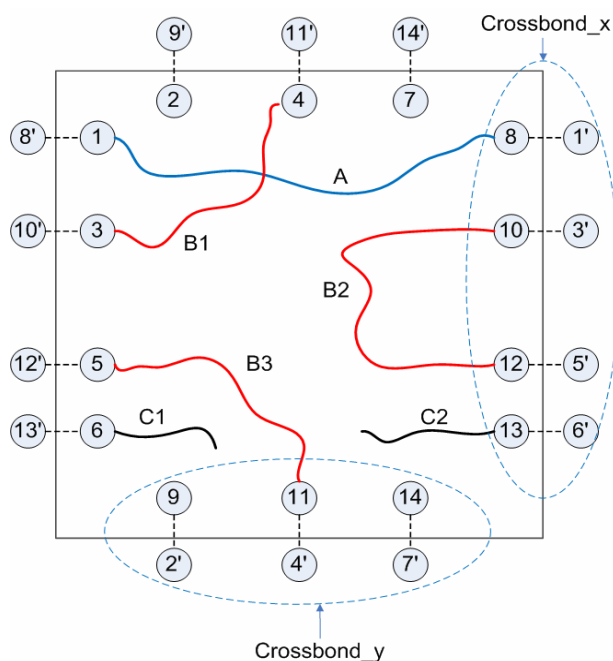
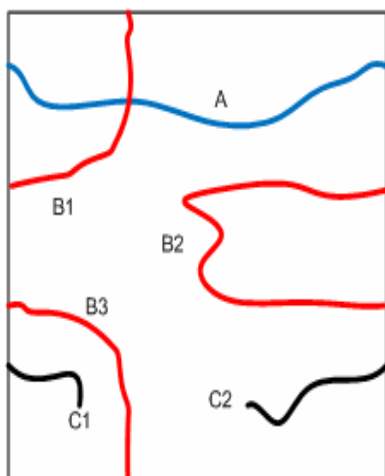
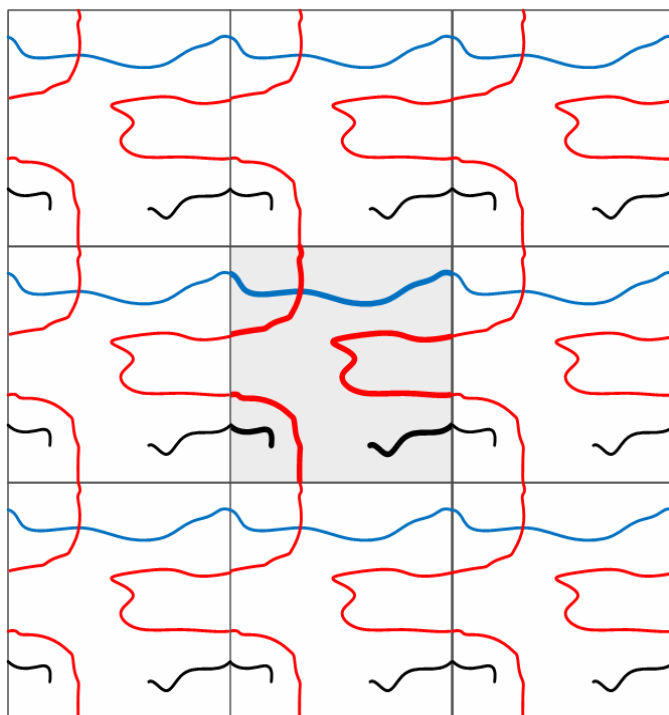


Figure 4.7. Boundary crossing bond in a 2D representation of clusters in a unit cell.



(a) A 2D representation of some molecular clusters in a unit cell with the Periodic Boundary Conditions (PBC) switched off. Note cluster A and B1 are distinct - they are considered to be on different z levels in the actual 3D system.



(b) The unit cell depicted in (a) is highlighted in the central cell which is surrounded by the periodically imaged neighbouring cells.

Figure 4.8. Two dimensional representations of clusters in a periodic system.

When the x-periodicity is switched off then the black segment in part (b) which crosses the x periodic boundary is broken into the two clusters C1 and C2 shown in (a). Removal of the x periodicity also causes the y periodic dimension spanning red segment shown in part (b) to split into the three clusters C1, C2, and C3 which do not span. The cluster marked A spans the x periodic dimension when both the x and y periodicities are switched off.

ρ_{SiO_2} (g/cc)	x_{Si}	x_O	x_{OH}	R_p (nm)
1.73	0.307	0.532	0.161	0.128
1.86	0.314	0.571	0.115	0.115
1.97	0.320	0.600	0.0801	0.105
2.03	0.325	0.625	0.0495	0.0997
2.2	0.333	0.667	0.0	0.0935

Table 4.1 The number fractions of silicon, siloxane (doubly bonded) oxygens, silanol groups and the average pore radii of the silica structures employed in the MD simulations.

full bond connectivity) to determine the appropriate level of silicon atom removal, with subsequent condensation of a prescribed set of dangling $|\text{-Si-O}$ bonds (modelled as silanols), which would lead to the desired target density. In all cases the prescription applied for the level of ‘silanol’ condensation was that all dangling oxygens created as a result of the raw etching process which were within 0.28 nm of each other (which is fractionally larger than the oxygen nearest neighbour distance in bulk silica) were ‘condensed’ with the removal of one of the oxygens in every given pair. For each pair of dangling bonds condensed, 10^5 Metropolis Monte Carlo relaxation steps were undertaken for the silica system locally within a range of 1 nm of the site of a given condensation. Selected average properties for each of these structures, determined from samples of 25 configurations each for the four system densities, are provided in Table 4.1. The average pore radii were determined using the technique described by Bhattacharya and Gubbins (2006) and this methodology will be described in some detail later in Chapter 6.

4.2.2 The Molecular Dynamics Method and Potential Functions

The molecular dynamics method employed in this work for the fully atomistic structures involved was the velocity Verlet algorithm (see Chapter 2) with a time step of 0.5 fs. An initial period (100 ps) for equilibration was employed with velocity rescaling and thereafter the trajectories evolved within the microcanonical ensemble. All of the trajectories were of 2.5 ns duration for each of the 50 gas particles, inserted randomly into each of the 25 silica configurations, and the mean-squared displacements of the centres-of-mass of the particles were evaluated over 0.5 ns with equal weight given to each data point.

In the computations the gas species are treated as ideal gases, i.e. there are no explicit interactions between the gas molecules within any given silica configuration, and the individual atom-atom pair interactions are considered to be composed of both intermolecular non-bonded terms and intramolecular contributions. Note that to ensure no distortions arise locally within the solid, the initial insertions of the gas particles are conducted in such a way that no two gas particles are within a molecular diameter of one another.

The non-bonded interactions are described by Lennard-Jones $U_{LJ}(r_{ij})$ and Columbic $U_{el}(r_{ij})$ (partial charge) potential terms

$$U(r_{ij}) = U_{LJ}(r_{ij}) + U_{el}(r_{ij}) \quad (4.3)$$

The Lennard-Jones interaction is

$$U_{LJ}(r_{ij}) = 4\varepsilon_{ij} \left(\left(\frac{\sigma_{ij}}{r_{ij}} \right)^{12} - \left(\frac{\sigma_{ij}}{r_{ij}} \right)^6 \right) \quad (4.4)$$

where r_{ij} is the distance between atoms i and j , ε_{ij} represents the magnitude of the minimum in well-depth and the distance σ_{ij} characterizes the separation between the two atoms at which repulsion dominates the interaction. A cut-off radius for the Lennard-Jones interaction of 1.2 nm was employed in the simulations.

In the evaluation of the interactions between the partial charges on the gas molecules and the charges within the silica system, the Coulombic potential in its screened form as proposed by Wolf et al (1999) is employed in this work (full details will be provided on this potential later in Chapter 5). In these computations the following simplified form which is known to be accurate (Carré et al (2007)) was utilised

$$U_{el}(r_{ij}) = \frac{q_i q_j}{4\pi\varepsilon_0} \left(\frac{1}{r_{ij}} - \frac{1}{R_c} + \left\{ \frac{1}{R_c^2} \right\} (r - R_c) \right) \quad (r_{ij} \leq R_c) \quad (4.5)$$

where r_{ij} is the distance between two partial atomic charges q_i and q_j on particles i and j respectively, ε_0 is the electrical permittivity of space and the cut-off R_c was set equal to 1 nm.

The Lennard-Jones and electrostatic (partial charge) parameters on each atom used in the model systems are reported in Table 4.2. In this work the OH groups are treated as united atom structures with the charge on the OH group defined by

combining the individual charges on the oxygen and hydrogen atoms. To assign the charge on the surface silicon atoms, q_{Si} , a simple formula has been employed which is given by

$$q_{Si} = -q_{OH} * (N_{OH}) - q_{O(Siloxane)} * (N_{O(Siloxane)}) \quad (4.6)$$

The intramolecular bonded interactions in the silica media are computed using the Keating Si-O bond stretching and O-Si-O, Si-O-Si bond angle bending interaction potential (Keating (1966) and von Alftan et al (2003)). This potential represents the energy of the solid as a function of the nearest neighbor positions and is given (in its simplified form (Keating (1966)) by

$$E = \sum_{i \in bonds} \frac{1}{2} k_i^b [r_i - r_{i0}]^2 + \sum_{ij \in angles} \frac{1}{2} k_{ij}^a [\cos \theta_{ij} - \cos \theta_{ij0}]^2 \quad (4.7)$$

Atom	ε/k_B (K)	σ (nm)	Charge, $q_i(e_o)$
O(silica)	185.0	0.2708	-0.64025
Si	0.0	0.0	+1.2805
O(OH)	185.0	0.3	-0.533
H(OH)	0.0	0.0	+0.206
He	10.22	0.228	0.0
N(q ^a)	34.897	0.33211	-0.5475 (+1.095) ^a
O (CO ₂)	82.997	0.3064	-0.33225
C	29.999	0.2785	+0.6645

Table 4.2. Lennard-Jones and Coulombic partial charge parameters (from Schumacher et al (2006a,b) and Chakravarty (1997)). See also MacElroy and Raghavan (1990)).

^aThe charge +1.095 is the charge on the centre-of-mass required to reproduce the quadrupole moment on N₂

In Equation 4.7, r_i is the distance between two bonded atoms, r_{i0} is the (average) equilibrium length of bond i , θ_{ij} represents the bond angle between bonds i and j and θ_{ij0} is the corresponding equilibrium value. k_i^b and k_{ij}^θ are the bond stretching and bond bending force constants respectively.

The parameters of the Keating potential for the silica system and for the intramolecular modes of N₂ and CO₂ (also evaluated using the functional form in Equation (4.7)) are provided below in Table 4.3. In the case of CO₂ the mathematical form of the bond angle bending potential for bonds i and j appearing in Equation (4.7) is replaced by (Mayo et al (1990))

$$U_{ij,Bend} = \frac{1}{2} k_{ij}^\theta (\theta_{ij} - \theta_{ij0})^2$$

Atomic interaction	Bond stretching constant (MJ/mol/nm ²)	Bond bending constant (kJ/mol)	Equilibrium distance (nm)	Angle (°)
Si-O	260.6		0.161	
Si-O-Si		193		$\theta_{Si-O-Si,0} = 144$
O-Si-O		417		$\theta_{O-Si-O,0} = 109.471$
N-N	292.9		0.10464	
C-O	585.8		0.1161	
O-C-O		418		$\theta_{O-C-O,0} = 180$
Si-OH	292.9		0.1487	

Table 4.3. Bonded intramolecular potential parameters.

A repulsive potential (von Alfthan et al (2003)) is also used along with the Keating potential in this study to prevent the overlapping of unbonded atoms during relaxation of the structure. This potential acts between atoms and does not consider nearest or second nearest neighbours with respect to the bond topology. The form of the repulsive potential selected to calculate the repulsive interaction in this work is

$$U_r = \begin{cases} \frac{1}{2} \sum_{i,j} k^r [r_{ij}^2 - r_c^2]^2, & r_{ij} < r_c \\ 0, & r_{ij} \geq r_c \end{cases} \quad (4.8)$$

where U_r is the repulsive energy between two atoms, k^r is the spring constant and r_c is a cut off radius. In this study the radius of the interaction has been chosen to be 0.26 nm which is the distance between the nearest neighbour oxygen atoms in silica and the spring constant k^r was set to $8000 \text{ eV/nm}^4 = 772 \text{ MJ/mol/nm}^4$.

4.3 Modelling

The underlying premise of the analysis leading to Equations (4.1) and (4.2) is believed to be fundamentally correct with one exception: in order to satisfy observations that normal Fickian diffusion (no matter how slow) of simple gas species can take place within silica films of the type shown in Figure 4.1 an additional term (or terms) must be included within the analysis. A model which extends the prior analysis leading to Equation (4.2) is described in the following.

The structure depicted in Figure 4.9 contains two primary domains, the grey area which represents a poorly conducting region and the white ‘channels’ which have a conductance much larger than the grey domain. As described by Havlin and Bunde (1991), random walkers within the white ‘channels’ very rapidly sample the configurational space of any given cluster within this domain. Their transfer to the poorly conducting domain is extremely slow and will only occur during a time scale of the order of t_X or greater as indicated in Figure 4.9(b).

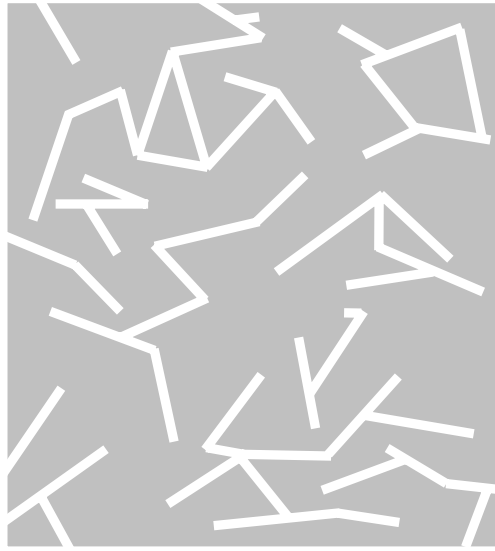


Figure 4.9(a) ‘Superconducting’ clusters (white) / poor conductor (grey) mixture

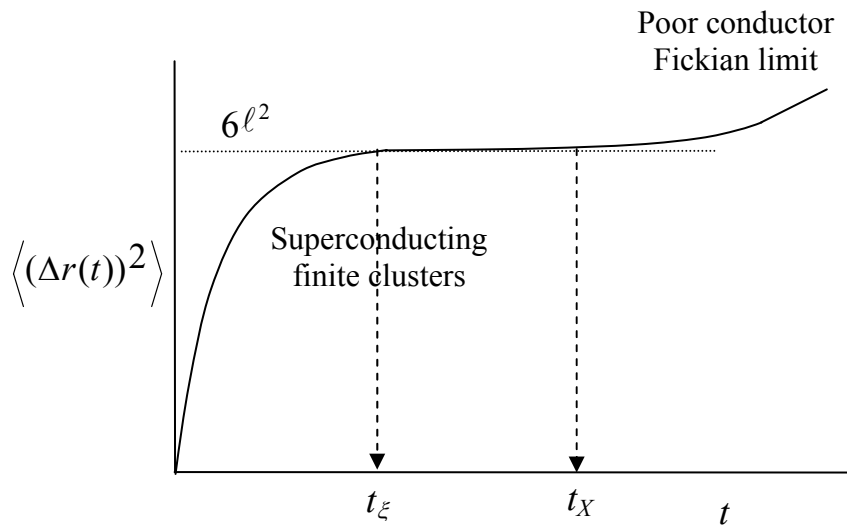


Figure 4.9(b) Schematic drawing of the MSD of a random walker diffusing within the medium illustrated in Figure 4.9(a)

At short times the walker moves on the finite (white) clusters and the MSD is considered to be described by Equation (4.1) during this time range (note that at very short times the MSD will be proportional to t^2 in the ballistic regime). For $t_\xi < t < t_X$ The MSD saturates at the value $6\ell^2$ in 3-dimensions. At intermediate-to-long times the random walker transfers into the grey domain and slowly diffuses through the medium. A simple extension of Equation (4.1) is

$$\langle |\Delta \mathbf{r}(t)|^2 \rangle = \frac{At^{2/d_w}}{1 + (A/6\ell^2)t^{2/d_w}} + 6Dt \quad (4.9)$$

where D is the long time diffusivity of the gas species within the poorly conducting domain. Noting that the interrelationship between the autocorrelation function of the centre-of-mass velocity (VACF) of the gas molecules and the centre-of-mass MSD is given by

$$\frac{1}{2} \frac{d \langle |\Delta \mathbf{r}(t)|^2 \rangle}{dt} = \int_0^t \varphi(\tau) d\tau \quad (4.10)$$

one may then consider two contributions to the VACF representing both of the additive terms appearing in Equation (4.9) i.e.

$$\varphi(t) = \varphi^{(\xi)}(t) + \varphi^{(X)}(t)$$

For one-dimensional diffusion through membranes of the kind illustrated in Figure 4.1 one has

$$\begin{aligned}
J(z, t) &= - \int_0^t \varphi(t - \tau) \frac{\partial c(z, \tau)}{\partial z} d\tau \\
&= - \int_0^t \varphi^{(\xi)}(t - \tau) \frac{\partial c(z, \tau)}{\partial z} d\tau - \int_0^t \varphi^{(X)}(t - \tau) \frac{\partial c(z, \tau)}{\partial z} d\tau
\end{aligned} \tag{4.11}$$

The first term on the right corresponds to the ‘superconducting’ flux and, following on from the analysis reported by MacElroy et al (1999) and MacElroy (2002) for $L > \ell$ under stationary conditions, this term is simply given by Equation (4.2) multiplied by the concentration difference across the membrane, namely

$$J^{(\xi)} = \left[\chi \sqrt{RT / 2\pi M} \exp(\delta/\ell) \right] \exp(-L/\ell) \Delta c^{Bulk} \tag{4.12a}$$

In the stationary limit the second term on the right of Equation (4.11) simply provides the Fickian term

$$J^{(X)} = DK \frac{\Delta c^{Bulk}}{L} \tag{4.12b}$$

where K is the equilibrium adsorption coefficient of the gas. Combining gives the general expression for a single ideal gas species

$$J = P \Delta p$$

where Δp is the pressure difference across the membrane and P is the permeance

$$P = \left[\chi \sqrt{\frac{1}{2\pi MRT}} \exp(\delta/\ell) \right] \exp\left(-\frac{L}{\ell}\right) + \frac{DK}{RTL} \tag{4.13}$$

In Section 4.4 below the expression presented in Equation (4.9) is used to correlate MSD data generated as outlined earlier for diffusion of the three gases He, N₂ and CO₂ in silica media at bulk densities of 1.73 g/cc, 1.86 g/cc, 1.97 g/cc, 2.03 g/cc and 2.2 g/cc (He only). In this work attention is solely focussed on Equation (4.9). Equation (4.13) and its implications for the analysis and assessment of permselectivity of silica membranes will be considered briefly in the concluding section of Chapter 6.

4.4 Results and Discussion

The results for the MSDs for each of the gases He, N₂ and CO₂ at the three temperatures 473K, 673K and 873K are reported in Figures 4.10 to 4.12. These MSDs were computed from 2.5 ns molecular trajectories and a nonlinear regression algorithm was employed to determine the four parameters, A , ℓ , d_w and D appearing in Equation (4.9).

The nonlinear regression was carried out using a version of the SOLVOPT program written by Kuntsevich and Kappel (2000) which implements the Shor (1985) algorithm. Versions of this program are available from the authors' website (Kappel and Kuntsevich (2000)), however the program used here was a Mathematica implementation developed in house. This allowed the results of the nonlinear fitting to be validated by comparison with the built in nonlinear solvers used in the Mathematica function NonlinearModelFit. The Mathematica code required to perform the fit is shown in Figure 4.13.

It was found necessary to use the numerical minimization NMinimize in order to obtain converged results, otherwise the Mathematica results were similar to those obtained from SOLVOPT, however the results from SOLVOPT usually produced the tightest fits and were more robust with respect to the changes in the parameters caused by eliminating points from the initial part of the curve from the region to be fitted. In all of the work reported below (with the exception of the analysis of the Helium MSDs as discussed in the following paragraph) the nonlinear fit was conducted for all data within the time range 10-500 ps.

Initial studies, employing this regression analysis for all four parameters resulted in significant scatter in the parameters themselves. For this reason the regression procedure was limited in two respects:

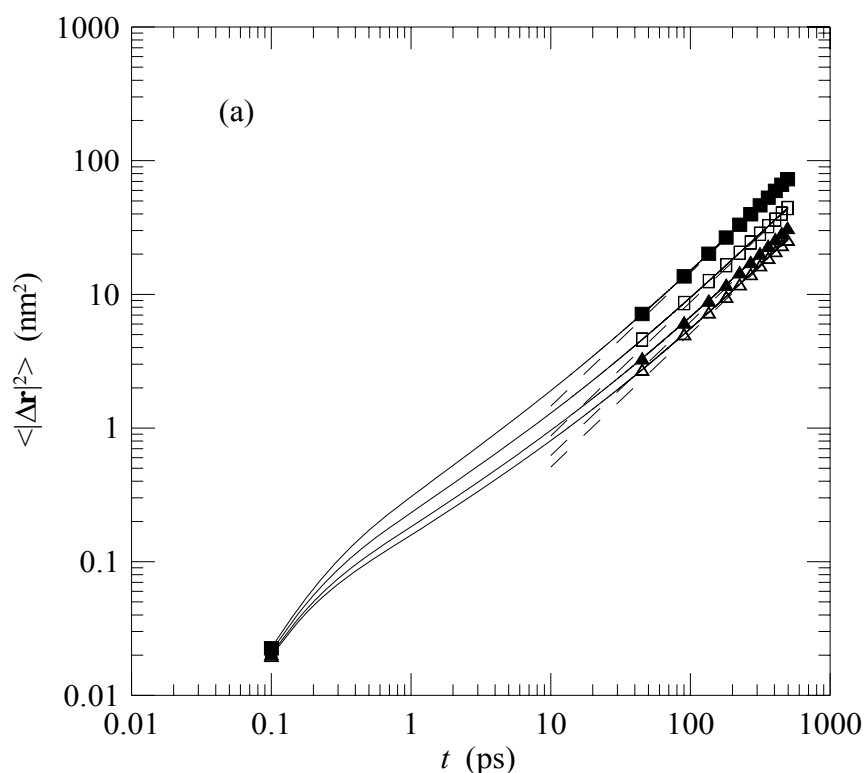


Figure 4.10(a). The mean square displacement of Helium atoms within moderate-to-high density nanoporous silica media at 473K. ■ 1.73 g/cc; □ 1.86 g/cc; ▲ 1.97 g/cc; △ 2.03 g/cc.

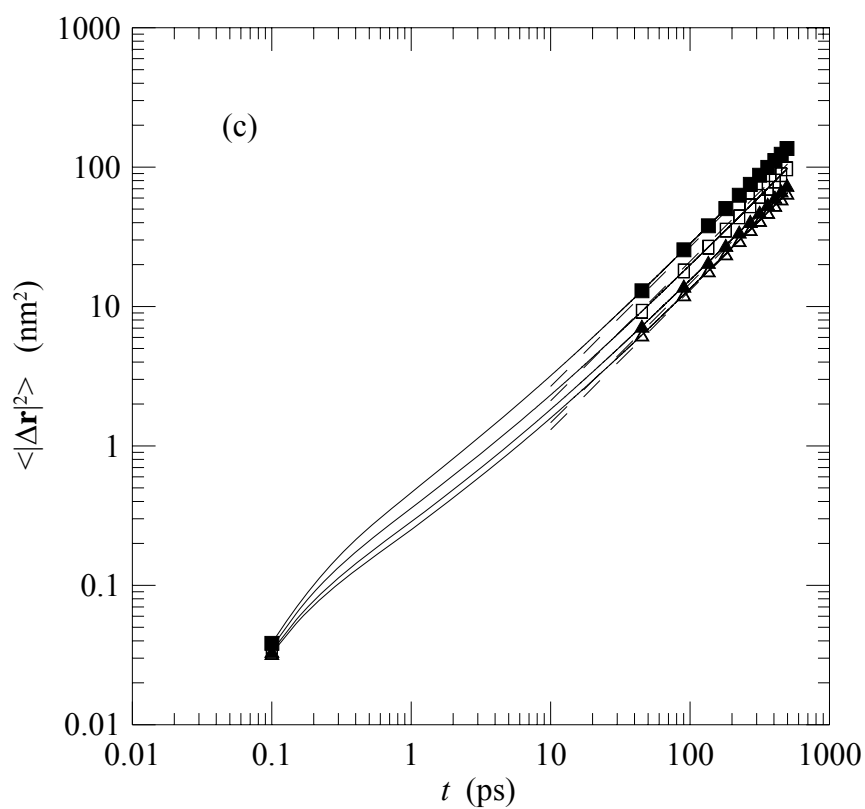
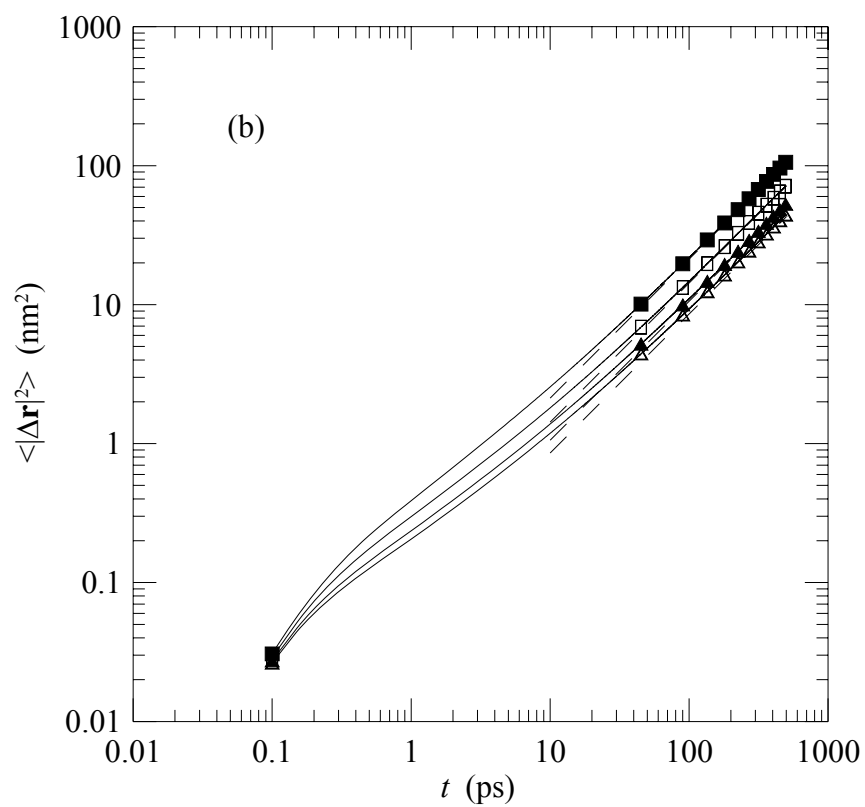


Figure 4.10(b,c). As in Figure 4.10(a) but for (b) 673K and (c) 873K.

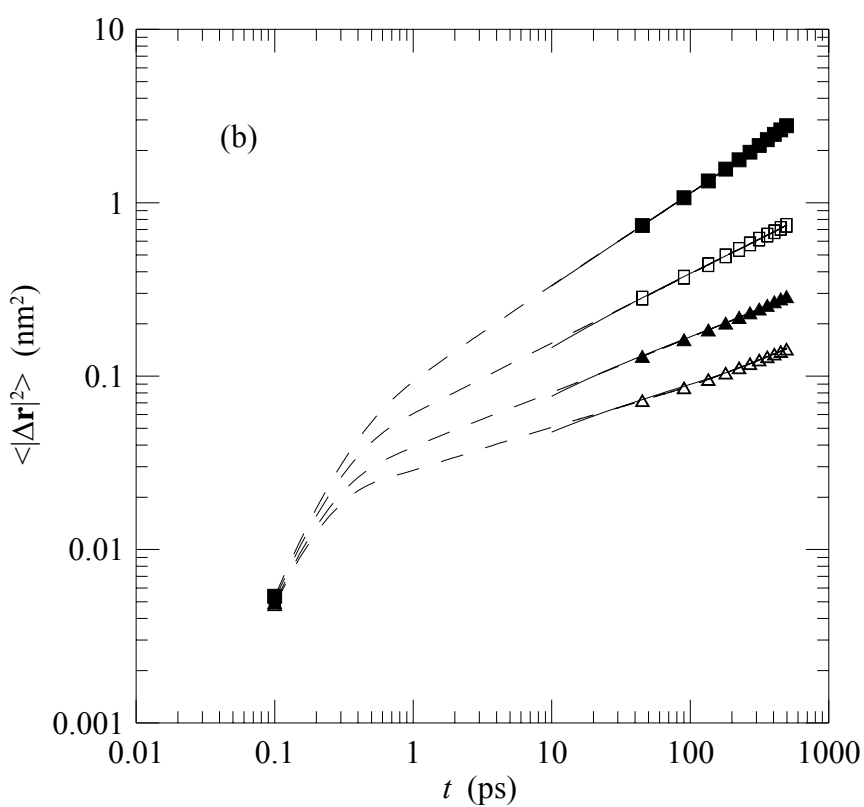
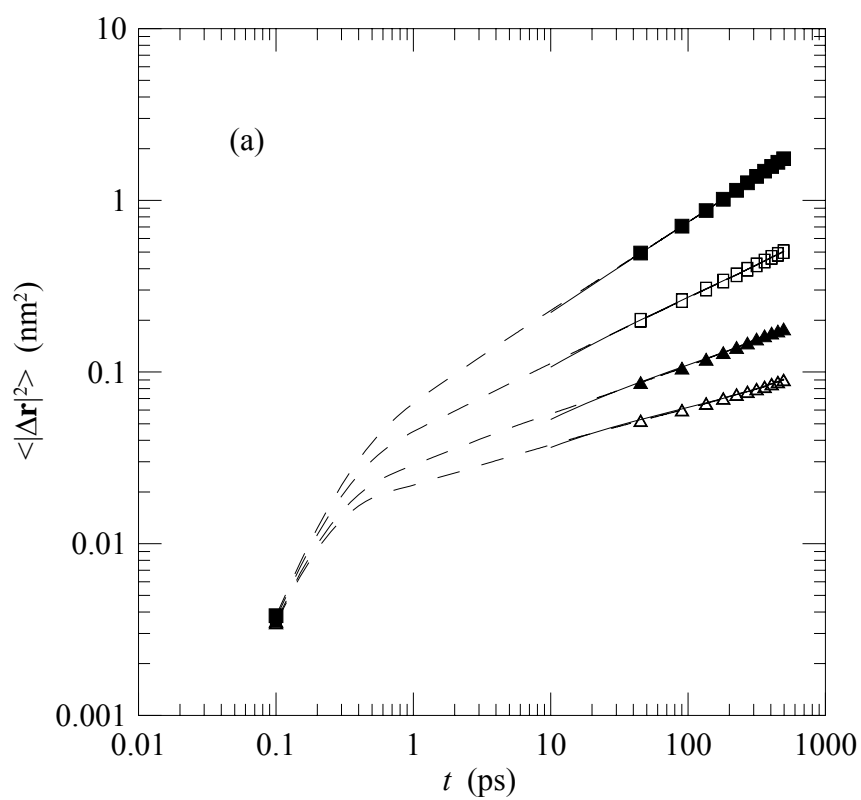


Figure 4.11(a, b). The mean square displacement of Nitrogen molecules within moderate-to-high density nanoporous silica media at 473K (a) and 673 (b). ■ 1.73 g/cc; □ 1.86 g/cc; ▲ 1.97 g/cc; △ 2.03 g/cc.

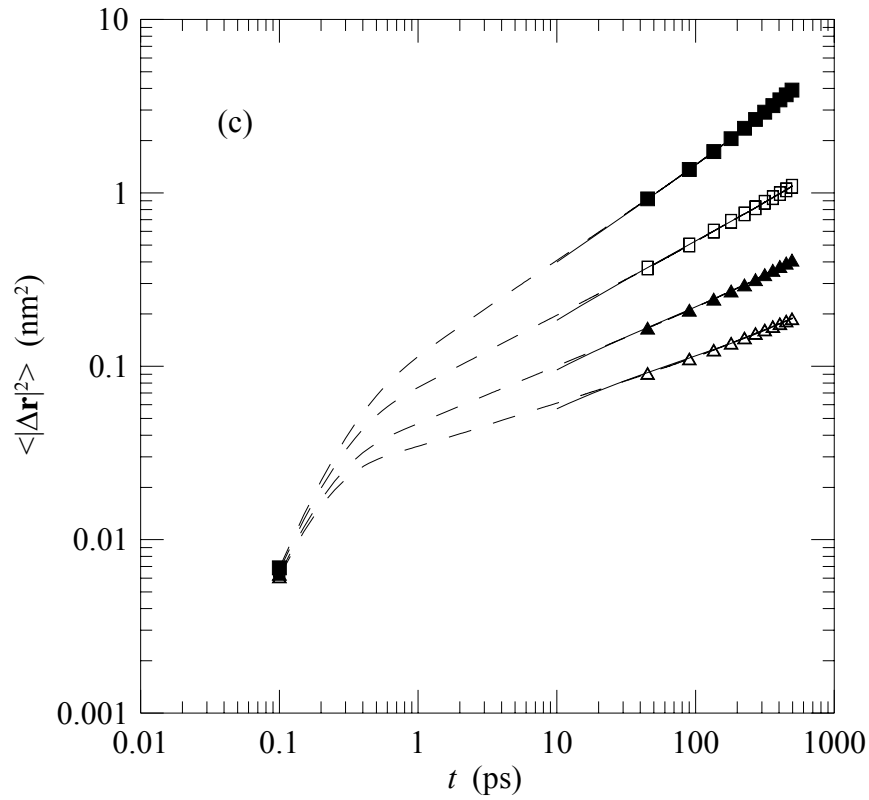


Figure 4.11(c). As in Figure 4.11 (a,b) but for 873K.

(a) In the analysis of the Helium MSD results it was very soon clear that the first term in Equation (4.9) was only of marginal importance and Helium mobility is essentially Fickian for most of the sampled time range. In most cases it was observed that the cluster length scale ℓ fluctuated considerably over the range 0.3-4 nm as anticipated in view of the small kinetic diameter of the Helium particle. The fit to the Helium data was therefore limited to the second term on the right of Equation (4.9) and the fitted diffusivities, D , as obtained from the slopes of the dashed lines shown in Figure 4.10 are reported in Table 4.4 and Figure 4.14.

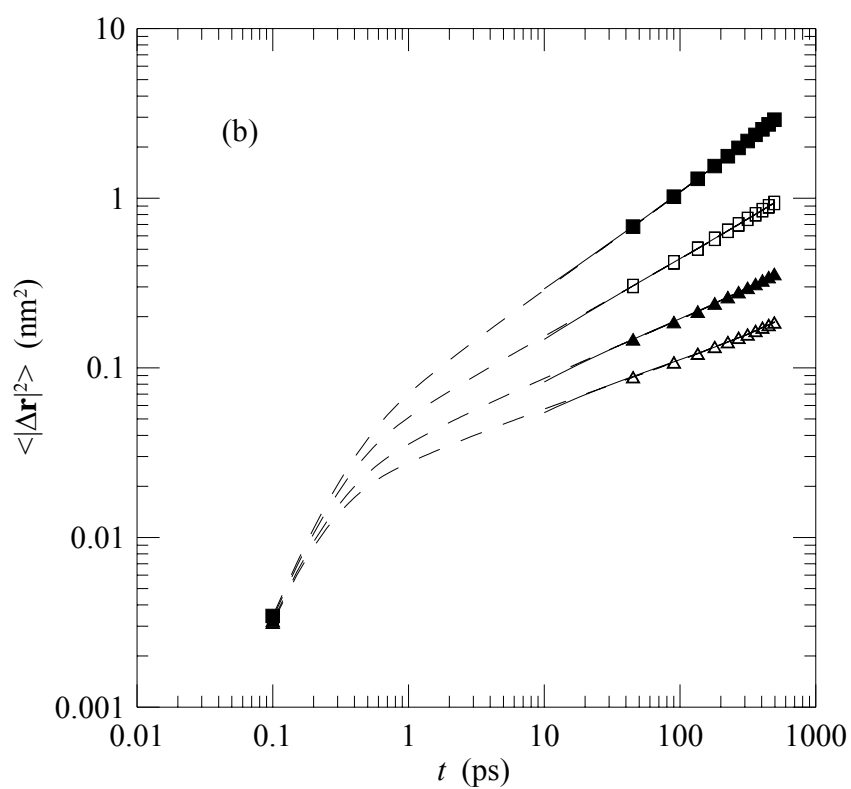
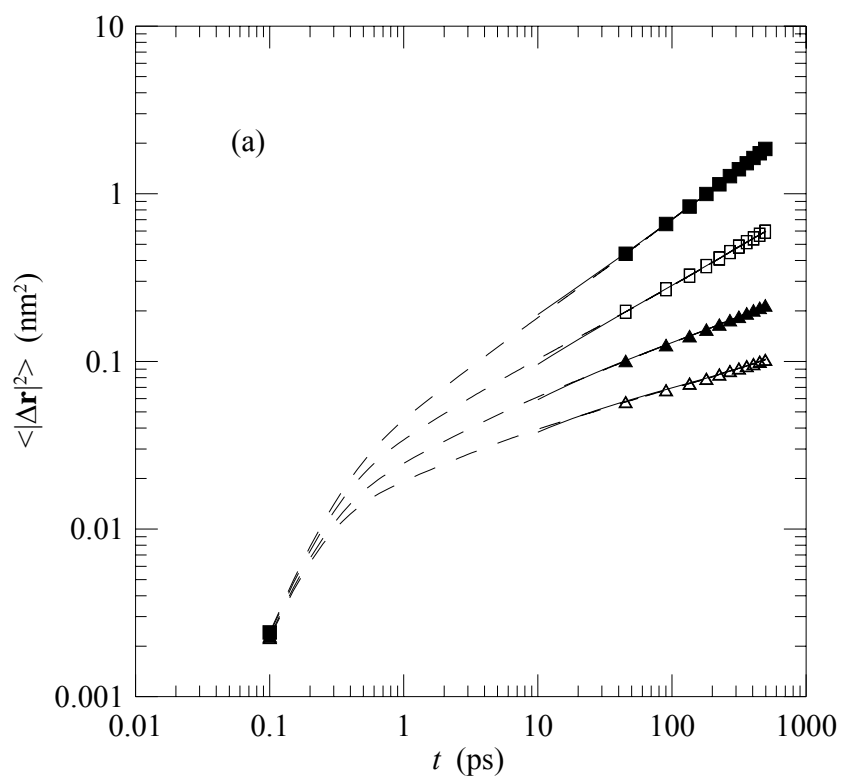


Figure 4.12(a, b). The mean square displacement of CO₂ molecules within moderate-to-high density nanoporous silica media at 473K (a) and 673 (b). ■ 1.73 g/cc; □ 1.86 g/cc; ▲ 1.97 g/cc; △ 2.03 g/cc.

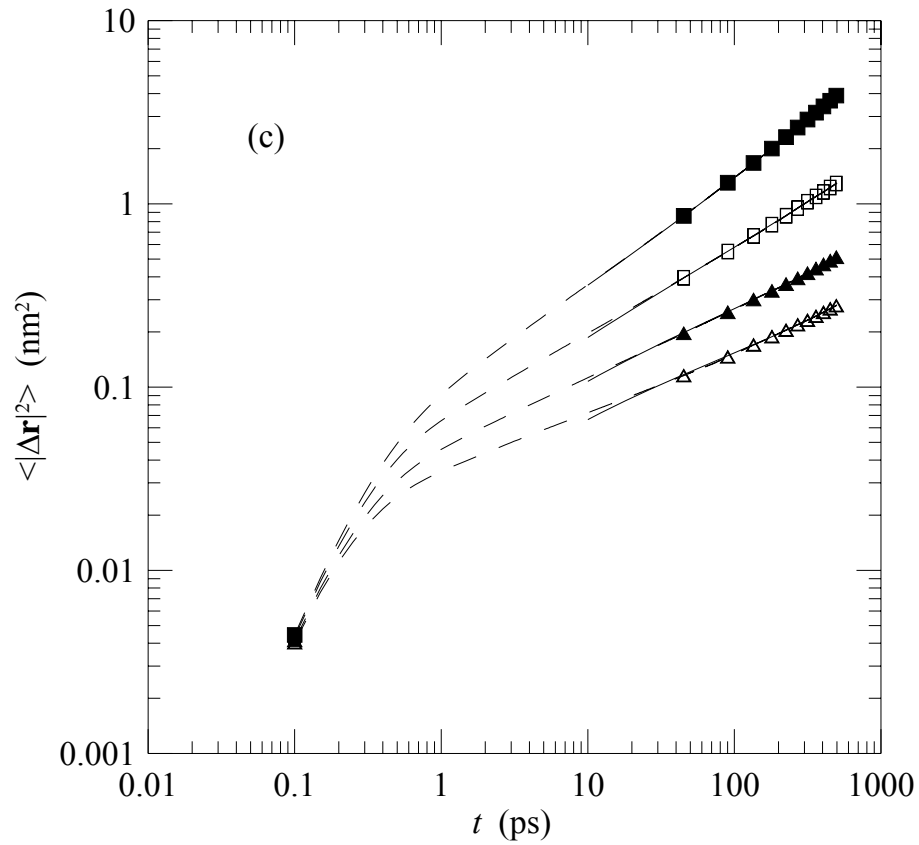


Figure 4.12(c). As in Figure 4.12 (a,b) but for 873K.

```

model = (a* t^n)/(1 + b *t^n) + c*t

cons0 = {0.0 < n < 1.0, a > 0.0, b > 0.0, 0.0 < c < 0.5};

paramsinit = {{a, 0.001}, {b, 0.001}, {c, 0.0001}, {n, 0.5}}

nlm = NonlinearModelFit[data, {model, cons0}, paramsinit, t, Method ->
"NMinimize"];

```

Figure 4.13 Code for implementation of the nonlinear regression algorithm in Mathematica.

(b) The fractal dimension d_w is known to be bounded by $3.667 < d_w < 3.863$ for three dimensional Euclidean systems (Bunde and Havlin (1991)). From the full four parameter regression on the N_2 and CO_2 data this parameter was estimated, on average, to be $d_w \sim 3.98 \pm 0.8$ which is within the bounds of the values reported by Bunde and Havlin. On this basis and in view of the scatter observed in the full nonlinear analysis it was deemed best to fix the value of d_w at 3.765. The results reported in Table 4.4 are based on this assumption with the three coefficients A , ℓ and D in Equation (4.9) now serving as the regression parameters for the fit to all of the MSD data for both N_2 and CO_2 .

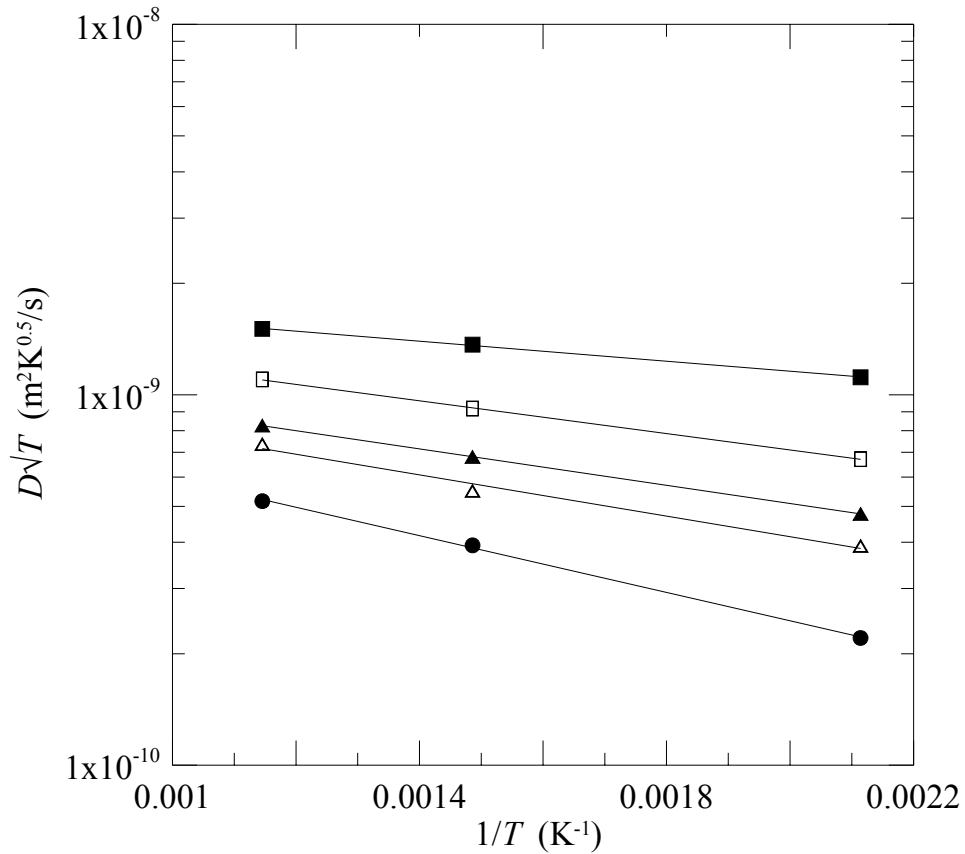


Figure 4.14 The diffusivity of Helium as a function of temperature within silica nanoporous structures at densities of ■ 1.73 g/cc; □ 1.86 g/cc; ▲ 1.97 g/cc; △ 2.03 g/cc; ● 2.2 g/cc.

Table 4.4 MSD Nonlinear fitting parameter estimates. The standard errors on these parameters were determined to be less than $\pm 20\%$ in all cases based on averages over five bins of five configurations each.

Gas	Density (g/cc)	T (K)	A	ℓ (nm)	D (m ² /s) (x 10 ¹¹)
He	1.73	473	-	-	2.426x10 ³
		673	-	-	3.542x10 ³
		873	-	-	4.450 x10 ³
	1.86	473	-	-	1.458 x10 ³
		673	-	-	2.383 x10 ³
		873	-	-	3.251 x10 ³
	1.97	473	-	-	1.038 x10 ³
		673	-	-	1.763 x10 ³
		873	-	-	2.441x10 ³
	2.03	473	-	-	0.850 x10 ³
		673	-	-	1.428 x10 ³
		873	-	-	2.176 x10 ³
	2.2	473	-	-	0.480 x10 ³
		673	-	-	1.018 x10 ³
		873	-	-	1.525 x10 ³
CO ₂	1.73	473	0.0533	2.123	15.90
		673	0.0814	1.739	30.85
		873	0.0979	1.946	50.73
	1.86	473	0.0305	0.367	6.289
		673	0.0464	0.459	10.37
		873	0.0577	0.546	15.35
	1.97	473	0.0237	0.184	2.094
		673	0.0315	0.228	4.360
		873	0.0391	0.278	6.378
	2.03	473	0.0184	0.124	0.851
		673	0.0237	0.161	2.051
		873	0.0258	0.200	3.403
N ₂	1.73	473	0.0653	0.868	16.03
		673	0.0968	0.909	35.70
		873	0.1130	0.930	66.92
	1.86	473	0.0376	0.301	5.059
		673	0.0494	0.386	6.877
		873	0.0599	0.465	12.44
	1.97	473	0.0225	0.163	1.818
		673	0.0308	0.207	3.119
		873	0.0375	0.233	5.547
	2.03	473	0.0197	0.113	0.800
		673	0.0232	0.137	1.674
		873	0.0251	0.162	2.077

The diffusivities for Helium reported in Table 4.4 are plotted in Figure 4.14 in the form D/\sqrt{T} . At all densities the diffusivity displays activated behaviour, albeit comparatively weak at the lower densities. At 2.2 g/cc where, as expected, the activated process is most evident, the activation energy is 7.34 kJ/mol. This value is lower than expected. Altemose (1961) has reported the diffusivity for Helium in fused silica to be $D_{He} \sim 10^{-6} \exp(-E_{A,He} / RT)$ (m²/s) with the activation energy $E_{A,He} = 33.3$ kJ/mol. Taking into consideration the \sqrt{T} term in Figure 4.14 the Helium activation energy for the model system investigated in this work is still low (9.93 kJ/mol) by approximately a factor of three. This discrepancy is believed to be due to the rather small value for the Lennard-Jones σ -value for Helium which is the recommended value proposed by Chakravarty (1997). At this time this issue is set aside for future consideration but should be borne in mind when ultimately addressing a direct comparison between membrane permeation rates and permselectivities for Helium relative to other gas species.

The primary focus of this work is demonstrated by the comparison of the model results (Equation (4.9)) for both N₂ and CO₂ in Figures 4.11 and 4.12. In all cases the quality of the fit is excellent and the deconvolution of the anomalous and Fickian terms, as shown for example for CO₂ in Figure 4.15 under two extreme conditions, demonstrates that both terms are of similar magnitude over much of the sampling time.

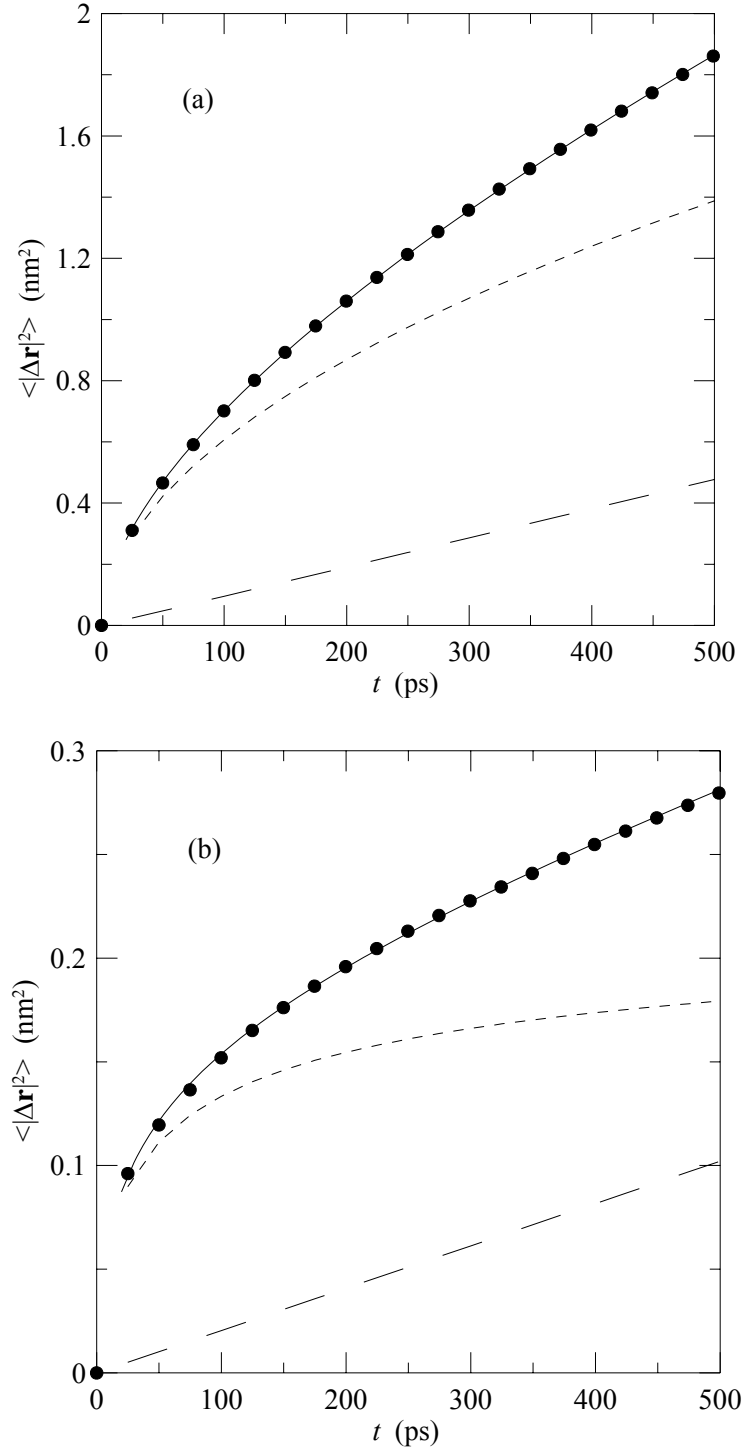


Figure 4.15 Examples of the deconvolution of the MSD based on Equation (4.9) for CO_2 at (a) $T = 473\text{K}$ and $\rho_{\text{SiO}_2} = 1.73\text{ g/cc}$ and (b) $T = 873\text{K}$ and $\rho_{\text{SiO}_2} = 2.03\text{ g/cc}$. The long dash is the Fickian contribution, the short dash is the anomalous term (the first on the right of Equation (4.9)) and the solid line is the combination of both these terms. The filled circles are original MD data.

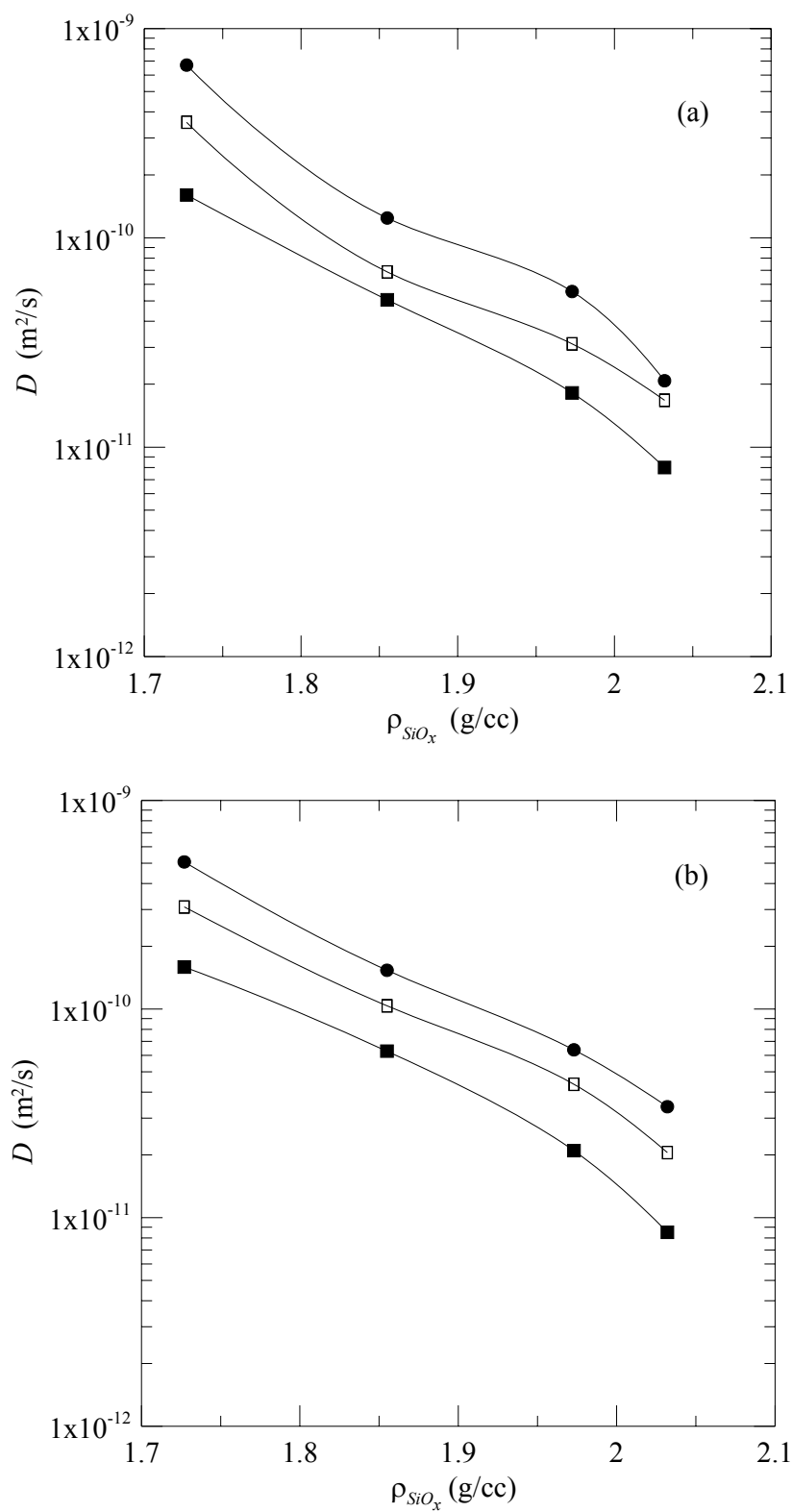


Figure 4.16 The Fickian diffusivity as a function of density ■ 473K; □ 673K; • 873K. (a) N_2 and (b) CO_2 .

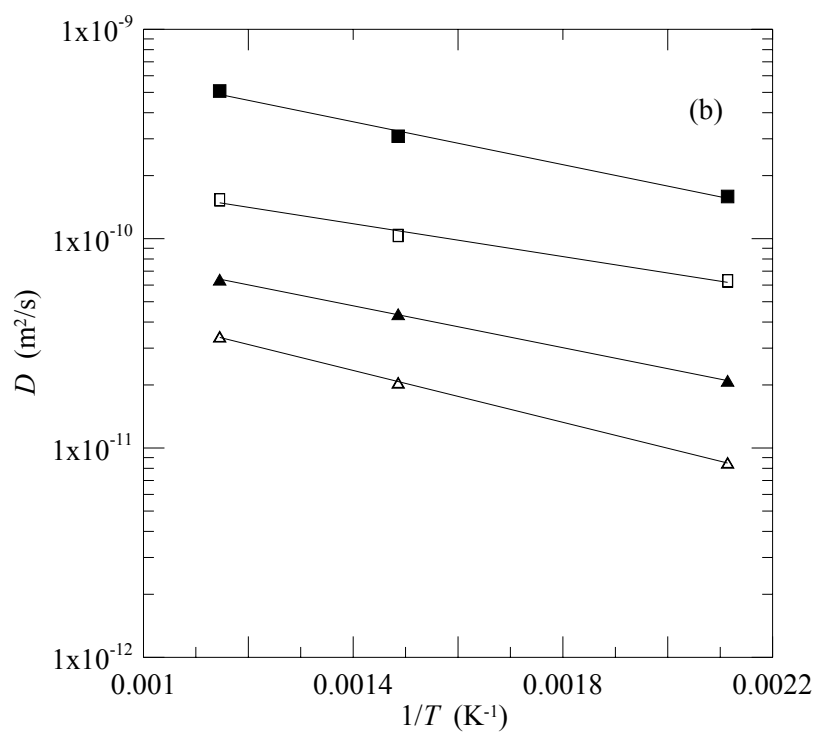
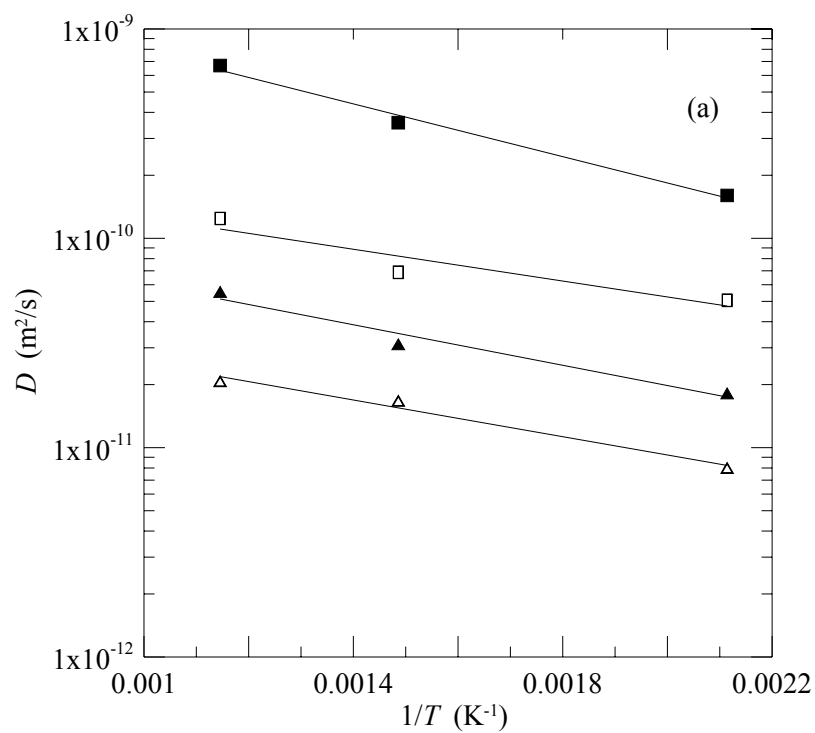


Figure 4.17 The Fickian diffusivity as a function of temperature: ■ 1.73 g/cc; □ 1.86 g/cc; ▲ 1.97 g/cc; △ 2.03 g/cc. (a) N₂ and (b) CO₂.

The diffusivities for N₂ and CO₂ reported in Table 4.4 are plotted as functions of density and temperature in Figures 4.16 and 4.17 respectively. At all temperatures D would appear to drop rapidly as the density increases above 2.0 g/cc indicating significant confinement effects in the quasi-static silica medium. At 873K, the highest temperature investigated here and hence that temperature at which one would anticipate least resistance to diffusion due to intrinsic vibrations in the silica structure, results reported by Kajihara et al (2007) for N₂ in amorphous silica provide $D \sim 6.6 \times 10^{-16} \text{ m}^2/\text{s}$ which is four orders of magnitude smaller than the lower bound of Figure 4.16(a). This suggests that as the density increases towards 2.2 g/cc the trend lines indicated in the Figure 4.16 are indeed correct with a very sharp drop in diffusivity in all cases as the density approaches 2.2 g/cc.

This may also be inferred from the temperature dependence indicated in Figure 4.17. At low densities the activation energies for diffusion are comparatively high reflecting a behaviour that might be more akin to diffusion in relatively ‘wide’ pores (see Table 4.1) with hopping between surface sites. At the highest density however the gas molecules are tightly confined and the diffusion depends much more on the intramolecular dynamics of the silica tetrahedra and their vibrations relative to neighbouring tetrahedra. The rather weak dependence of ℓ on temperature in contrast to the significant density dependence of this parameter (see Table 4.4 and Figure 4.18) would suggest that at densities higher than those investigated here the cavities within which N₂ or CO₂ molecules are trapped are very tight with cluster pathways for wormlike movement of the N₂ and CO₂ molecules rapidly approaching the cavity size itself (compare the pore radii

reported in Table 4.1 with the percolation cluster sizes in Table 4.4). Transport under these conditions would involve diffusive jumps of the gas particles determined by rare events resulting from the formation of apertures between trapping sites in the solid. The formation of apertures sufficiently wide for transport to take place would require the transformation of significant levels of thermal energy into potential energy and it is anticipated that the slopes of the lines shown in Figure 4.17 would increase significantly as the density approaches 2.2 g/cc.

The density dependence of the percolation cluster size, ℓ , as shown in Figure 4.18(a) is also of particular interest when compared with the earlier results for static media as cited in Figure 4.3 (Cuffe et al (2006)). As was observed for static media there is a distinct discontinuity in the semi-logarithmic plot which is believed to be a signature of the percolation transition for the superconducting channels depicted in Figure 4.9(a). As the ‘superconducting’ channels become fully percolating, the percolation cluster size, ℓ , extends to infinity. For the fully mobile structures examined here the influence of the growth in the percolation length scales for CO₂ is clearly observed in the range 79% - 84% of the density of bulk silica in contrast to the much lower density of 56% of the bulk value for the static systems shown in Figure 4.3. For N₂ the percolation transition occurs below 80% in the present case in comparison with the upper limit of 52% for the static structures. For reasons to be outlined in Chapter 6 it is believed that these values of the effective percolation transitions for silica observed in this work are in fact lower bounds and that silica membranes fabricated via CVD or sol-gel synthesis

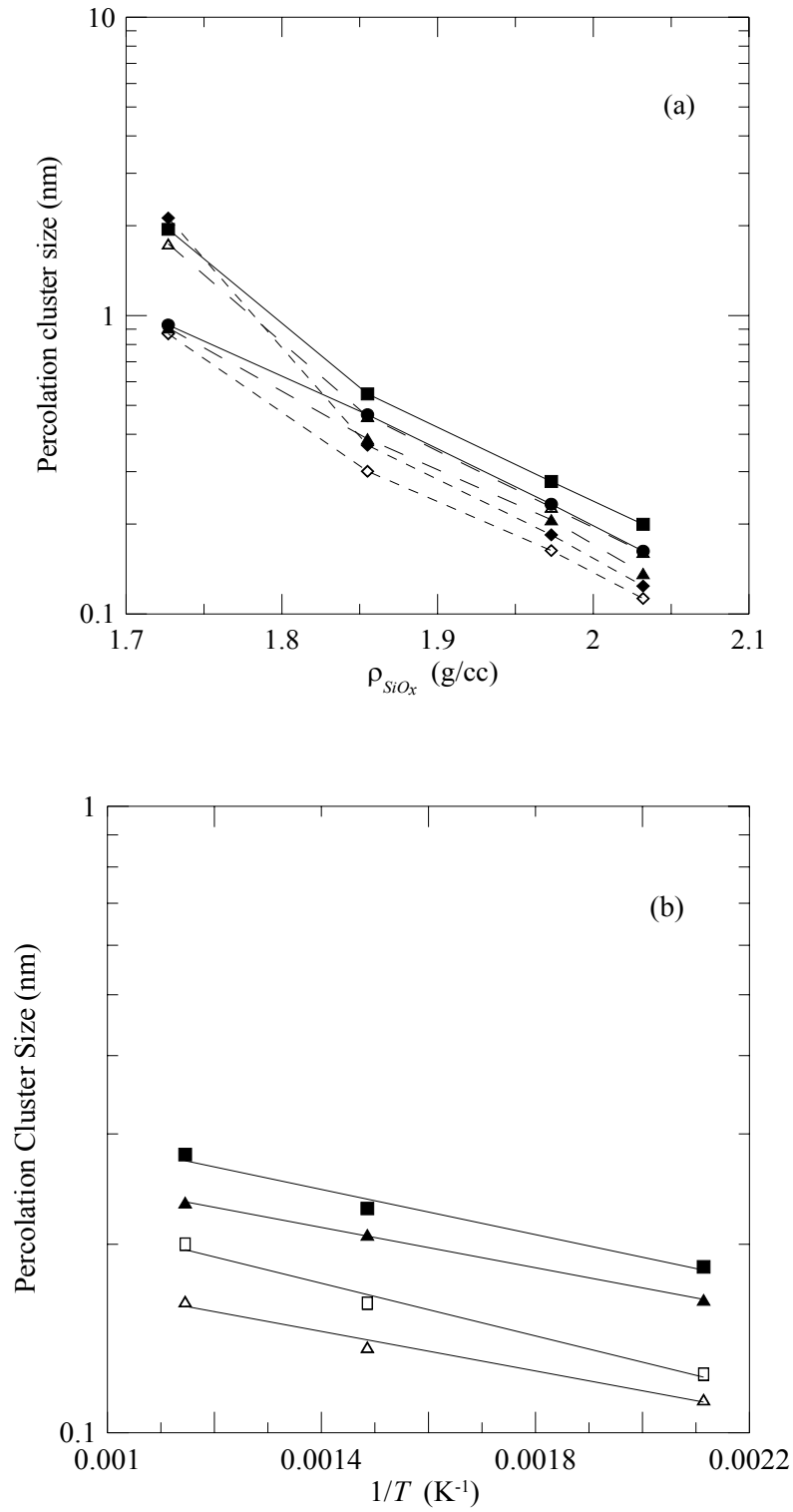


Figure 4.18 (a) The percolation cluster size, ℓ , as a function of density: ■ CO₂ and • N₂ at 873K; △ CO₂ and ▲ N₂ at 673K; ◆ CO₂ and ◇ N₂ at 473K. (b) The percolation cluster size as a function of temperature: ■ CO₂ and ▲ N₂ for 1.97 g/cc; □ CO₂ and △ N₂ for 2.03 g/cc.

will have superconducting channel percolation transitions for the individual gas species closer to the bulk glass density than the results inferred from Figure 4.18(a).

In the next Chapter an approach is developed to model the fabrication of thin solid films of the kind illustrated in Figure 4.1 and it will be shown that the densities of the films created during chemical vapour deposition are close to the density, 2.2 g/cc, of amorphous vitreous silica. In this work, while MD simulations at this density are not performed for the gases N₂ and CO₂ in view of the very low values for D in both cases as implied by correlations reported in the literature (Kajihara et al (2007) for N₂ and Behrens (2010) for CO₂) an approximate analysis will be given which provides supporting theoretical evidence for the significant selectivities observed experimentally by Cuffe et al (2006) and McCann (2010).

Chapter 5. Kinetic Monte Carlo Simulation of the Formation of Thin Solid Films of Silica via Chemical Vapour Deposition: Methodology

A key outcome from the results reported in Chapter 4 is the need to ensure reliable characterisation of the silica media involved in membrane separations processes in order to define the conditions for optimum separation of gas mixtures. It is therefore imperative that computational tools be developed to permit the simulation of the fabrication of nano-membranes at the nanoscale. In this chapter the methodology employed in the fabrication of thin nanoporous amorphous silica films via chemical vapour deposition (CVD) is described as a first step in the realisation of this goal. The CVD process simulated involves nonporous silica substrates onto which reactive precursors are deposited. While the ultimate objective is to develop methods appropriate to deposition onto porous substrates, nonporous substrates are chosen in this work to simplify the interpretation of the resultant morphology of the silica films formed and to validate the molecular simulation methods employed. These computational techniques involve a combination of lattice kinetic Monte Carlo (KMC) and off-lattice Monte Carlo to investigate the growth process using the CVD deposition technique.

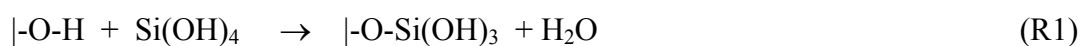
5.1 The Substrate Material

In this work both silicic acid, Si(OH)_4 , and independently, tetraethoxysilane, $\text{Si(OCH}_2\text{CH}_3)_4$ (TEOS), are employed as the deposition precursors involved in the reaction-controlled growth of silica (SiO_x) layers on the surface of a nonporous amorphous silica substrate at temperatures below 1000K.

The silica substrate is an atomistic model of amorphous glass at a bulk density of 2.2g/cc initially prepared by a combination of methods similar to those reported by Wooten et al (1985) and MacElroy and Raghavan (1990). A section of a three-dimensional periodically imaged bulk amorphous silica (SiO₂) cube is cut along the *xy*-plane at two *z* locations to produce a substrate base material on the upper side (+*z* direction) of which the deposition would take place. While sectioning, the bridging oxygen atoms connected to the two silicon atoms which share both top and bottom plane of the substrate were converted into hydroxyl groups (OH) and each of the two silicon atoms is assigned to one OH group. Finally, a structure with dimensions 3.56643nm x 3.56643nm x 1.5nm is generated and serves as the substrate for silica deposition. The periodic boundary condition along the *z* axis is then removed and the OH groups on the top surface are treated as the initial reacting sites to commence the growth of the SiO_x layer. The bottom part of the substrate (1.0 nm) is kept rigid and the top 0.5 nm is taken into account for Monte Carlo moves during atomic relaxation in the thin film deposition process. The film growth takes place along the +*z* direction of the substrate and periodic boundary conditions are applied in the *x* and *y* directions in order to minimise edge effects. Figure 5.1 shows the initial SiO₂ structure and the front view of the cleaved surface employed as the substrate in this study.

5.2 Reaction Kinetics

The reactions which are deemed to take place in this model system are as follows. In the case of silicic acid, Si(OH)₄, the deposition occurs as (Pelmenschikov et al (2001))



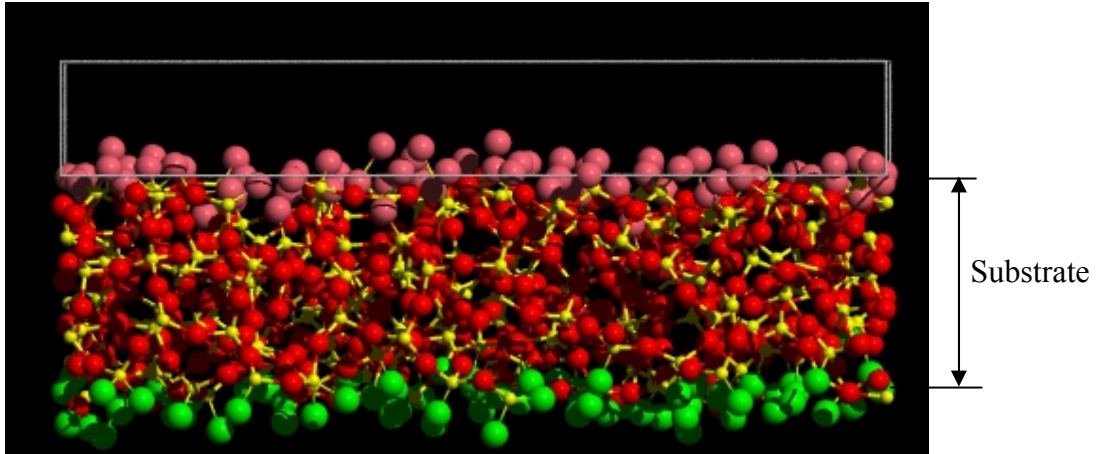


Figure 5.1: A snapshot of the initial amorphous 3.56643nm x 3.56643nm x 1.5nm substrate used for deposition in this model. The green atoms represent the bottom surface and the pink atoms correspond to the top surface hydroxyl groups which serve as reactive seed sites for the deposition process.

In the simulation of the deposition of TEOS the nine irreversible reactions listed in Table 5.1 are considered to take place (Coltrin et al (2000)). Furthermore, in both the $\text{Si}(\text{OH})_4$ and TEOS deposition studies the surface condensation (annihilation) reaction



also takes place.

For simplicity in all of the simulations conducted here only reactions which may be considered to be taking place on the solid surface or within the growing

film have been simulated and gas phase decomposition/dissociation of the TEOS has been neglected. Furthermore, the rate for each of the reactions is defined by,

$$r_{if} = k_{if} c_{Xi} c_{Yi} \quad (i = R1, R2, R11)$$

or

$$r_{if} = k_{if} c_{Xi} \quad (i = R3 - R10) \quad (5.1)$$

where k_{if} is the forward reaction rate constant for the reaction of species X and Y . The reverse reactions, which are of course all thermodynamically feasible, are omitted in these studies. This is based largely on an analysis of the reverse reactions for TEOS using thermochemical data summarized by Coltrin et al (2000) for the temperature range of interest in the present work (473-873K). Each of the reactions listed in Table 5.1 are essentially irreversible under these conditions. The approach employed here therefore serves as a model of low pressure chemical vapour deposition (LPCVD) reactors with a small though finite gas phase volume and a high surface area solid substrate and is also representative of the conditions employed in low temperature molecular beam deposition studies.

To calculate the rate constants an Arrhenius type relation is considered in this study

$$k_{if} = A_{if} \exp\left(-\frac{E_{if}}{RT}\right) \quad (5.2)$$

where E_{if} is the energy barrier between two states (with the subscript, if , denoting the forward transition of reaction i), R is the universal gas constant, T is the temperature and A_{if} is the pre-exponential (frequency) factor.

The Arrhenius parameters, in appropriate units, for the reactions R1- R10 are provided in Table 5.2. For reaction R1, with forward rate constant k_{1f} , the parameters are based on activation energy estimates reported by Pelmenchikov et al (2001) and Pereira et al (1998) and estimates for the frequency factors of bimolecular surface reactions cited by Zhdanov (1991).

The Arrhenius parameters for reactions R3 – R10 in Table 5.2 are taken directly from earlier work reported by Coltrin et al (2000). The activation energy for reaction R2 refers to a net contribution associated with both adsorption of TEOS onto the silica film followed by reaction within the layer. In the studies reported here, the rate expression employed for this process is

$$\begin{aligned}
 r(\mathbf{r}) &= k_{2f} c_{OH}(\mathbf{r}) c_{TEOS}(\mathbf{r}) \\
 &= \frac{k_{2f}}{RT} < K_{TEOS}(\mathbf{r}) > c_{OH}(\mathbf{r}) p_{TEOS}
 \end{aligned}
 \tag{R2}$$

Pre-production kinetic Monte Carlo simulations (details of the KMC methodology employed are provided in Section 5.3 below) were conducted to ascertain initial estimates for the equilibrium values of the TEOS partition coefficients, $< K_{TEOS}(\mathbf{r}) >$, and the silanol group loadings as functions of position, \mathbf{r} , within the film over the temperature range 473-873K. The results of these computations for the group $< K_{TEOS}(\mathbf{r}) > c_{OH}(\mathbf{r})$ average over simulated layers at three TEOS deposition pressures (0.000284, 0.00284, and 0.0284 torr) are reported in Figure 5.2 as a function of temperature. Note that these simulations demonstrated that the deposition reactions actually only take place within a very thin gas-solid interfacial region (2-3 nm thick) at the surface of the evolving film.

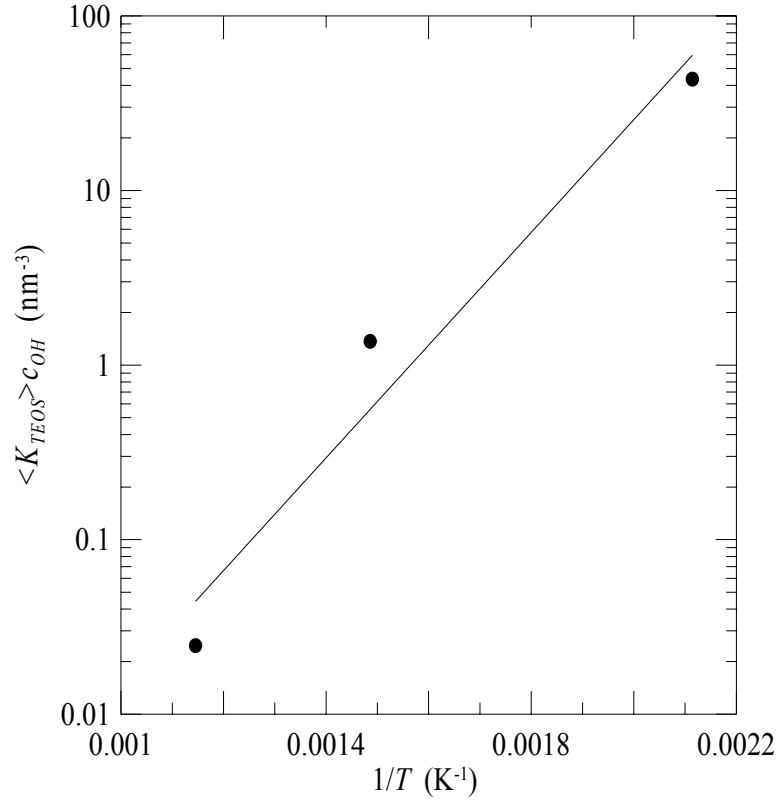


Figure 5.2. The layer-averaged equilibrium adsorption/reaction term required for evaluation of rate coefficient for TEOS deposition.

The fit provides the averaged result

$$\langle K_{TEOS} \rangle c_{OH} = 8.84 \times 10^{-6} \exp\left(\frac{61,500(\text{J/mol})}{RT}\right) \quad (5.3)$$

The next step employed the cold molecular beam data reported by Coltrin et al (2000). Their data provide the growth rate at 1.7×10^{-3} torr as a function of temperature

$$\text{Growth rate} = 5.19 \times 10^{-3} \exp\left(-\frac{187500}{RT}\right) \text{ (Å/min)} \quad (5.4)$$

Reaction No.	Reactions
	A. Deposition Reaction
R2	$\text{Si}(\text{O}-\text{CH}_2\text{CH}_3)_4 + -\text{OH} \rightarrow -\text{O}-\text{Si}(\text{O}-\text{CH}_2\text{CH}_3)_3 + \text{C}_2\text{H}_5\text{OH}$
	B. Dissociation Reactions
R3	$-\text{Si}(\text{O}-\text{CH}_2\text{CH}_3)_3 \rightarrow -\text{Si}(\text{OH})(\text{O}-\text{CH}_2\text{CH}_3)_2 + \text{C}_2\text{H}_4$
R4	$-\text{Si}(\text{OH})(\text{O}-\text{CH}_2\text{CH}_3)_2 \rightarrow -\text{Si}(\text{OH})_2(\text{O}-\text{CH}_2\text{CH}_3) + \text{C}_2\text{H}_4$
R5	$-\text{Si}(\text{O}-\text{CH}_2\text{CH}_3) \rightarrow \equiv\text{Si}(\text{OH}) + \text{C}_2\text{H}_4$
R6	$-\text{Si}(\text{O}-\text{CH}_2\text{CH}_3)_2 \rightarrow =\text{Si}(\text{OH})(\text{O}-\text{CH}_2\text{CH}_3) + \text{C}_2\text{H}_4$
R7	$-\text{Si}(\text{OH})(\text{O}-\text{CH}_2\text{CH}_3) \rightarrow =\text{Si}(\text{OH})_2 + \text{C}_2\text{H}_4$
	C. Dissociation Reactions in presence of a siloxane bond (SiO_2)
R8	$-\text{Si}(\text{OH})(\text{O}-\text{CH}_2\text{CH}_3)_2 \rightarrow \equiv\text{Si}(\text{O}-\text{CH}_2\text{CH}_3) + \text{C}_2\text{H}_5\text{OH}$
R9	$-\text{Si}(\text{OH})_2(\text{O}-\text{CH}_2\text{CH}_3) \rightarrow \equiv\text{Si}(\text{O}-\text{CH}_2\text{CH}_3) + \text{H}_2\text{O}$
R10	$-\text{Si}(\text{OH})_2(\text{O}-\text{CH}_2\text{CH}_3) \rightarrow \equiv\text{Si}(\text{OH}) + \text{C}_2\text{H}_5\text{OH}$

Table 5.1 Chemical Reactions for SiO_2 deposition from TEOS

Reaction No.	Frequency Factor	Activation Energy (kJ/mol)
R1	$3.45 \times 10^{15} \text{ (cc.mol}^{-1}\text{sec}^{-1}\text{)}$	110
R2	$1.70 \times 10^{20} \text{ (cc.mol}^{-1}\text{sec}^{-1}\text{)}$	249
R3	$5.1 \times 10^{12} \text{ (sec}^{-1}\text{)}$	197
R4	$3.4 \times 10^{12} \text{ (sec}^{-1}\text{)}$	197
R5	$1.7 \times 10^{12} \text{ (sec}^{-1}\text{)}$	197
R6	$1.7 \times 10^{12} \text{ (sec}^{-1}\text{)}$	197
R7	$1.7 \times 10^{12} \text{ (sec}^{-1}\text{)}$	197
R8	$2.0 \times 10^{12} \text{ (sec}^{-1}\text{)}$	184
R9	$2.0 \times 10^{12} \text{ (sec}^{-1}\text{)}$	184
R10	$2.0 \times 10^{12} \text{ (sec}^{-1}\text{)}$	184
R11	$10^{13} \text{ (sec}^{-1}\text{)}$	(See Eq. 3)

Table 5.2 Arrhenius Parameters for Si(OH)₄ and TEOS Deposition Reactions

Under these conditions the growth rate is determined primarily by reaction R2 and, from a combination of the exponential terms in Equations (5.3) and (5.4), the activation energy for the reaction rate constant k_{2f} is estimated to be 249 kJ/mol. The last step in the analysis requires an accurate estimate of the frequency factor for k_{2f} and this was obtained directly by comparing the growth rate in Equation (5.4) with extended KMC computations which will be reported later in Chapter 6.

It is important to note that there are two distinct differences in the manner in which the rate constant k_{2f} is treated in this work in contrast to Coltrin et al (2000). In the work reported by Coltrin et al the Arrhenius frequency factor for R2 is cited in terms of a reactive sticking coefficient based on surface area; the frequency factor reported in Table 5.2 is in units appropriate to a bulk second order reaction with the surface silanol groups distributed within the three dimensionally growing nanoporous silica film. The activation energy for the TEOS-silanol reaction is also significantly larger than the value reported in (Coltrin et al (2000)) (in the latter this value was cited as 183 kJ/mol). This is due to the separate and explicit evaluation of the equilibrium distribution coefficient $\langle K_{TEOS}(\mathbf{r}) \rangle$ as described above. Interestingly, the activation energy reported in Table 2 for the TEOS-silanol reaction is similar in magnitude to the activation energy for the homogeneous gas phase dissociation of TEOS to produce the intermediate $\text{Si}(\text{OH})(\text{OC}_2\text{H}_5)_3$. This could serve to demonstrate that reaction R2 as depicted in Table 2 and in the work of Coltrin et al (2000) is not elementary even though the overall reaction is second order as evidenced from a comparison with experimental observations. The intermediate $\text{Si}(\text{OH})(\text{OC}_2\text{H}_5)_3$ itself requires very little activation (see Coltrin et al (2000)) to complete the deposition reaction sequence with the surface silanol.

The forward reaction R11 (the self-healing reaction of Pelmenchikov et al. (2001)) is modelled based on reported observations of Bogillo et al (1997). The rate constant is expressed as

$$k_{11} = 10^{13} (\text{sec}^{-1}) \exp\left(-\frac{E_{A,11}}{RT}\right); E_{A,11} = 5.81 (\text{kJ/mol}) \exp(8.8164 r_{\text{Si-Si}} (\text{nm})) \quad (5.5)$$

where the distance scale is the relative separation of the two silicon atoms to which the condensing hydroxyls are attached (note that the estimate of the frequency factor, 10^{13} sec^{-1} , comes directly from Pelmenchikov et al (2001) and is in agreement with estimates reported by Zhdanov (1991) for monomolecular reactions in the adsorbed state). The reaction is considered to be pseudo first-order with the relative frequency computed for each individual pair of hydroxyls. Note that should the condensation reaction result in the formation of a 2-membered (diamond like) ring as shown in Figure 5.3, then the reaction is not allowed to proceed. The reverse reaction is considered to occur rapidly (an example of the self-healing process outlined by Pelmenchikov et al (2001)) thereby eliminating the highly strained configuration indicated by the diamond-like configuration on the right hand side of Figure 5.3.

In section 5.3 below the kinetic Monte Carlo method employed in the execution of the formation of the thin silica films based on (a) reactions R1 and R11 for silicic acid deposition and (b) reactions R2-R11 for TEOS deposition is described in detail.

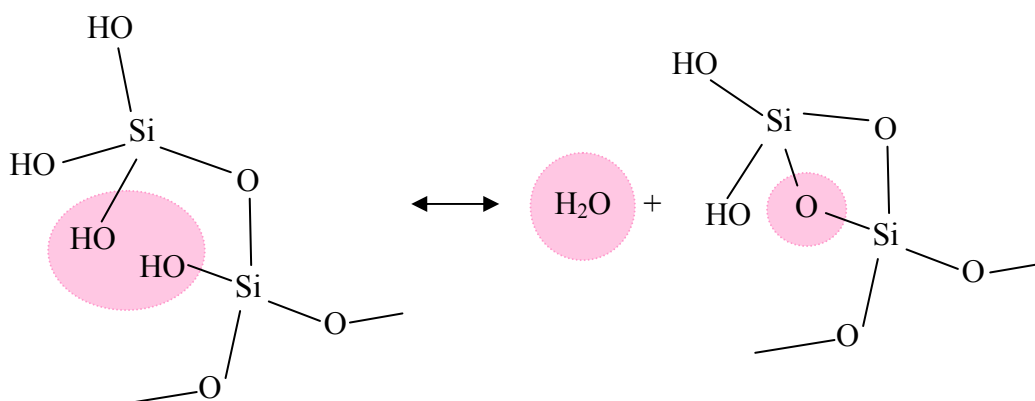


Figure 5.3: The hypothetical formation of a strained two-membered oxygen ring during silanol condensation.

5.3 The Kinetic Monte Carlo Algorithm

5.3.1 The Reaction Frequencies and Reagent Partitioning

The evolution of the silica (SiO_x) film is simulated using the Bortz-Kalos-Lebowitz (1975) lattice kinetic Monte Carlo (KMC) method in conjunction with a hybrid off-lattice relaxation process. In the KMC process the reactive deposition precursor (silicic acid or TEOS) from the vapour phase is incorporated within the growing solid film and transformed into surface sites. The simulation space is discretized into small subcells each of dimension $0.5095 \text{ nm} \times 0.5095 \text{ nm} \times 0.5 \text{ nm}$ ($=\Delta V$) (see Figure 5.4). During the growth process, each subcell of the three dimensional simulation box can be occupied by one or more silicon sites which are bonded to a combination of molecular groups ($-\text{OH}$, $-\text{OCH}_2\text{OCH}_3$ or bridging oxygens) and the occurrence of one of the reactions at one of the sites is termed an event. At each KMC step the frequency of each reaction event in each subcell is calculated and the choice of reaction event, r , to be undertaken is determined by the

probability P_r which is proportional to the frequency of the associated surface reaction relative to the sum of all such frequencies.

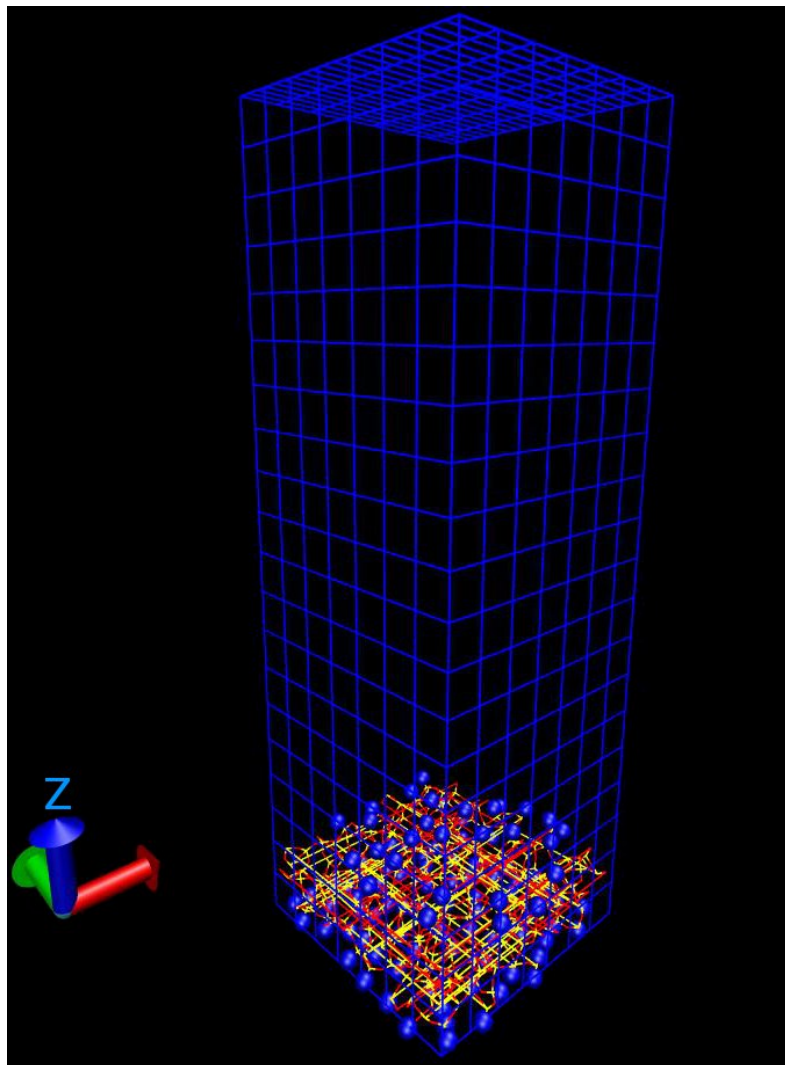


Figure 5.4 The grid of subcells employed in the KMC deposition algorithm.

The frequencies of the reactions are provided by the instantaneous conservation equation of the reacting species as defined locally in time and space by the expression

$$\frac{1}{V} \frac{dN_{Xi}}{dt} = -r_{if} = -k_{if} c_{Xi} c_{Yi} \quad (5.6)$$

where V is the volume of the space, N_X is number of species particles of type X and t is the time.

With a change in the number of reactant particles $\Delta N_{Xi} = -1$ of component X taking place during the time of a single reaction event then the above expression provides the frequency of this reaction, ν_{if} , as

$$\nu_{if} = \frac{1}{\Delta t} = V r_{if} \quad (5.7)$$

with, for example,

$$\nu_{if} = V k_{if} c_{Xi} c_{Yi}$$

representing the frequencies for the deposition reactions R1 or R2 where $c_{Xi} = c_{OH}$ and $c_{Yi} = c_{Si(OH)_4}$ or $c_{Si(OCH_2CH_3)_4}$ are the concentrations of OH (silanol), silicic acid and TEOS respectively.

In the present work the frequency for each reaction is scaled relative to the deposition reaction rate constant k_{1f} and expressed in the reference form

$$\nu_r^* = \frac{k_B T}{k_{1f}} \nu_r \quad (5.8)$$

Also noting that the (locally averaged) Henry's law reagent partition coefficient, $\langle K_R \rangle$, where $R = \text{Si(OH)}_4$ or TEOS, between the bulk gas and the nanopores of the evolving layer must be taken into consideration i.e.

$$c_R^{nanopore} = \langle K_R \rangle c_R^{Bulk} = \langle K_R \rangle \frac{p_R}{k_B T} \quad (5.9)$$

then the individual deposition reaction frequencies are given by

$$\nu_r^* = V c_{OH} \langle K_R \rangle p_R \quad (R = \text{Si(OH)}_4 \text{ or TEOS}) \quad (5.10)$$

To illustrate the application of the KMC algorithm, the procedure associated with the deposition of silicic acid as precursor is outlined below.

In the case of thin film formation via silicic acid deposition the two reactions of concern are R1 and R11. The selection of which reaction event should be sampled at any given time is determined by the frequencies of the reactions given by

$$\begin{aligned} \nu_1^*(\mathbf{r}) &= \Delta V R T c_{OH}(\mathbf{r}) c_{\text{Si(OH)}_4}(\mathbf{r}) \\ &= \langle K_{\text{Si(OH)}_4}(\mathbf{r}) \rangle N_{OH}(\mathbf{r}) p_{\text{Si(OH)}_4} \end{aligned} \quad (5.11)$$

$$\nu_{11}^*(\mathbf{r}) = R T \frac{k_{11}}{k_{1f}} N_{OH-HO}(\mathbf{r})$$

where $\nu_m^*(\mathbf{r})$ is the scaled frequency for reaction m and is directly related to the reaction frequency $\nu_m(\mathbf{r})$ (sec^{-1}) by

$$\nu_m^*(\mathbf{r}) = \frac{RT}{k_{1f}} \nu_m(\mathbf{r})$$

Furthermore, c_i is the local concentration of i , N_i is the number of sites of type i within volume element ΔV and p_i is the bulk vapour phase partial pressure of i . Note that the designation of the number of pairs of condensable silanol groups, N_{OH-HO} , is such that at least one of the OH groups is within the volume element ΔV and the second OH group is from a biased sample i.e. only those within a specific radius of the first group and also not a next-to-nearest bonded neighbour. Also in view of the inhomogeneity of the deposition process, the reaction frequencies are functions of position within the layer as it forms. The local partition coefficients for the reagents, $\langle K_i(\mathbf{r}) \rangle$, which are employed to determine the local concentration of these species relative to pre-specified bulk vapour pressures, are computed via a two step process involving a Widom insertion algorithm (for details see Allen and Tildesly (1987)) coupled with topological constraints associated with the accessibility of the nanocavities within the deposited layer to vapour/gas molecules exterior to the medium. As noted above, the deposition region is subdivided into small cubic elements of volume ΔV (0.125 nm^3) centred at \mathbf{r} and the partition coefficients are computed using

$$K_i(\mathbf{r}) = \frac{1}{\Delta V} \int_{\Delta V} \left\langle \exp \left(- \frac{U(\mathbf{r}', \mathbf{r})}{k_B T} \right) \right\rangle d\mathbf{r}' \quad (5.12)$$

where the energy $U(\mathbf{r})$ is computed from the potential interactions between the individual atoms of the inserted molecule ($\text{Si}(\text{OH})_4$ or TEOS) and the atoms of the silica layer. These individual atom-atom pair interactions include both Lennard-Jones $U_{LJ}(r_{ij})$ and Columbic $U_{el}(r_{ij})$ (partial charge) potential terms

$$U(r_{ij}) = U_{LJ}(r_{ij}) + U_{el}(r_{ij}) \quad (5.13)$$

The Lennard-Jones interaction has been described earlier in Chapter 4 and in contrast to the minimum image method employed in Chapter 4 for the Coulombic potential, in the deposition studies this potential in its screened form as proposed by Wolf et al (1999) is employed in this work to estimate the potential interactions between pairs of partial charges in the system. This is a computationally viable approach for large two dimensionally periodic disordered systems of the kind investigated in this work and, in its shifted force form (Fennel and Gezelter (2006)) the Wolf method involves the following modification to the Coulomb energy for $r_{ij} \leq R_c$:

$$U_{el}(r_{ij}) = \frac{q_i q_j}{4\pi\epsilon_0} \left(\frac{\text{erfc}(\alpha r_{ij})}{r_{ij}} - \frac{\text{erfc}(\alpha R_c)}{R_c} + \left\{ \frac{\text{erfc}(\alpha R_c)}{R_c^2} + \frac{2\alpha}{\sqrt{\pi}} \frac{\exp(-\alpha^2 R_c^2)}{R_c} \right\} (r - R_c) \right) \quad (5.14)$$

where r_{ij} is the distance between two partial atomic charges q_i and q_j on particles i and j respectively, and ϵ_0 is the electrical permittivity of space. The spherical cutoff R_c and shielding factor α must be determined empirically. When α is zero this expression reduces to a standard shifted force potential.

$$U_{el}(r_{ij}) = \frac{q_i q_j}{4\pi\epsilon_0} \left(\frac{1}{r_{ij}} - \frac{1}{R_c} + \left\{ \frac{1}{R_c^2} \right\} (r - R_c) \right) \quad (r_{ij} \leq R_c) \quad (5.15)$$

The parameters used in this work ($\alpha = 0$, $R_c = 1$ nm) are those suggested by Carré et al (2007) who have shown that the method can provide accurate results for amorphous silica systems.

In addition to the Lennard-Jones and electrostatic (partial charge) parameters provided in Table 4.2, the parameters for the ethoxy groups in TEOS are reported in Table 5.3. In this work the OH groups on the silicic acid, and the CH₂ and CH₃ groups in the case of TEOS deposition, are treated as united atom structures with the charge on the OH group defined by combining the individual charges on the oxygen and hydrogen atoms. In the TEOS simulations the charges on united atom structures CH₂ and CH₃ are assumed to be 0.0. To assign the charge on the surface silicon atoms q_{Si} during the growth process, the simple formula given by Equation (4.6) is extended to read

$$q_{Si} = -q_{OH} * (N_{OH}) - q_{O(Siloxane)} * (N_{O(Siloxane)}) - q_{O(Ethoxy)} * (N_{O(Ethoxy)}) \quad (5.16)$$

The angular bracket $\langle \rangle_{\Omega}$ in Equation (5.12) refers to the canonical average over orientations of the inserted species. The insertion cycle involves placing the test particle in question at a randomly selected position \mathbf{r}' with a random orientation within a subcell in the simulation box. Typically, the partition coefficients are evaluated by averaging over 10^3 trial cycles of insertion per subcell.

Atom	ε/k_B (K)	σ (nm)	Charge, $q_i(e_0)$
O(ethoxy)	185.0	0.2708	-0.64025
CH ₂	108.2	0.36	0.0
CH ₃	153.5	0.37	0.0

Table 5.3. Lennard-Jones and Coulombic partial charge parameters

5.3.2 Reagent Accessibility and Percolation

An additional refinement introduced into the simulations is an acknowledgement of the fact that the volume of the nanoporous silica medium cannot be fully accessible to the depositing species. This constraint is applied by sampling only those sites for deposition reactions to take place which are located on topologically permitted pathways within the growing nanoporous solid film. To this end a lower bound in the critical percolation threshold of 0.03 is selected for the Henry's Law constants in this work. Regions of the solid which are characterized by this value of K or lower are considered to be inaccessible. This lower bound corresponds to a conservative estimate based on the known percolation limit for partitioning in media composed of random assemblies of spheres (Kertesz (1981), Park and MacElroy (1989), Rintoul (2000) and Hofling et al (2006)) which nanoporous silica closely resembles (MacElroy (2002)). During the deposition process a percolation analysis is carried out to define the accessible path for the percolating reagent molecule through the porous structure. In this work, both lattice (Hoshen and Kopelman (1976)) and non-lattice (Al-Futaisi and Patzek (2003)) versions of the Hoshen and Kopelman (HK) algorithm (see Chapter 2) are employed to label percolation clusters within the solid film. The accessible cluster analysis employs a three dimensional cubic subcell lattice (grid) with periodic imaging in the x and y directions. Lattice HK is employed to explore accessible pathways through the entire deposited structure and, to establish the number of percolating clusters in the structure, the non-lattice form of the HK algorithm is implemented.

Although the reaction subcells form a regular 3D lattice this is easily handled by the non lattice extension of the Hoshen and Kopelman algorithm. It was decided to use the non-lattice version as it provides the most flexibility in specifying the regions to be connected and the connectivity rules.

To use the non-lattice version it is necessary to map the lattice connections to the connectivity table structures required by the non-lattice algorithm. This is achieved by scanning the 3D lattice and placing ‘atoms’ (nodes) in the accessible lattice cells and bonding them to neighbouring nodes, essentially converting the lattice representation to a pseudo molecular network. This was done while taking into account the periodic boundary conditions and rules for identifying neighbours considered below.

In order to validate the non-lattice algorithm a lattice version was also created and the lattice scanning part of this algorithm produces the connectivity structures required by the non-lattice algorithm. The original lattice algorithm was for a two dimensional rectangular lattice without periodic boundary conditions, and this was extended to allow two or three dimensional lattices with any dimension being periodic if required. The definition of what constitutes a neighboring cell is also flexible so that cells which share either faces, or edges, or corners could be selected as shown in Figure 5.5(a) below.

For the purpose of the accessible region cluster analysis the three dimensional cubic lattice is periodic in the x and y dimensions and each cell has up to 27 neighbors (those sharing a common face) with the exception of cells along the top

and bottom layers in the z direction. As the lattice is scanned each cell has 13 neighbours which have been previously examined (except on the first layer) as shown in Figure 5.5(b), by specifying which of these cells to examine one can easily allow all neighbors, only face sharing neighbours, or face and edge sharing neighbours. Furthermore, taking advantage of the generality of the non-lattice version of the algorithm one can use the values of the cell centered at the edge or corner positions as shown in Figures 5.5(c) and (d) to specify links between the node for the link and nodes version of the algorithm (note - this could be readily adapted to non-lattice partitions of the space such as Voronoi voids using bottlenecks as the links).

Having assigned cluster numbers to the reaction cells, the determination of the accessible cells is then trivial as all cells having the same cluster numbers found in the top layer are accessible from the top layer.

The percolation analysis is most readily described with reference to Figure 5.6. This figure illustrates a two dimensional representation of the system with each square representing one of the small volume elements (a cube of size $0.5095 \times 0.5095 \times 0.5 \text{ nm}^3$). The system of subcells is initially mapped to determine the subcell Henry's law coefficients. These are represented in varying shades of grey in Figure 5.6(a). The subcells are then segregated into two groups as indicated in Figure 5.6(b) and then the Hoshen-Kopelman cluster algorithm described above is employed to establish the set of percolating clusters within the structure. As indicated in Figure 5.6(c) there are 6 individual clusters marked with different colours (note that periodic boundary conditions are applied laterally).

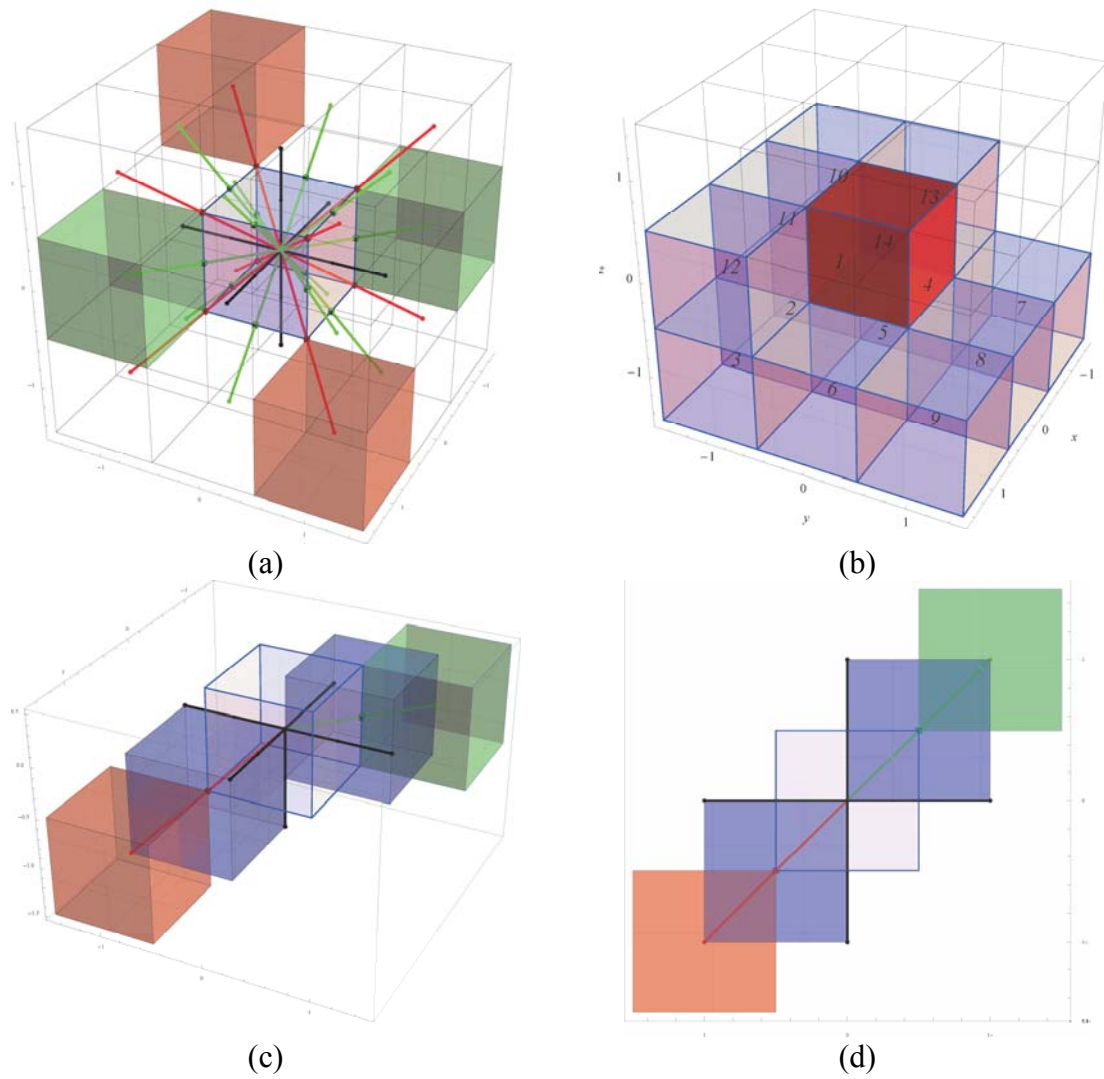


Figure 5.5. Cell connectivity on the 3D lattice. (a) A cell with its 27 neighbours is shown with two edge sharing neighbours and two corner sharing neighbours highlighted. The lines show the possible links between the cell nodes for the case where the full non-lattice version of the Hoshen-Kopelman algorithm is used. (b) The central cell (cell number 14) and its 13 previously examined neighbours. (c) A cell with one corner sharing neighbor (orange cell in bottom left hand corner) and one edge sharing neighbor shown (green cell in top right hand corner). The blue cells centered on the links between the central cell and these neighbours are the regions for determining whether these links are considered occupied or empty (blocked). (d) Top down view of (c)

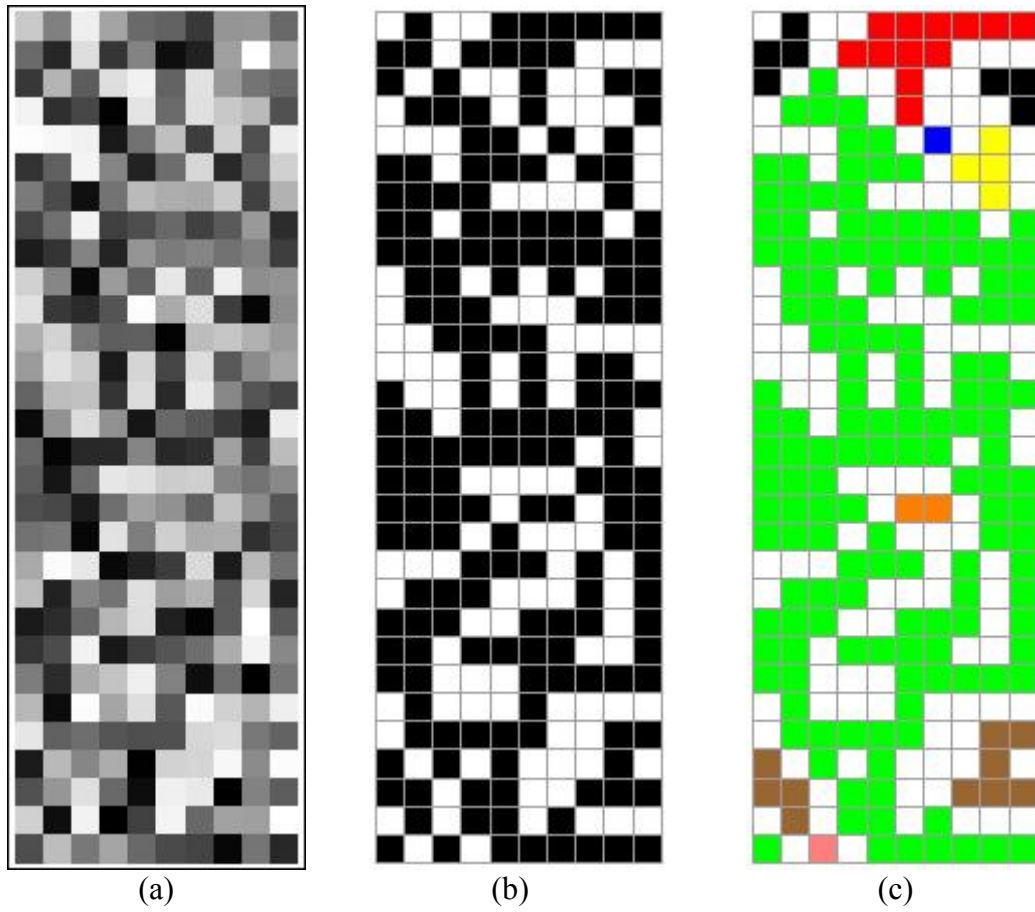


Figure 5.6. Two-dimensional example of the deposited layer (each layer divided into 0.5 nm squares). (a) An initial mapping of the relative magnitudes of the partition coefficients, (b) mapping of those subcells with $K < 0.03$ (white) and those with $K > 0.03$ (black), (c) cluster structure as determined by the Hoshen-Kopelman algorithm.

In general one may select the connectivity between clusters such as those shown in Figure 5.6(c) as appropriate to the given situation. In the studies reported in this work ‘coloured’ cells adjoining through edges and corners as well as faces are considered to be fully connected and hence the example shown in Figure 5.6 (c) is fully percolating from top to bottom.

5.3.3 The Bortz-Kalos-Lebowitz KMC Algorithm

A single cycle of the lattice KMC algorithm is completed with the selection of which reaction event to be undertaken. For the case of the silicic acid KMC simulations involving 2 reactions (see Equation (5.11) above) the probability of which reaction to execute is given by

$$P_{m,j} = \frac{v_{m,j}^*}{\sum_{i=1}^{N_{BIN}} \sum_{m=1}^2 v_{m,i}^*} \quad (5.17)$$

where N_{BIN} is the instantaneous number of subcells, each of volume ΔV , within the growing film at that given time. To implement this a random number uniformly distributed in the range (0, 1) is generated and the event (reaction i) to be undertaken is determined by

$$\sum_{j,m=1}^{i-1} \frac{v_{m,j}^*}{\sum_{k=1}^{N_{BIN}} \sum_{m=1}^2 v_{m,k}^*} < \xi_1 \leq \sum_{j,m=1}^i \frac{v_{m,j}^*}{\sum_{k=1}^{N_{BIN}} \sum_{m=1}^2 v_{m,k}^*} \quad (5.18)$$

Within this lattice KMC, one reaction is allowed to take place at one site in each KMC step. After an event has occurred, the simulation time is updated and the process is continued until the KMC cycle reaches a predefined number of events.

At each simulation step the time increment τ_{inc} is computed as

$$\tau_{incr} = -\frac{\ln(\xi_2)}{\sum_{k=1}^{N_{BIN}} \sum_{m=1}^2 v_{m,k}^*} \quad (5.19)$$

where ξ_2 is another random number uniformly distributed in the range (0, 1). The time increment as given by Equation (5.19) is adjusted dynamically and

stochastically to accommodate the fastest possible event at each simulation step. In the TEOS deposition studies the same approach was employed for the extended set of reactions R2-R11.

To minimize the energy and relax the structure independently of reactions R1-R11, the canonical Metropolis Monte Carlo scheme as outlined by Burlakov et al (2001) and Schumacher et al (2006a,b) has been employed at intervals between each KMC event. Initial studies to investigate the relative importance of the switching of pairs of siloxane bonds via the reversible bond switching reactions R12 and R13 (the Wooten, Winer, and Weaire formalism (1985))



confirmed that these reactions only occur extremely rarely at the temperatures investigated in this work (validating observations reported by Cabriolu and Ballone (2010)).

5.3.3 Structural Relaxation via Canonical Monte Carlo

In the canonical (Metropolis) MC simulations the energy is computed prior to and after the move using the Keating Si-O bond stretching and O-Si-O, Si-O-Si bond angle bending interaction potential (Keating (1966) and von Alfthan et al (2003)). The implementation of this potential for the Si-O pairs and O-Si-O, Si-O-Si triplets in the silica film is as described earlier in Chapter 4. The parameters of the Keating potential for the $\text{Si}(\text{OH})_4$ and $\text{Si}(\text{OCH}_2\text{CH}_3)_4$ deposition models used in this study are provided in Table 5.4. In the case of TEOS a reaction between the

depositing molecule and surface of the substrate results in carbon atoms being confined within the layer during the growth process. Mayo et al (1990) reported the parameters for organic molecules using the Dreiding force field which are employed in this work for prediction of the structure. The k_i^b and k_{ij}^θ values for the carbon atoms are obtained from the Dreiding potential and converted to correlate with the Keating potential. The bond stretch force constant k_i^b is taken to be the same as the corresponding coefficient $k_{ij}^{b(dreiding)}$ reported by Mayo et al (1990) and the value of k_{ij}^θ employed in this study is given by

$$k_{ij}^\theta = \frac{k_{ij(dreiding)}^\theta}{\sin^2 \theta_{ij0}} \quad (5.20)$$

This approach may lead to marginally lower accuracy but allows reasonable predictions to be made for novel combinations of the elements simulated in this work.

The repulsive potential described by Equation (4.8) was also employed in this work to minimize the occurrence of significant overlapping of neighbouring atoms or groups.

During the relaxation process the acceptance or rejection of a new trial configuration follows the usual Metropolis Monte Carlo prescription. At least 500 trial MC simulation moves are conducted between each KMC event and independent evaluations of the –O-Si-O-/Si-O-Si- configurational properties such as the atomic RDFs and bond angle distributions have confirmed that the final

structures formed are consistent with the equilibrium structures observed for random networks of amorphous silica.

Atomic interaction	Bond stretching constant (MJ/mol/nm ²)	Bond bending constant (kJ/mol)	Equilibrium distance (nm)	Angle (°)
Si-O _c	292.9		0.1487	
CH ₂ -CH ₃	292.9		0.143	
O _c -CH ₂	292.9		0.132	
Si-O _c -CH ₂		558		$\theta_{Si-Oc-CH2,0} = 120$
O _c -CH ₂ -CH ₃		471		$\theta_{Oc-CH2-CH3,0} = 109.471$

Table 5.4. Potential parameters used for relaxation of the deposited solid films.

Other parameters for the Si-O pairs, O-Si-O, Si-O-Si triplets and Si-OH are provided in Table 4.3.

In all of the runs conducted in this study the total length of the growth trajectory during the CVD simulation of the formation of a single layer was fixed at 8000 reaction events. For each thermodynamic condition (temperature and precursor pressure) and for both reagents, Si(OC₂H₅)₄ and Si(OH)₄, five independent layers were fabricated and the results reported in the following section therefore correspond to averages over 40,000 reaction events in each case.

Chapter 6. Kinetic Monte Carlo Simulation of the Formation of Thin Solid Films of Silica via Chemical Vapour Deposition: Results and Discussion

The internal architecture of nanoporous composite membranes formed during CVD has a significant influence on the equilibrium and/or kinetic selectivity of the resultant membrane for separating fluid mixtures. Therefore, to develop a more complete understanding of the key features of the deposited structure and the manner in which the experimental deposition conditions play a role in determining the membrane properties, one needs to characterize these nanoporous media in terms of morphological parameters such as local atomic and mass density distributions, pore sizes, voidage and spatial details of the membrane chemical composition.

6.1 Film Growth Rates

The most direct comparison with experiment which can be made is through the solid film growth rate, a macroscopic observable normally reported in studies of nanoscale thin film deposition. In Figure 6.1 the film growth rates at three temperatures for the films simulated in this work are reported over a range of precursor reagent pressures $10^{-4} < p_R < 1.5$ torr. For most of the conditions investigated the growth rates are linear in pressure as implied by the expression for the time increment, Equation (5.19). The exception is at the lowest temperature of 473K for TEOS. Under stationary conditions, the denominator of Equation (5.19) with TEOS as the precursor may be expressed as

$$\begin{aligned}
& \sum_{j=1}^{N_{BIN}} \left(\sum_{i=3}^{N_{Diss}} r_{i,j} + k_{2f} \left[< K_{TEOS,j} > N_{OH,j} \right] (p_{TEOS} / RT) \right) \\
&= \sum_{j=1}^{N_{BIN}} \left(\sum_{i=3}^{N_{Diss}} A_i N_{C_2H_5,i,j} \exp(-E_{A,i} / RT) \right. \\
&\quad \left. + k_{11} [N_{OH-HO,j}] + k_{2f} \left[< K_{TEOS,j} > N_{OH,j} \right] (p_{TEOS} / RT) \right) \quad (6.1) \\
&= \left(\sum_{i=3}^{N_{Diss}} \left(\sum_{j=1}^{N_{BIN}} N_{C_2H_5,i,j} \right) A_i \exp(-E_{A,i} / RT) \right. \\
&\quad \left. + k_{11} \left(\sum_{j=1}^{N_{BIN}} N_{OH-HO,j} \right) + k_{2f} (p_{TEOS} / RT) \left(\sum_{j=1}^{N_{BIN}} < K_{TEOS,j} > N_{OH,j} \right) \right)
\end{aligned}$$

During the deposition process at low temperatures the ethoxy dissociation reactions (on the left of the last expression in (6.1)) occur with frequencies commensurate with the TEOS deposition term shown on the right of the above expression. The growth rate, however, is not a simple linear function of pressure in view of the direct increase in the ethoxy concentration level (the first term on the left of Equation (6.1)) within the deposited film at higher deposition pressures. This results in the nonlinearity in the growth curves observed in Figure 6.1 at low temperatures. At high temperatures (and at low pressures in all cases), the ethoxy dissociation reactions occur very frequently relative to the deposition reaction with the result that for each TEOS molecule deposited the three ethyl moieties remaining in the surface group as indicated by the right hand side of reaction R2 must first be stripped before another TEOS molecular deposition can take place. As will be demonstrated below this does indeed lead to low levels of carbon in the deposited films, however, while the dissociation reactions R3-R7 do take place independently of all other reactions in the system there are exceptions to this sequence of full carbon depletion prior to deposition of a TEOS molecule. Hidden constraints exist for the dissociation reactions R8-R10 since suitable ‘glass bond’

siloxane oxygens are required in the neighbourhood of these ethoxy groups for each of these reactions to proceed. The absence of such an oxygen will result in the retention of the ethoxy moiety. A subsequent reaction may produce a suitable glass bond oxygen and allow for its removal, however it is clear that in general ethoxy dissociation not entirely independent of the other reactions.

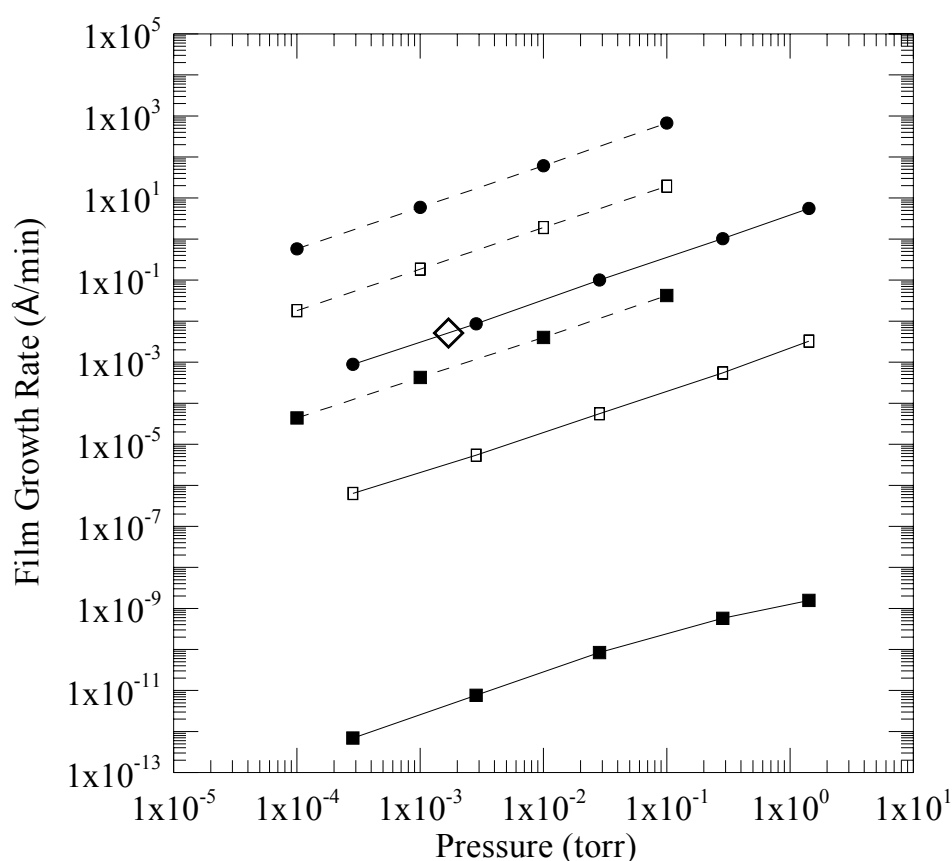
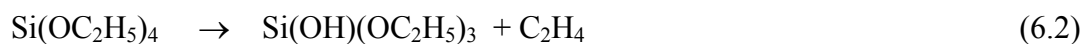


Figure 6.1. SiO_x film growth rate as a function of precursor pressure. Dashed lines: silicic acid precursor; full lines: TEOS precursor. Deposition temperature: ■ 473K; □ 673K; ● 873K. The large open diamond corresponds to the deposition rate reported by Coltrin et al (2000) for a cold molecular beam of TEOS depositing at 1.7×10^{-3} torr onto a substrate maintained at a temperature of 873K.

The open diamond symbol shown in Figure 6.1 at a pressure of 1.7×10^{-3} torr and 873 K is the growth rate under these conditions estimated from data reported by Coltrin et al (2000) for cold (25°C) molecular beam deposition onto a substrate surface maintained at 873 K. Under these conditions it has been noted that molecular dissociation of TEOS in the gas phase is negligible. At high gas phase temperatures however Coltrin et al have clearly demonstrated that dissociation reactions within the gas phase prior to deposition are of paramount importance. This is evident from the simulation results shown in Figure 3 and the experimental data of Desu (1989) for CVD at high temperatures. Coltrin et al (2000) have made a detailed comparison with the experimental observations reported by Desu and conclude that the gas phase dissociation reaction



with rate constant $k = 4.9 \times 10^{13} (\text{sec}^{-1}) \exp\left(-\frac{257.15 (\text{kJ/mol})}{RT}\right)$, is the most significant gas phase decomposition reaction and greatly influences the thin solid film growth rate at high temperatures. By including the dissociation reaction in Equation (6.2) within the set reported in Table 5.1, they have demonstrated good agreement with the data reported by Desu over the reaction limiting range from 893K to 1000K (at higher temperatures the deposition process becomes diffusion limiting as indicated by the nonlinearity in the data in Figure 6.2 for $T > 1000\text{K}$). The omission of gas phase reactions in the studies reported here, and in particular the formation of the intermediate $\text{Si(OH)(OC}_2\text{H}_5)_3$ in the gas phase, serves to explain, at least in part, the under-prediction by the KMC simulation results for TEOS in Figure 6.2.

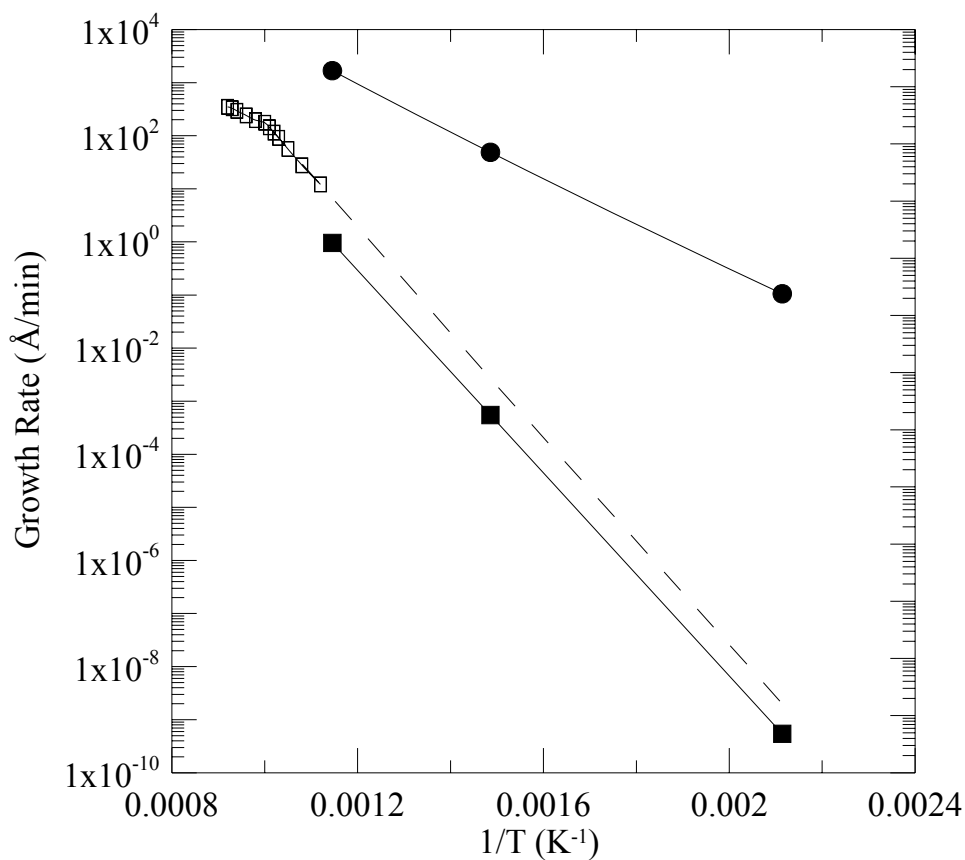


Figure 6.2. SiO_x film growth rate as a function of temperature at a fixed precursor reagent pressure of 0.25 torr. ■ kinetic Monte Carlo simulation results for TEOS employing the reactions R2-R11; ● kinetic Monte Carlo simulation results for Si(OH)₄ employing the reactions R1 and R11; □ experimental data reported by Desu (1989) for the temperature range 893K-1083K (the dashed line is the extrapolation of a fit to the experimental data proposed by Desu).

At 873K the KMC growth rate is approximately six times smaller than the estimate provided by Desu's correlation (the dashed line in Figure 6.2). While the

agreement would appear to be improved at lower temperatures (within a factor of 3 at 473K) it is clear that, in general, for a more complete analysis of the deposition process, computations based on additional data provided by a knowledge of the specific configuration, internal gas phase distribution pattern and thermal states within the CVD reactor involved would be required. The KMC method employed in this work should provide reliable results for systems with low gas phase reaction times or low temperature molecular beam deposition onto hot surfaces.

The Si(OH)_4 simulation results reported in Figures 6.1 and 6.2 are indicative of an upper bound in the deposition rates for the limiting case in which TEOS, and other alkoxysilanes, have been stripped of their carbon content in the gas phase prior to deposition. At 873 K the growth rate for silicic acid as the precursor is approximately three orders of magnitude larger than estimated for undissociated TEOS and two orders of magnitude larger than the film growth rate provided by the experimental data reported by Desu (1989) for TEOS in which, as noted above, the reactive intermediate $\text{Si(OH)(OC}_2\text{H}_5)_3$ is considered to play a major role during the deposition process. As will be shown below, this also has a direct bearing on the precursor dependence of the atomic structure of the resulting thin films formed during layer growth.

6.2 Film Mass and Number Density Profiles

The mass density profiles obtained for a selected set of simulation runs are shown in Figure 6.3. The background substrate (see Figure 5.1) corresponds to the region $z < 0$ and the densities in this region for the deposited material starts at 0.0 where penetration of the depositing silicic acid or TEOS cannot take place. In the

inhomogeneous region at the surface of the substrate ($z = 0$) the density initially passes through a maximum before leveling off at a layer thickness of approximately 1-2 nm. From the profiles it is clear that the average densities of the silica films (see Figure 6.4) in the homogeneous region $z > 2\text{nm}$ decreases with increasing substrate/deposition temperature and, for Si(OH)_4 deposition, with increasing precursor pressure (statistically, with standard errors $\sim \pm 2\%$, the densities of the TEOS films are essentially independent of pressure although the low temperature deposition results do indicate a systematic density reduction of approximately 2.3% at the highest pressure studied). To explain these observations we note that there are two competing effects relating separately to temperature and pressure involved during the deposition process. High temperature conditions encourage minimal hydroxyl content through hydroxyl group condensation (reaction R11) and this is evident from the results for the atomic number density profiles shown in Figures 6.5 and 6.6. During deposition the removal of OH groups via condensation at a given pressure results in fewer sites for subsequent deposition and leads to a lowering of the density locally within the medium and a more open pore structure. Local condensation reactions deep within the layer also result in the appearance of nano-cavities and both of these effects are most significant for high temperature deposition conditions. Conversely, at a given temperature increasing the deposition pressure enhances the deposition rate and during Si(OH)_4 CVD this leads to a significantly higher OH content. The latter effect results in a greater degree of steric exclusion of neighboring atomic groups by dangling silanol groups prior to silanol condensation with the subsequent creation of larger voids within the evolving film. Furthermore, while the presence of the ethyl moieties during TEOS deposition encourages the formation, on dissociation, of larger nano-cavities (and

hence lower densities than solid films based on silicic acid) the trend towards lower densities at higher temperatures in these media would also appear to be primarily related to silanol condensation and dehydration.

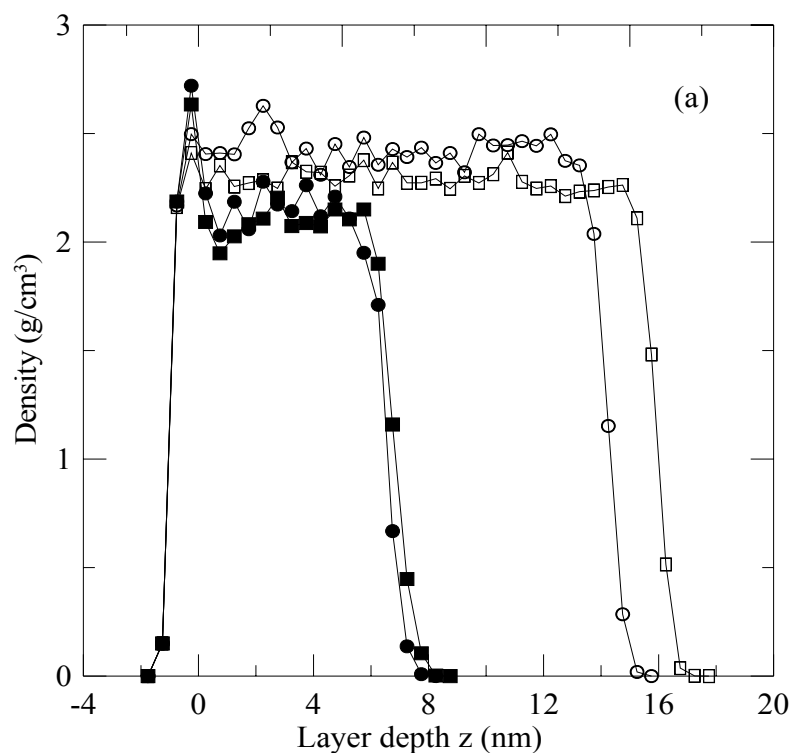


Figure 6.3(a). The mass density as a function of layer depth for silicic acid deposition (open circles at 1×10^{-4} torr and open squares at 0.1 torr) and TEOS deposition (filled circles at 2.84×10^{-4} torr and filled squares at 1.42 torr) at 473 K.

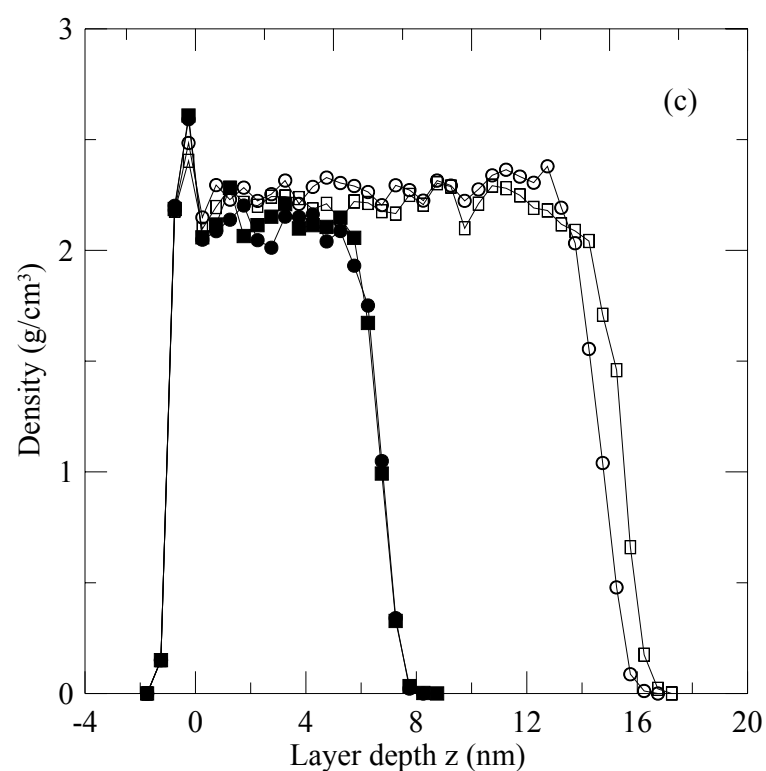
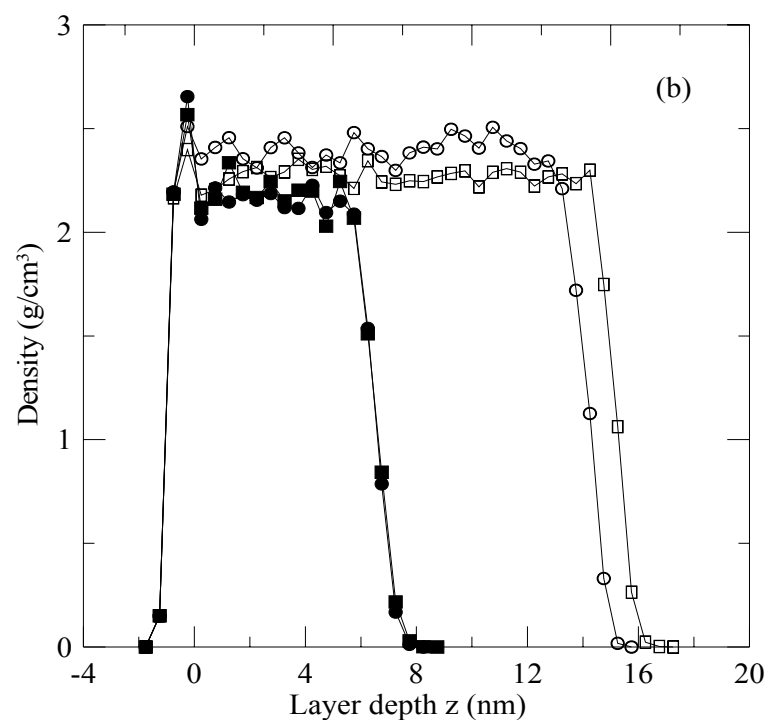


Figure 6.3(b,c). The mass density as a function of layer depth for silicic acid deposition (open circles at 1×10^{-4} torr and open squares at 0.1 torr) and TEOS deposition (filled circles at 2.84×10^{-4} torr and filled squares at 1.42 torr) at (b) 673 K and (c) 873 K.

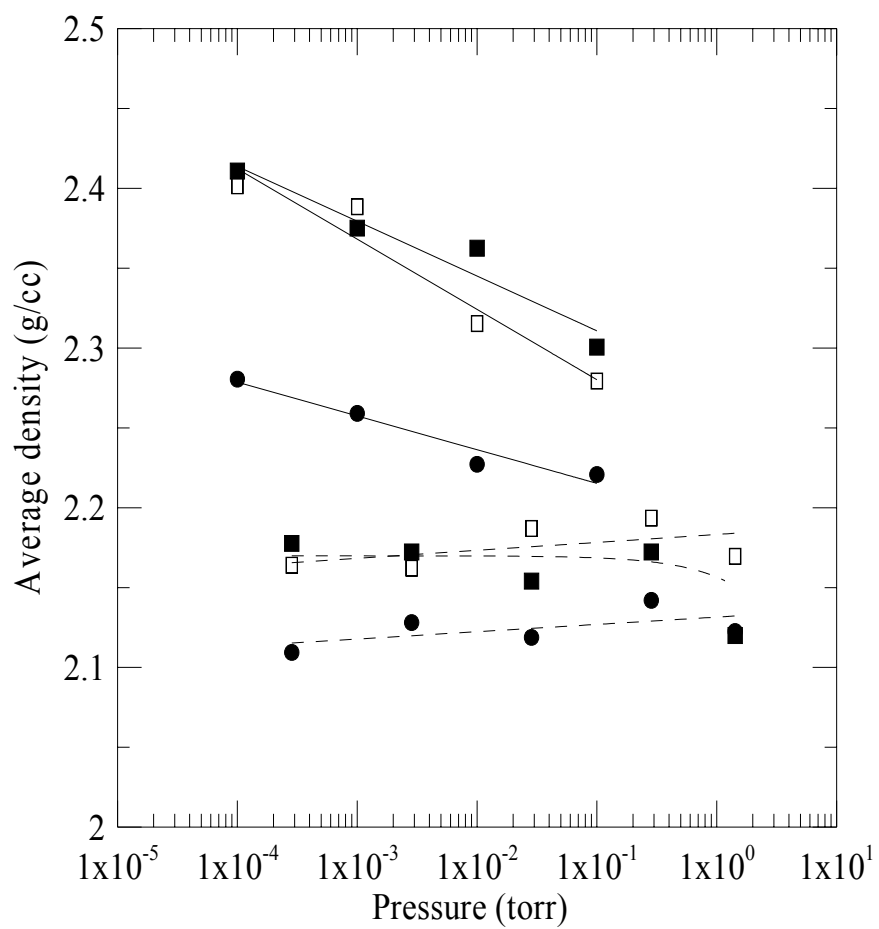


Figure 6.4. The average mass density as a function of deposition pressure for silicic acid deposition (full lines) and TEOS deposition (dashed lines) at ■ 473K; □ 673K; ● 873K.

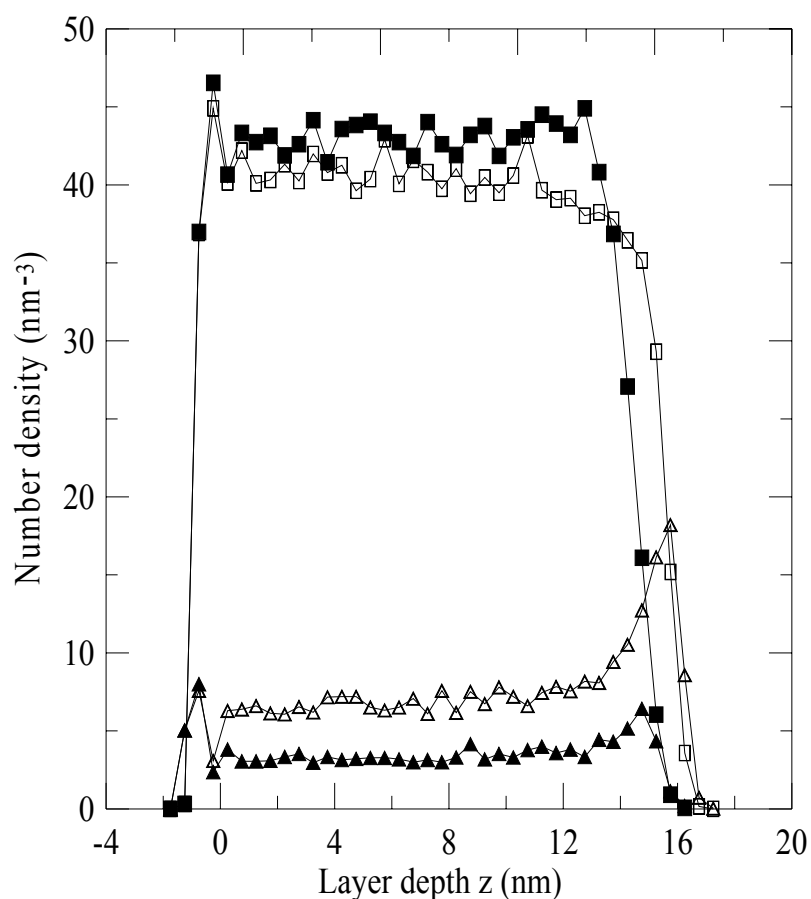


Figure 6.5. The oxygen atomic number density profiles with $\text{Si}(\text{OH})_4$ employed as precursor. The open and filled squares correspond to siloxane (or bridging) oxygens and the open and filled triangles correspond to the hydroxyl oxygens. The open symbols refer to the lowest temperature (473 K) and highest pressure ($p_{\text{Si}(\text{OH})_4} = 0.1$ torr) and the filled symbols refer to the highest simulated temperature (873 K) and lowest precursor pressure (1×10^{-4} torr).

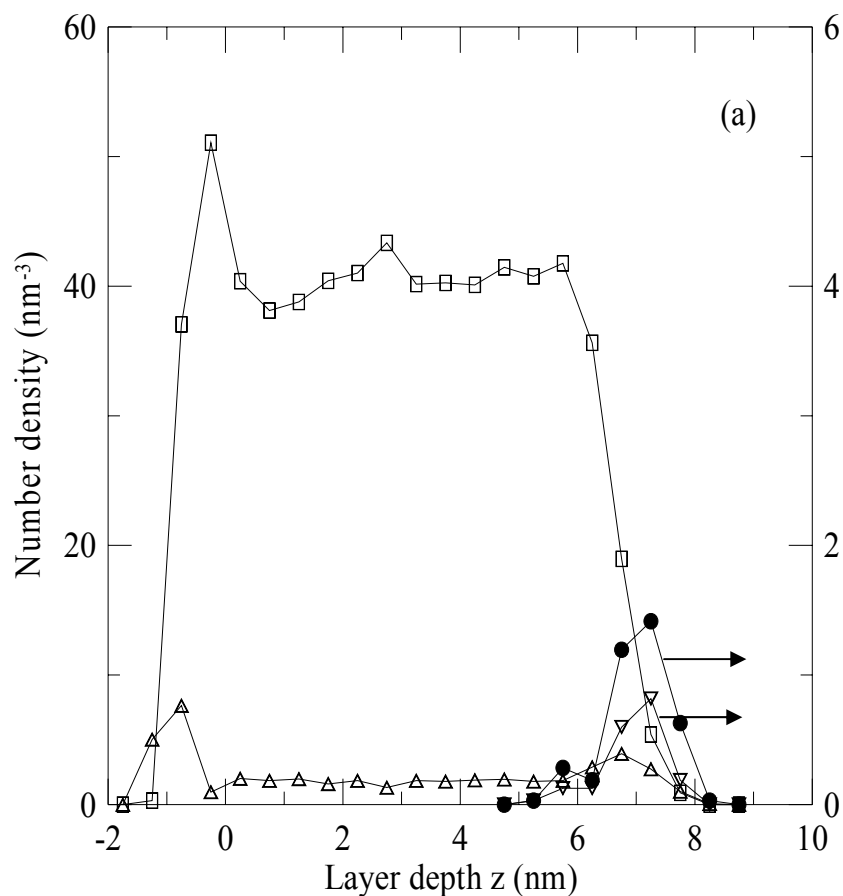


Figure 6.6(a). The oxygen and carbon atomic number density profiles with TEOS employed as precursor at 473K and a precursor pressure of 1.42 torr. The open symbols correspond to the oxygen atoms: \square siloxane (or bridging oxygens); \triangle hydroxyl oxygens; ∇ ethoxy oxygens. The filled circles correspond to the carbon atoms (in both $-\text{CH}_2$ and $-\text{CH}_3$). Note the change in reference axis for the ethoxy oxygens and the carbon atoms.

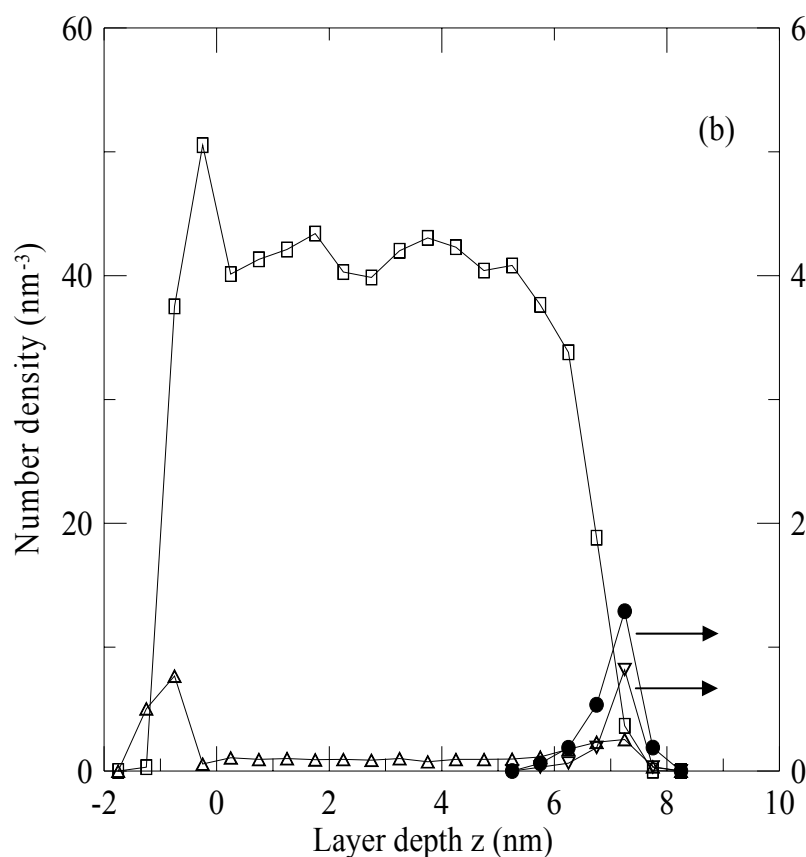


Figure 6.6(b). As in Figure 6.6(a) but at 873K and a precursor pressure of 2.84×10^{-4} torr.

The carbon content of the films formed during TEOS deposition is also sensitive to temperature and pressure with the least carbon remaining, as anticipated, at the highest temperature and lowest pressure. However even in this case there is still a significant level of carbon remaining in the film (primarily within 3 nanometres of the surface). This ‘contamination’ is common in CVD processes employing alkoxysilanes as precursors with the carbon content being particularly high at high precursor pressures (flowrates) and/or low temperatures (Ramamoorthy et al (2008)). To illustrate more clearly the carbon composition dependence on temperature and pressure the results for the number fraction $x_{C_2H_5}$ of the ethyl groups (relative to the total number density of the silicon, siloxane

oxygen, hydroxyl groups, ethoxy oxygens and ethyl groups) remaining in the top 3.5 nm of the deposited films as a function of TEOS pressure are reported in Figure 6.7 (no residual carbon was observed deeper within the layers during the simulations). These results were obtained from running averages over samples of the 3.5 nm surface interfacial zone during the last half of the film growth trajectory.

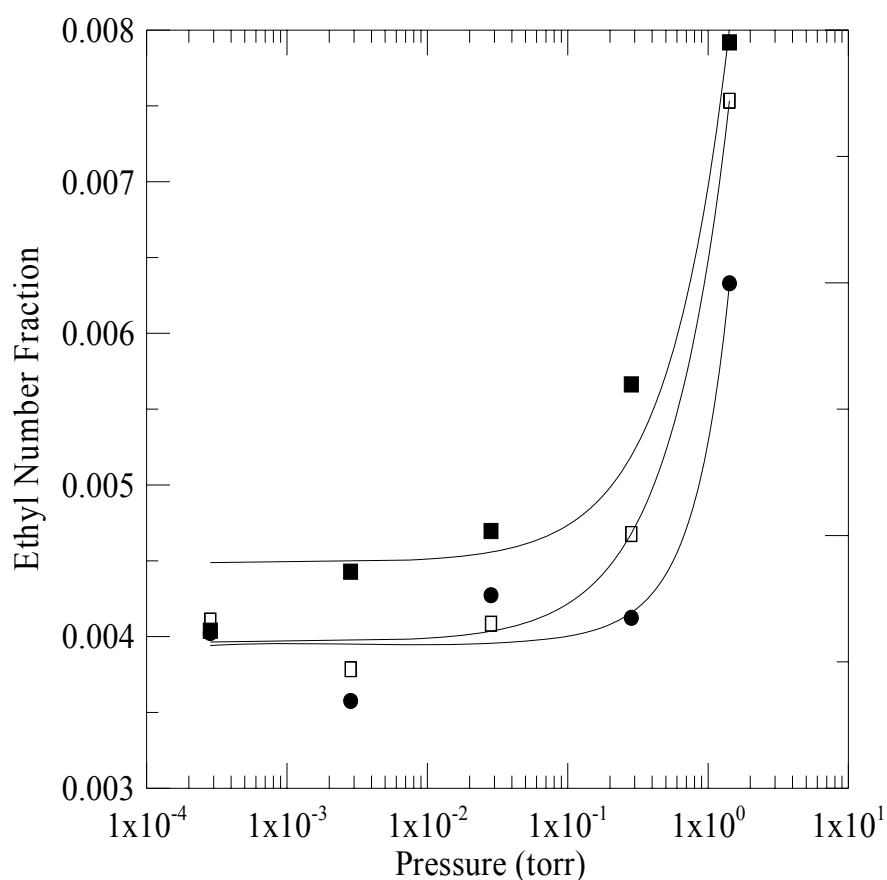


Figure 6.7. Ethyl number fraction in the 3.5 nm thick surface layer of the TEOS based CVD films as a function of precursor pressure at: ■ 473K; □ 673K; ● 873K.

At 473K the carbon content is highest, increasing significantly with increasing TEOS pressure. As the deposition temperature is increased the carbon levels at a given precursor pressure only diminish marginally and it is clear that even at high

temperature and low pressures between 0.4% and 0.5% carbon can remain in the top 3-4 nm interfacial region of the solid film. In a process setting, removal of this would normally require thermal treatment (continued dissociation via reactions R3-R10 in the absence of deposition) and/or oxidation with O₂ or O₃.

An important outcome from the KMC simulations is the demonstration of the dependence of film mass density and molecular structure not only on the thermodynamic conditions for the deposition process but also on the precursor employed. The films obtained with the molecularly larger of the two precursors result in layers with significantly lower densities. For example, from Figure 6.4 the density within the homogeneous region of the Si(OC₂H₅)₄ film deposited at 873K is approximately 2.1 g/cm³ while that for Si(OH)₄ deposition is close to 2.3 g/cm³. The lower densities observed for TEOS are not an uncommon observation in experimental CVD studies (Haupfear et al (1994), Yin et al (2004)) in which film densities as much as 10% lower than the density of bulk amorphous glass have been observed. Precursor controlled SiO_x film density has also been proposed for applications as low-k dielectric films (see for example Mountsier (2000)). These materials and techniques, with appropriate selection of the thermodynamic deposition conditions, may also be employed in the development of controlled pore composite membranes for molecular size selective separation of the components of gas and liquid mixtures.

6.3 Pore size distributions and void accessibilities

Selected results for the pore size distributions (PSDs) for the homogeneous regions of the density profiles reported in Figures 6.3(a) and 6.3(c) are shown in

Figure 6.8. These distributions were determined using the algorithm developed by Bhattacharya and Gubbins (2006). According to this method the pore size in the structure at a given point is defined by the largest diameter of a sphere that encompasses the given point without overlapping the neighbouring atoms in the system. Enumerating the pore sizes in this manner it is straightforward to establish the normalised pore size distribution for each of the simulated structures formed via the KMC CVD algorithm.

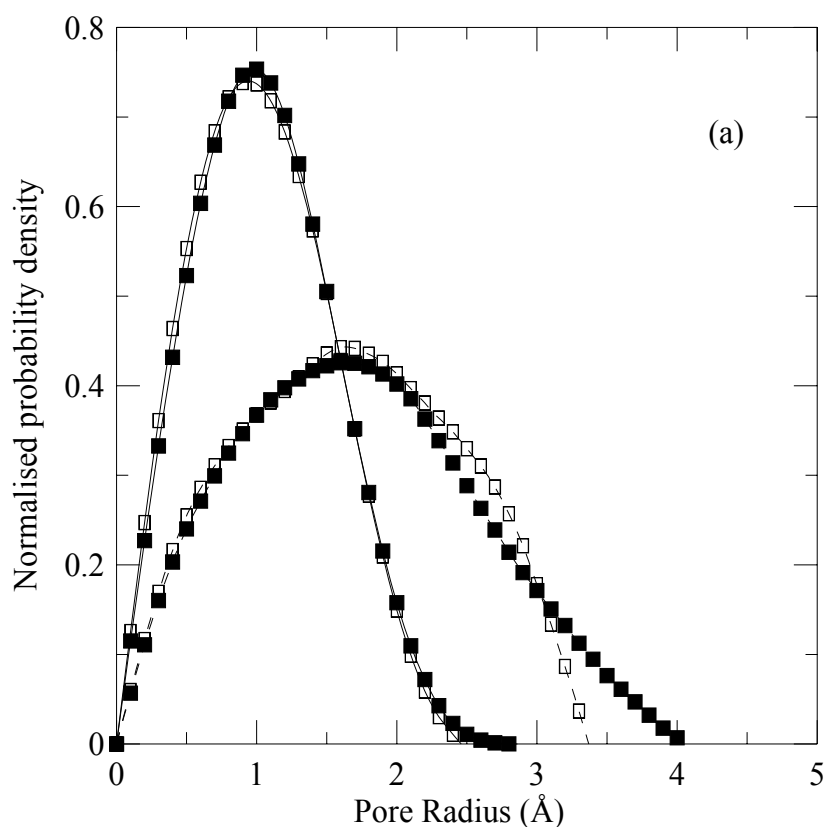


Figure 6.8(a). Pore size distributions for CVD layers formed by deposition of Si(OH)_4 (full lines) and TEOS (dashed lines) $T = 473$ K. Filled squares correspond to the highest pressure investigated (0.1 torr for Si(OH)_4 and 1.42 torr for TEOS) and the open squares refer to the lowest pressure (10^{-4} torr for Si(OH)_4 and 2.84×10^{-4} torr for TEOS).

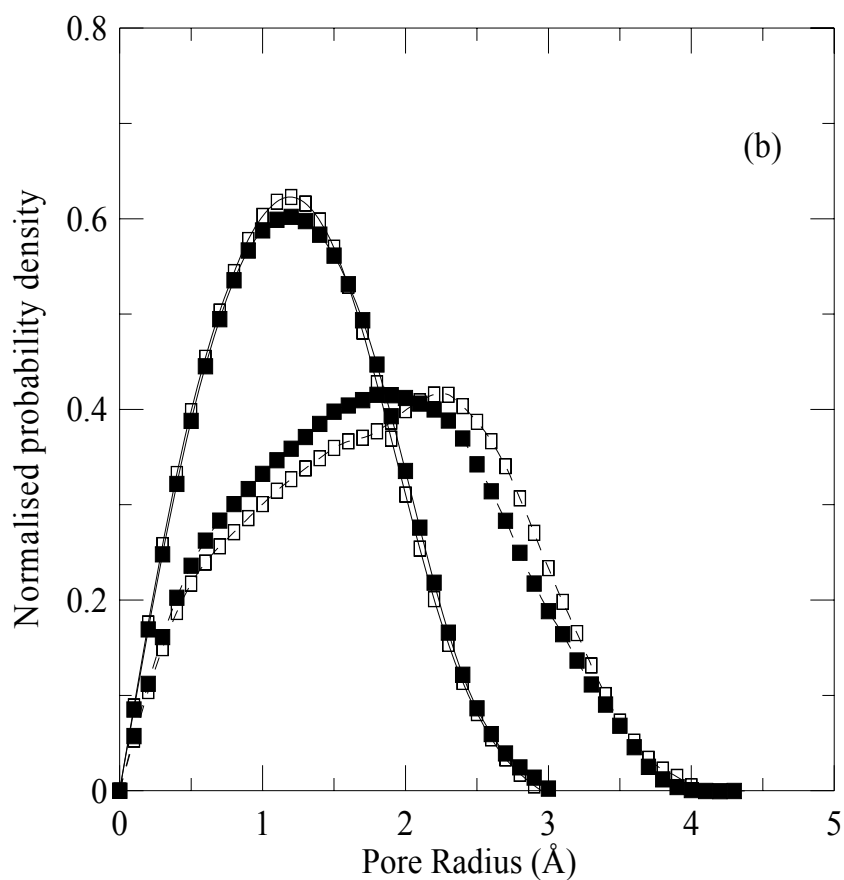


Figure 6.8(b). As in Figure 6.8(a) but for $T = 873\text{K}$.

For high deposition temperatures the PSDs are relatively broad with a maximum pore radius of 4.1\AA and 3.0\AA for TEOS and silicic acid respectively clearly illustrating the influence of the molecular size of the individual precursors. The influence of precursor pressure in controlling the pore size is also seen in the low temperature TEOS deposition results with a significant reduction in the maximum pore radius from 4.0\AA to 3.4\AA . The results at high temperature however are only marginally affected by pressure.

The influence of precursor molecular size, and to a lesser extent the deposition thermodynamic conditions, is also very much in evidence from the average pore radii of ~ 1.65 - 1.85 Å (TEOS) and ~ 1.05 - 1.25 Å (Si(OH)_4) as shown in Figure 6.9. The results for the average pore radii inversely follow the trends observed in Figure 6.4 for the average density of the films. For both precursors the average pore radii increase with temperature which we believe is due to the lower OH content within the high temperature films. For fluid mixture separations however, the added variability, and hence control, of pore size depending on the precursor employed is most significant and should be a key factor for consideration in the fabrication of size (or kinetically) selective membranes.

To provide additional insight into the influence of the pore accessibility of these films can have on their selectivity and to assess possible changes in morphological characteristics vis-à-vis deposition conditions, a series of computations have been performed to evaluate the hard core partitioning of a range of simple gas species between the bulk gas and the pores of the films formed in these simulations. A simple random insertion routine has been employed on the homogeneous region of the films in the range $1.5 \text{ nm} < z < 12.0 \text{ nm}$ and $1.5 \text{ nm} < z < 5.0 \text{ nm}$ for layers formed by silicic acid as precursor and TEOS as precursor, respectively, for a hard point particle, Helium (with a hard sphere atomic diameter equal to its Lennard-Jones collision diameter $\sigma = 0.228 \text{ nm}$ (Chakravarty (1997))), Oxygen (diatomic with a hard atomic diameter $\sigma = 0.3106 \text{ nm}$ and an interatomic distance $\ell = 0.09699 \text{ nm}$), Nitrogen (diatomic with a hard atomic diameter $\sigma = 0.3321 \text{ nm}$ and an interatomic distance $\ell = 0.10464$) and carbon dioxide (a triatomic, linear molecular with hard atomic diameters $\sigma = 0.3064 \text{ nm}$ (O) and σ

= 0.2785 nm (C) with a carbon-oxygen interatomic distance $\ell = 0.1161$ nm). These parameters are the same as those employed in Chapter 4 and the σ values for the atoms in O₂, N₂ and CO₂ are taken from Schumacher et al (2006a,b).

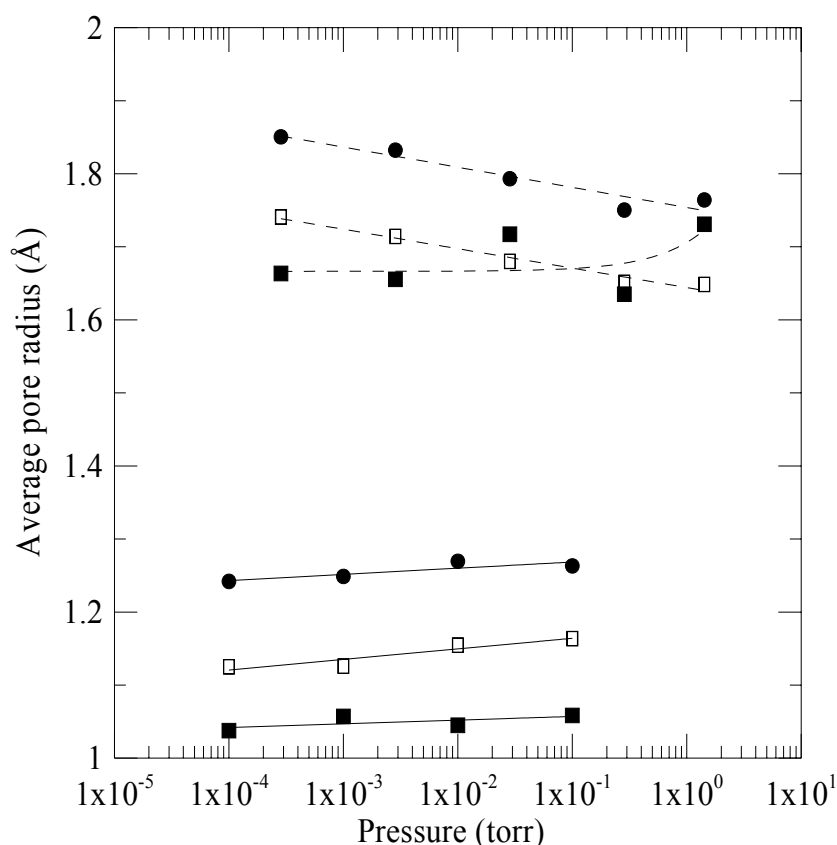


Figure 6.9. The average pore radius for the simulated nanoporous layers as a function of precursor pressure (upper curves: TEOS; lower curves: Si(OH)₄). ■ 473K; □ 673K; ● 873K.

A simple relationship based on models of the inserted particles as a hard sphere (Helium) or as hard spherocylinders (O₂, N₂ or CO₂) which correlates all of data for a given precursor quite well is given by Raghavan and MacElroy (1991)

$$\frac{\ln \psi_{Acc}}{\ln \psi_{Acc}(\sigma_f = 0)} = \left(1 + \frac{\sigma_f}{\sigma_s}\right)^3 + \frac{3}{2} \frac{\ell_f}{\sigma_s} \left(1 + \frac{\sigma_f}{\sigma_s}\right)^2 \quad (6.3)$$

Density variations between configurations are cancelled to a significant degree in the ratio on the left hand side of Equation (6.3). The single fitting parameter in this expression is σ_s , the effective diameter of the solid exclusion ‘particles’ which make up the silica structure. Equation (6.3) is based on the assumption that the solid exclusion particles are overlapping spheres distributed at random within the medium and while the correlation of the void accessibility data is very good, the actual silica structures are not entirely random (in particular long range topological constraints are present due to bond connectivity throughout the silica network). For this reason the fitting parameter σ_s does depend to some extent on the origin of the film (notably the precursor employed): for all of the layers formed with silicic acid as the precursor $\sigma_s = 0.324$ nm and for the TEOS based systems $\sigma_s = 0.422$ nm, intermediate between the size of the siloxane oxygen/hydroxyl group and an effective size for the silica tetrahedra. The parity plot provided in Figure 6.10 demonstrates the relative accuracy of Equation (6.3) for all of the simulations conducted in this work.

Most of the Helium data are in the region of or above the limiting value of 0.03 and the results represented by the open squares and triangles in the vicinity of $\psi = 0.03$ are the data for TEOS related layers. The results in the lower left hand corner of Figure 6.10 are for O₂, N₂ and CO₂ distributing within silicic acid based films. While in general the ability of Equation (6.3) to correlate the data over 3-4 decades of voidage values is very good, there does appear to be some dependence on the deposition temperatures. The variation across the parity line, from left-to-right, for

a given gas would appear to be correlated primarily with increasing temperature and a reduction in the concentration of OH groups at high temperatures.

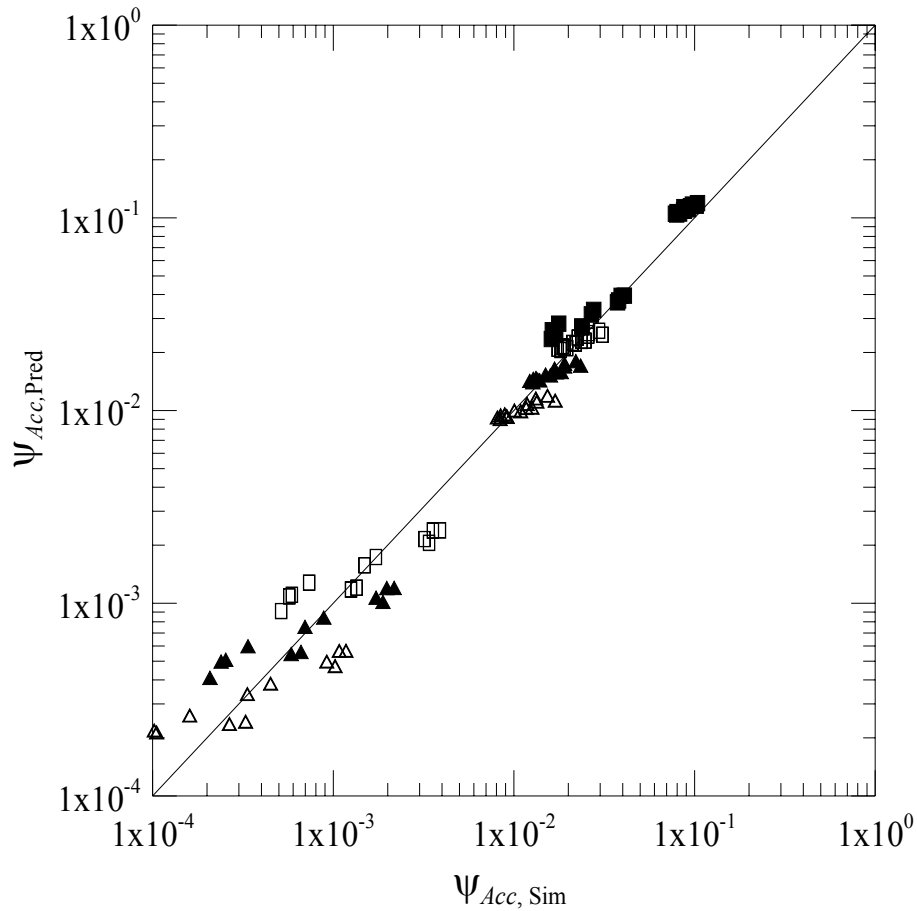


Figure 6.10. Parity plot for the accessible pore volumes predicted using Equation (6.3) and the results obtained by direct MC simulation: ■ Helium; □ Oxygen; ▲ Nitrogen; △ Carbon dioxide.

6.4 Concluding observations

To conclude this Chapter, an approximate analysis for permeation across hypothetical silica films is conducted based on the following observations. The morphological characteristics of the layers formed via silicic acid deposition are very similar to the properties of the silica systems prepared by etching as described

in Chapter 4. To demonstrate this, the properties of a range of systems are reported in Table 6.1.

	Etched Structure Density	Si(OH) ₄ Deposit $T, p_{\text{Si(OH)}_4}$	Etched Structure Density	Si(OH) ₄ Deposit $T, p_{\text{Si(OH)}_4}$	Etched Structure Density	Si(OH) ₄ Deposit $T, p_{\text{Si(OH)}_4}$
	1.73 g/cc	873K 0.01 torr (2.23 g/cc)	1.86 g/cc	673K 0.1 torr (2.28 g/cc)	1.97 g/cc	473K 0.01 torr (2.36 g/cc)
R_p	0.128 nm	0.127 nm	0.115 nm	0.116 nm	0.105 nm	0.105 nm
ψ_{CO_2}	0.0018	0.0012	0.00055	0.00045	0.000116	0.000102
ψ_{N_2}	0.0031	0.0022	0.00105	0.00089	0.000260	0.000254
ψ_{He}	0.0559	0.0409	0.0377	0.0276	0.0263	0.0163
$\psi(0)$	0.592	0.520	0.575	0.502	0.563	0.478

Table 6.1. Comparison of morphological properties of structures formed by etching (Chapter 4) and those computed from thin films formed via Si(OH)₄ CVD.

In all cases the pore radii determined as described earlier are consistent across pairs of systems. Furthermore, although not shown here, the pore size distributions for the three pairs of systems reported in Table 6.1 are also very similar and the accessible pore volumes for the two gases CO₂ and N₂ are also seen to be in good agreement. In the latter case the overestimates for the etched structures are reflected to a greater extent in the relative differences between the Helium and point particle void accessibilities for the individual pairs of structures. The primary reason for these discrepancies is a consequence of the manner in which the etched structures are produced. The random removal of a silicon atom with subsequent

‘condensation’ of the singly bonded oxygens leads to the formation of ‘SiO_x ghost’ holes within the structure which would not normally be expected to occur during the more realistic CVD process. These holes also account for the significant disparity in the structure densities even when many of the other structural features of the pairs of solids are very similar (see, for example, the etched structure of 1.97 g/cc and the deposited film with the same average pore size which closely conforms to its structural features).

These observations suggest that the domains (in particular the freely permeable ‘superconducting’ channels of these structures) within which transport of the gases takes place for a given pair of media are one-to-one equivalent and to facilitate estimation of permeation properties the following tentative assumptions are made:

- (1) The ‘superconducting’ channels, and hence the percolation cluster sizes, within the layers formed via CVD are similar to those within the twinned etched media.
- (2) Diffusion within the poorly conducting domains of the deposited layers will be assumed, in the first instance, to be the same as in the corresponding domains of the etched structures. This assumption along with assumption (1) will be referred to as case (1/2) in the discussion below.
- (3) Assumption (2) will be replaced by the more realistic assumption that the diffusivities for N₂ and CO₂ within the poorly conducting domains of the deposited structures are more closely related to values for vitreous silica given the significantly higher densities of the deposited materials (in assumption (2) the lower density of the etched structures

allows for greater vibrational freedom in the silica network and hence the possible existence of low energy barriers for diffusive jumps to take place within these media). The analysis based on this assumption and assumption (1) will be referred to as case (1/3) below.

The five parameters required to estimate the permeance for a given gas species using Equation (4.13) are the Henry's law adsorption equilibrium coefficient, the diffusivity of the species in the infinite medium, the percolation cluster size, ℓ , the inhomogeneity factor, δ , and the nanopore accessibility coefficient, χ . Based on non-equilibrium molecular dynamics simulations reported by Moloney (2011) it may be inferred that as a reasonable approximation the group of terms $\chi \exp(\delta / \ell)$ is ~ 1.0 for each gas species. The Henry's law K values for each of the gases in the individual etched structures are computed from the canonical average of the Boltzmann factor as estimated via the Widom insertion algorithm (see Chapter 5 for its application locally to subcells in the solid film)

$$K_i = \frac{1}{V} \int_V \left\langle \exp \left(- \frac{U(\mathbf{r}')}{k_B T} \right) \right\rangle_{\Omega} d\mathbf{r}' \quad (6.4)$$

where V is the volume of the fundamental cubic cell described in Chapter 4. A total of 10^8 trial insertions were performed for each of the etched media reported in Chapter 4 with canonical averaging over orientations of the inserted species and averaging of the 25 nanoporous silica configurations in each case. The results obtained at 873K were:

1.73 g/cc: $K(\text{N}_2) = 0.22$ and $K(\text{CO}_2) = 0.67$

1.86 g/cc: $K(N_2) = 0.15$ and $K(CO_2) = 0.43$

1.97 g/cc: $K(N_2) = 0.097$ and $K(CO_2) = 0.26$

For case (1/3) in which assumption (3) is made, the diffusion contribution to Equation (4.13) is estimated using the Henry's Law values $K(N_2) = 0.017$ and $K(CO_2) = 0.04$, which are computed using the amorphous silica structure of density 2.2 g/cc from which the etched structures in Chapter 4 were obtained. The diffusion coefficients used in this set of calculations are based on the reported diffusivities for N_2 and CO_2 in vitreous silica: for N_2 Kajihara et al (2007) report $D_{N_2} \sim 1.3 \times 10^{-8} \exp(-14657/T) \text{ m}^2/\text{s}$ and for CO_2 Behrens(2010) provides $D_{CO_2} \sim 3.8 \times 10^{-9} \exp(-14220/T) \text{ m}^2/\text{s}$. These expressions give $D_{N_2} = 6.645 \times 10^{-16} \text{ m}^2/\text{s}$ and $D_{CO_2} = 3.204 \times 10^{-16} \text{ m}^2/\text{s}$ at 873K.

The permeances for N_2 and CO_2 for the three etched materials at 1.73 g/cc, 1.86 g/cc and 1.97 g/cc for case (1/2) are shown in Figure 6.11(a) as functions of the membrane thickness using Equation (4.13). The resulting permselectivities defined by

$$\alpha = \frac{P_{CO_2}}{P_{N_2}} \quad (6.5)$$

for each of the solids are reported in Figure 6.11(b). A corresponding set of results are provided in Figure 6.12 for case (1/3).

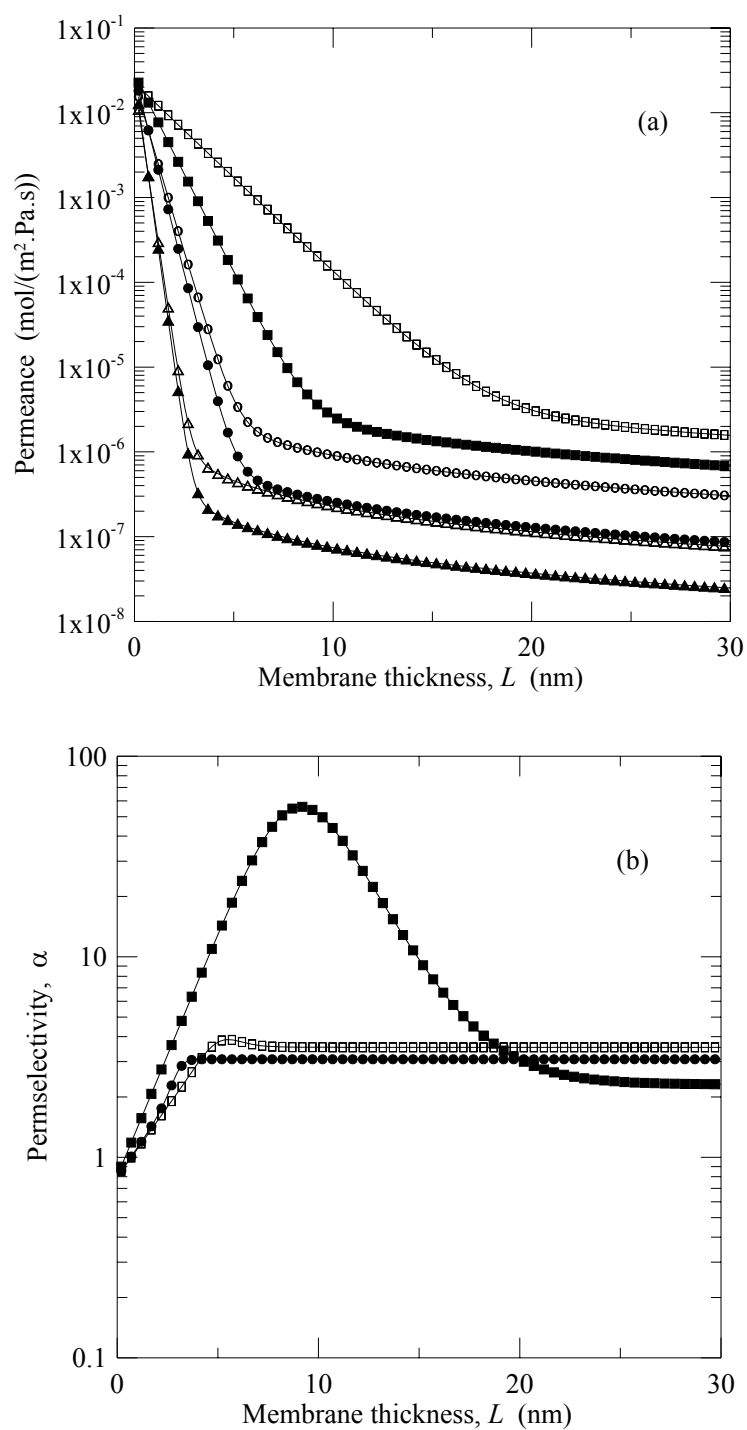


Figure 6.11. (a) Predicted permeances as functions of membrane thickness for CO₂ (open symbols) and N₂ (filled symbols) for etched model silica densities of 1.73 g/cc (squares), 1.86 g/cc (circles) and 1.97 g/cc (triangles) based on assumptions (1) and (2) in the text. (b) The permselectivities computed from the results shown in (a) for 1.73 g/cc (■), 1.86 (□) and 1.97 g/cc (●).

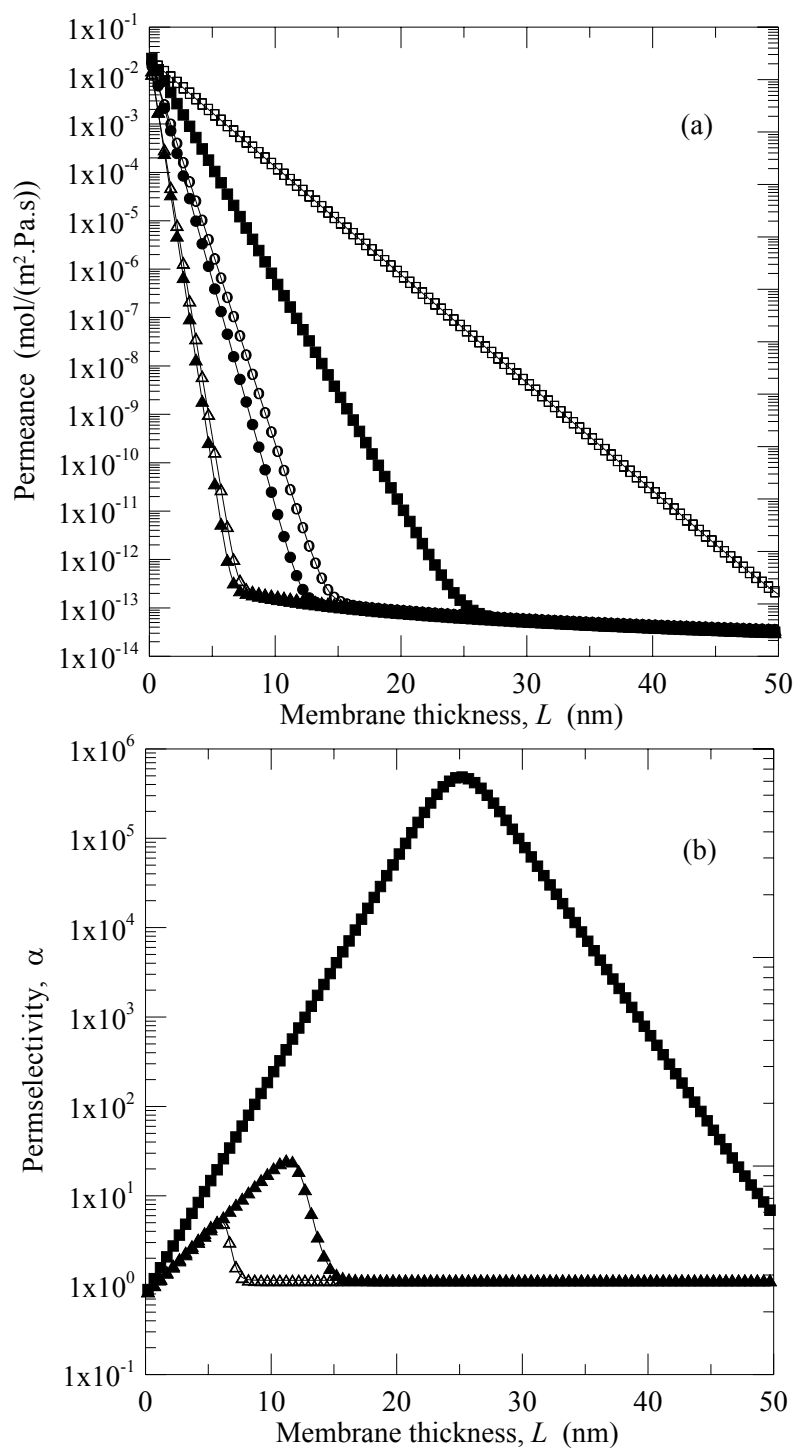


Figure 6.12. (a) Predicted permeances as functions of membrane thickness for CO₂ (open symbols) and N₂ (filled symbols) for silica densities of 1.73 g/cc (squares), 1.86 g/cc (circles) and 1.97 g/cc (triangles) based on assumptions (1) and (3) in the text. (b) The permselectivities computed from the results shown in (a) for 1.73 g/cc (■), 1.86 g/cc (▲) and 1.97 g/cc (△).

For case (1/2) an optimum (maximum) value for α of ~ 60 is observed at a membrane thickness ~ 9 -10 nm for the low density etched structure while the permselectivities for the two higher densities are determined solely by the DK/RTL term in Equation (4.13). In all cases the permeances for thick silica films are predicted to lie in the range $10^{-8} - 10^{-6}$ mol/m².Pa.s which, with one exception to be discussed below, are approximately 4 orders of magnitude larger than experimentally observed values. For case (1/3) maxima in the selectivities are observed at all densities, albeit relatively small values for the two higher densities. In this case however, the permeances are up to 3 orders of magnitude too low in comparison with reported experimental values.

Cuffe et al (2006) reported experimental measurements of permeance at a temperature of 873K for N₂ and CO₂ through CVD fabricated membranes which are reproduced in the table below.

CO ₂ Permeance (mol/m ² .Pa.s)	CO ₂ / N ₂ Selectivity	Deposition Temperature
4.3x10 ⁻¹⁰	8.2:1	600°C
7.3 x 10 ⁻⁹	11.3:1	600°C
3.0x10 ⁻¹¹	>36:1	670°C
6.9x10 ⁻¹¹	>75:1	600°C
2.8x10 ⁻¹¹	>275:1	500°C

Table 6.2 Experimental permeances measured at 873K and selectivities reported by Cuffe et al (2006) for membranes fabricated via CVD using TEOS as precursor.

The results reported by Cuffe et al refer to the observed values just after the point of pore closure on the substrate where the permeances of the individual gases dropped dramatically from their original values for the bare substrate. In these studies the substrate was Vycor porous glass with a nominal pore radius of 3-4 nm. Interestingly, this pore size (diameter) is close to the peak maximum in Figure 6.11(b) suggesting that pore closure alone without subsequent thin film build up resulted in the membranes prepared by Cuffe et al. The results in Figure 6.12 also imply that this is the case albeit for denser films. Unfortunately no electron micrograph images were taken of the deposited materials in this early work and the above comment cannot be confirmed.

The second issue of the magnitude of the permeances also needs consideration. The largest permeance recorded in Table 6.2 is close to the lower bound in Figure 6.11(a) and since the selectivity in this case is higher by a factor of three experimentally it is believed that case (1/2) does not adequately conform to observations. At this time it is suggested that the simulations which best agree with the results in Table 6.2 are those for case (1/3) with percolation cluster sizes similar to those in the 1.73 g/cc etched medium but with a poor conductor diffusivity, D_{CO_2} , which is intermediate to $0.5073 \times 10^{-9} \text{ m}^2/\text{s}$ (the 1.73 g/cc etched silica medium) and $3.204 \times 10^{-16} \text{ m}^2/\text{s}$ (for vitreous silica). In view of the recorded density of the twinned deposited silica film of 2.23 g/cc in this case this conclusion does not appear to be unreasonable. Additional studies are, however, required to evaluate both the percolation cluster sizes and diffusivities for silica media which more closely relate to the properties of the layers formed via TEOS deposition. In

light of the significant increase in the average percolation cluster size with both pore size and void accessibility as indicated in the results reported in Tables 4.4 and 6.1, it would also be reasonable to assume that this parameter will be larger still for the TEOS based silica films. The CVD results reported by Lee et al (2004) and Araki et al (2007) would suggest that this is indeed the case.

On the basis of the above comments it is believed that a central focus in future work on this topic should be the determination of the process parameters which will ultimately enable precise control of the parameter, ℓ , which itself largely determines both the magnitude of the peaks in Figures 6.11(b) and 6.12(b) and peak position relative to the membrane thickness. Density and temperature are two important control variables; however studies should be undertaken to ascertain the influence of the precursor, CVD reactor pressure, and the influence of inert and/or reactive diluent gases on the properties of the thin silica film. Process conditions clearly influence the magnitude of this quantity as may be inferred from the results reported by Araki et al (2007). Another element of control relates to the Fickian term involving D . Lowering the diffusivity enhances the relative importance of the non-Fickian contribution as clearly indicated by contrasting Figures 6.11 and 6.12 and this may be achieved by controlling film density and/or by introducing varying levels of other ionic species into the silica film (see for example Altemose (1961)). Ultimately however care will need to be taken (a) to ensure that the permeance is increased as much as possible (certainly greater than 10^{-8} mol/m².Pa.s for CO₂) to ensure separation capacity while achieving high selectivity and (b) to assess the stability of the ultrathin layer in the typically harsh environments in which oxide membranes of these kinds will find preferred applications.

Chapter 7. Conclusions and Recommendations

In this research the focus has been on efforts to resolve a number of outstanding issues in the characterisation and quantification of transport within nanoporous materials. Particular topics addressed were the mathematical description of diffusion in a model crystalline pore which represents a classical problem in the field of diffusion in porous materials and permeation within high density nanoporous silica membranes, a field which is growing in importance with the increasing demand for novel techniques which may be employed for separating gas mixtures (particularly those underpinning industrial performance in the energy sector).

A comparison between the results predicted via molecular dynamics and colour diffusion with pseudo-homogeneous expressions provided by linear response theory for a simple fluid confined within a model pore structure with embedded structural inhomogeneities confirms the validity of coarse grained analyses for the diffusion fluxes in porous media. A detailed investigation of the quasi-hydrodynamic theory of Pozhar and Gubbins (1993, 1997) for self-diffusion has also demonstrated both weaknesses and strengths in this comparatively sophisticated approach to transport in confined fluids. The strength of the theory lies in its emphasis on the importance of fluctuation phenomena around the equilibrium state and the need for a self-consistent formalism for transport in inhomogeneous systems. The principal weakness in the mathematical approach, however, is a reliance on the Boltzmann molecular chaos Ansatz, which is implicit in its Enskog-like binary collision integral analysis, and which fail to describe the dynamical properties of adsorbed fluids at low-to-moderate loadings due to the omission of recollisional events with the static adsorbent atoms within the evolution of the phase space trajectory. A similar problem arises at high densities where caging within the dense fluid also leads to significant recollisional effects not included in the formalism.

In a study of the diffusion processes of the light gases He, N₂ and CO₂ within dense amorphous silica systems, a novel approach has been proposed which describes the permeation characteristics of fluids through membranes in a unique way. The model allows one determine key parameters from a simulation of homogenous silica systems which may then be adapted to apply to a relatively complete description of the permeance of fluids in the barrier layers of composite membrane systems. The core of the theory is the superposition of two distinct modes of transport within disordered media:

- (a) anomalous diffusion which exists over time scales less than a few hundred picoseconds in length and which takes place on finite ‘superconducting’ clusters of channels within the disordered structure;
- (b) Normal Fickian diffusion which takes place within the underlying continuous background structure of the amorphous medium.

The existence of both these modes of transport is demonstrated by a deconvolution of the mean-square displacement of the centre-of-mass of the diffusing particles which ultimately results in a novel expression for the permeance of gases within the disordered system. The theory can explain experimental observations in a very simple way and demonstrates that, with appropriate control of experimental and process variables, highly selective membranes for difficult mixtures such as CO₂/N₂ may be fabricated.

To assist in the realisation of this last target, a kinetic Monte Carlo algorithm has been developed and applied to simulate thin silica film formation via chemical vapour deposition (CVD). The model algorithm is applied to the simulation of TEOS and Si(OH)₄ deposition onto nonporous silica substrates. While good quantitative agreement with reported experimental data has been demonstrated for layer growth rates, the primary objective of these studies has been to demonstrate that the KMC algorithm is able to provide valuable molecular level details of the

nanoporous thin films formed during the CVD process. The main observations to be drawn from the results are as follows:

- (a) High density films are formed during the CVD process. The densities, in the range 2.1 g/cc-2.4 g/cc, are sensitive to the precursor employed and, to a lesser extent, the thermodynamic conditions of the CVD process itself.
- (b) The morphological details of the silica films are similarly sensitive to the precursor employed. In particular depending on the alkoxysilane, $\text{Si(OH)}_{4-x}(\text{O}(\text{CH}_2)_n\text{CH}_3)_x$, employed and its pretreatment within the gas phase, the average pore diameter within the silica film formed via CVD may lie within a broad range from 0.2 nm to 0.4 nm, the tightest pores being formed when $x \rightarrow 0$.

The breadth of topics which require further investigation has been alluded to in the closing sections of each of the Chapters in this thesis. The development of an exact and tractable non-equilibrium statistical mechanical theory for inhomogeneous fluids is elusive however, with the mathematical analysis achieved by Pozhar and Gubbins, it can be stated that the current status of our understanding of this problem has reached a level commensurate with the theoretical standing of the kinetic theory of the homogeneous liquid state. Future advances in the latter will now have a direct bearing on achieving the goal of an exact unified approach to transport in porous media.

In the more explicitly applied field of transport in composite membranes and the fabrication of thin, highly selective solid films for separation of both gases and liquids, the protocols in the manufacturing process which directly influence the relative magnitude of the percolation cluster size, ℓ , for different pairs of fluid species will need to be defined precisely. In future work the KMC algorithm should be developed and applied directly to deposition onto microporous substrates and the properties of the oxide films formed by pore filling and layer growth examined in detail. An additional feature of the deposition process not included in this work but which

should form a key role in future studies is the inclusion of the reversibility of the reactions listed in Chapter 5 and most notably the hydration reaction. Hydrothermal treatment as well as thermal treatment of the silica layers formed via the algorithms described in this work should have a direct bearing on both the morphological properties and the chemical composition of the solid films. A challenging task will also be the development of a full suite of reactions required to accurately model deposition in plasma systems (most notably, plasma enhanced CVD) which is a rapidly growing field of research in the broad area of nanotechnology.

Bibliography

- Adams, D.J., *Molecular Physics*, **1975**, 29, 307.
- Akter, T, *Atomistic Simulation of Nanoporous Silica Layers: Deposition and Membrane Separation Characteristics*, **2010**, PhD Thesis, University College Dublin, Ireland.
- Al-Futaisi, A.; Patzek, T.W., *Physica A*, **2003**, 321, 665.
- Allen, M.P.; Tildesley, D. J., *Computer Simulation of Liquids*, **1987**, Oxford University Press, Oxford, United Kingdom.
- Altomose V.O., *J. Appl. Phys.*, **1961**, 32, 1309.
- Araki, S.; Mohri, N.; Yoshimitsu, Y.; Miyake, Y., *J. Membr .Sci.*, **2007**, 290, 138.
- Arnold, A.; Holm, C., *Computer Physics Communications*, **2002**, 148, 327.
- Ban, S., *Computer Simulation of Zeolites: Adsorption, Diffusion and Dealumination*, **2009**, Scheikunde Proefschriften, Dissertation, Utrecht University.
- Barrett, E.P.; Joyner, L.G.; Halenda, P.B., *J. Am. Chem. Soc.*, **1951**, 73, 373
- Battaile, C.C.; Srolovitz, D.J., *Ann. Rev. Mat. Res.* **2002**, 32, 97.
- Beeler, Jr., J.R., *Phys. Rev.*, **1966**, 150, 470.
- Behrens, H., *Chem. Geol.*, **2010**, 272, 40.
- Belmabkhout, Y.; Sayari, A., *Chem. Eng. Sci.*, **2009**, 64, 3729.
- Bhattacharya, S.; Gubbins, K.E., *Langmuir*, **2006**, 22, 7726.
- Bogillo, V.I.; Pirnach, L.S.; Dabrowski, A., *Langmuir* **1997**, 13, 928.
- Boon, J.P.; Yip, S., *Molecular Hydrodynamics*, **1991**, Dover, New York
- Bortz, A.B.; Kalos, M.H.; Lebowitz, J.L., *J. Comp. Phys.*, **1975**, 17, 10.
- Bredesen, R.; Jordal, K.; Bolland, O., *Chem.Eng.Proc.*, **2004**, 43, 1129.
- Brucker, R., *Encyclopedia of Applied Physics*, **1997**, 18, 101

- Bunde, H.; Havlin, S., Chapters 2 and 3 in *Fractals and Disordered Systems*, **1991**, Springer-Verlag, Berlin.
- Burlakov, V.M.; Briggs, G.A.D.; Sutton, A.P.; Tsukahara, Y., *Phys. Rev. Lett.* **2001**, 86, 3052.
- Cabriolu, R.; Ballone, P., *Phys. Rev. B*, **2010**, 81, 155432.
- Carré, A. ; Berthier, L. ; Horbach, J. ; Ispas, S. ; Kob, W., *J. Chem. Phys.* , **2007**, 127, 114512.
- Catlow, C.R.A. ; Cormack, A.N., *Int. Rev. In Phys. Chem.*, **1987**, 6, 227.
- Chakravarty, C., *J. Phys. Chem. B*, **1997**, 101, 1878.
- Chapman, S.; Cowling, T.G., *The Mathematical Theory of Non-uniform Gases*, 3rd edition, **1990**, Cambridge University Press, Cambridge, UK.
- Chialvo, A.A.; Debenedetti P.G.; *Computer Physics Communications*, **1991**, 64, 15.
- Clarke, M.M.; Raff, L.M.; Scott, H.L., *Computers in Physics*, **1996**, 10, 584.
- Cohen, E.D.G., *Am. J. Phys.*, **1993**, 61, 524 .
- Coltrin, M.E.; Ho, P.; Moffat, H.K.; Buss, R.J., *Thin Solid Films*, **2000**, 365, 251.
- Condamin, S.; Tejedor, V.; Voituriez, R.; Benichou, O.; Klafter, J., *Proc. Natl. Acad. Sci. USA*, **2008**, 105, 5675.
- Connolly, M.L., *J.Appl.Cryst.*, **1983**, 16, 548.
- Cuffe, L.; MacElroy, J.M.D.; Tacke, M.; Kozachok, M.; Mooney, D.A., *J. Membr.Sci.* **2006**, 272, 6.
- Desu, S.B., *J. Am. Ceram. Soc.*, **1989**, 72, 1615.
- de Schepper, I.M.; Cohen, E.G.D., *Phys. Rev. A*, **1980**, 22, 287.
- Dubinin, M.M; Astakhov, V.A.; Radushkevich, L.V., In: (2nd Edition), Cadenhead D.A.; Danielli, J.F.; Rosenberg, M.D., Editors, *Physical Adsorption of*

Gases and Vapors in Micropores, Progress and Membrane Science, Academic Press, New York, **1975**, 9, 1.

Egelstaff, P.A., *An Introduction to the Liquid State*, 2nd Edition, **1992**, Oxford University Press, Oxford, United Kingdom.

Everett, D.H., Chapter 36 in *The Solid-Gas Interface* (Ed. E.A.Flood), **1967**, Marcel Dekker, Inc. New York.

Everett, D.H., *Pure Appl. Chem.*, **1972**, 31, 577.

Feenstra, K.A.; Hess, B.; Berendsen, H.J.C., *J. Comp. Chem.*, **1999**, 20, 786.

Fennell, C.J.; Gezelter, J.D., *J. Chem. Phys.*, **2006**, 124, 234104.

Fernandes, N.E.; Gavalas G.R., *Chem. Eng. Sci.*, **1998**, 53, 1049.

Fichtorn, K.A.; Weinberg, W.H., *J. Chem. Phys.*, **1991**, 95, 1090.

Frenkel D.; Smit, B., *Understanding Molecular Simulations*, **2002**, Academic Press, New York.

Gefen, Y.; Aharony, A.; Alexander, S., *Phys. Rev. Lett.*, **1983**, 50, 77.

Gelb, L.D.; Gubbins, K.E., *Langmuir*, **1999**, 15, 305.

Gelb, L.D.; Gubbins, K.E.; Radhakrishnan, R.; Sliwinska-Bartkowiak, M., *Rep. Prog. Phys.*, **1999**, 62, 1573.

Gillespie, D.T., *J. Phys. Chem.*, **1977**, 81, 2340.

Gilliland, E.R.; Baddour, R.F.; Perkinson, G.P.; Sladek, K.J., *Ind. Eng. Chem. Fundam.*, **1974**, 13, 95.

Grønbech-Jensen, N., *Int. J. Mod. Phys.*, **1997**, C8, 1287.

Grønbech-Jensen, N.; Hummer, G.; Beardmore, K. M., *Mol. Phys.* **1997**, 92, 941.

Gulmen, T.S.; Thompson, W.H., *Mater. Res. Symp. Proc.*, **2006**, 899E, 77.

Gusev A.A.; Muller-Plathe, F.; van Gunsteren, W.F.; Suter, U.W., *Advances in Polymer Science*, **1994**, 116, 207.

- Gusev A.A.; Suter, U.W., *J. Chem. Phys.*, **1993**, 99, 2228.
- Haile, J.M., *Molecular Dynamics Simulation*, **1992**, Wiley, New York.
- Hansen, J.P.; McDonald, I.R., *Theory of Simple Liquids*, 3rd Edition, **2006**, Academic Press, London.
- Hauptfear, E.A.; Olson, E.C.; Schmidt, L.D., *J. Electrochem. Soc.*, **1994**, 141, 1943.
- Hedin, N.; Chen, L.; Laaksonen, A., *Nanoscale*, **2010**, 2, 1819.
- Hedman, F.; Laaksonen, A., *Chem. Phys. Lett.*, **2006**, 425, 142.
- Heffelfinger, G.; van Swol, F., *J.Chem.Phys.*, **1994**, 100, 7548.
- Herzbach, D.; Binder, B.; Muser, M.H., *J. Chem. Phys.*, **2005**, 123, 124711.
- Hockney, R.W.; Eastwood, J.W., *Computer Simulation Using Particles*, **1989**, Taylor & Francis, Oxford,UK.
- Hofling, F.; Franosch, T.; Frey, E., *Phys. Rev. Lett.*, **2006**, 96, 165901.
- Hoshen, J.; Kopelman, R., *Phys. Rev. B*, **1976**, 14, 3438.
- Hughes, B.D.; Shlesinger, M.F.; Montroll, E.W., *Proc. Natl. Acad. Sci. USA*, **1981**, 78, 3287.
- Kajihara, K.; Hirano, M.; Takimoto, Y.; Skuja, L.; Hosono, H., *Appl Phys. Lett.*, **2007**, 91, 071904.
- Kappel, F.; Kuntsevich, A.V., *Comput. Optim. Appl.*, **2000**, 15, 193.
- Karttunen, M.; Rottler, J.; Vattulainen, L.; Sagui, C., *Current Topics in Membranes*, **2008**, 60, 49.
- <http://www.uni-graz.at/imawww/kuntsevich/solvopt/>
- Keating, P.N., *Phys. Rev.*, **1966**, 145, 637.
- Kertesz, J., *J. de Phys. Lett.*, **1981**, 42, 393.
- Kim, S.; Gavalas G.R., *Ind. Eng. Chem. Res.*, **1995**, 34, 168.

Knizhnika, A.A.; Bagaturyantsa, A.A.; Belova, I.V.; Potapkina, B.V.; Korkin, A.A., *Comp. Mat. Sci.* **2002**, *24*, 128.

Koehl, P., *Current Opinion in Structural Biology*, **2006**, *16*, 142.

Lastoskie, C.M.; Gubbins, K.E., *Advances in Chemical Engineering*, **2001**, *28*, 203.

Leach, A. R., *Molecular Modeling: Principles and Applications*, 2nd Edition, **2001**, Longman, Edinburgh.

Lee, D; Zhang, L.; Oyama, S.T.; Niu, S.; Saraf, R.F., *J. Membr .Sci.*, **2004**, *231*, 117.

Leimkuhler, B.; Reich, S., *Simulating Hamiltonian Dynamics*, **2004**, Cambridge University Press, Cambridge, UK.

Lekner, J, *Physica A*, **1989**, *157*, 826

Li, D.; Hwang, S.T., *J. Membr. Sci.*, **1992**, *66*, 119.

Libby, B.E.; Monson, P.A. paper 317e, *AIChE National Annual Conference*, November **2003**, San Francisco, CA.

MacElroy, J.M.D.; Raghavan, K., *J. Chem. Phys.*, **1990**, *93*, 2068.

MacElroy, J.M.D., *J.Chem.Phys.*, **1994**, *101*, 5274

MacElroy, J.M.D.; Friedman S.P.; Seaton, N.A., *Chem. Eng. Sci.*, **1999**, *54*, 1015

MacElroy, J.M.D.; Pozhar, L.A.; Suh, S.-H., *Coll. Surf. A*, **2001**, *187*, 493.

MacElroy, J.M.D., *Mol. Phys.* **2002**, *100*, 2369.

Mason, E.A.; Viehland, *J. Chem. Phys.*, **1978**, *68*, 3562.

Mayo, S.L.; Olafson, B.D.; Goddard, W.A., *J. Phys. Chem.*, **1990**, *94*, 8897.

McCann, M. T. P., *Plasma Deposition of Nanoporous Inorganic membranes for Gas Separation*, **2010**, PhD Thesis, University College Dublin, Ireland.

McNeil, W.J.; Madden W.G., *J.Chem.Phys.*, **1982**, *76*, 6221.

Merkel, T.C.; He, Z.; Pinnau, I.; Freeman, B.D.; Meakin, P.; Hill, A.J., *Macromolecules*, **2003**, *36*, 6844.

Mezei, M., *Mol. Phys.*, **1980**, *40*, 901.

Moloney, J., *Generation and Characterisation of Nano-porous Inorganic Membranes for High Temperature Gas Separation using Molecular Modelling*, **2011**, PhD Thesis, University College Dublin, Ireland.

Mooney, D.A.; MacElroy, J.M.D.; Kozachok, M.; Cuffe, L.; Tacke, M., *16th International Congress of Chemical and Process Engineering (CHISA)*, August **2004**, Prague, the Czech Republic.

Mountsier, T.W., *Chemical vapor deposition of low density silicon dioxide films*, **2000**, US Patent 6,054,206.

Mulder, M., *Basic Principles of Membrane Technology*, Kluwer Academic Publishers, **1996**, Dordrecht.

Nicholson D.; Parsonage N.G., *Computer Simulation and the Statistical Mechanics of Adsorption*, **1982**, Academic Press, London

Nicolas, J. J.; Gubbins, K. E.; Streett, W. B.; Tildesley, D. J., *Mol. Phys.*, **1979**, *37*, 1429.

Norman, G.E.; Filinov, V.S., *High Temperature (USSR)*, **1969**, *7*, 216.

Odagaki, T.; Hiwatari, Y., *Phys. Rev. A*, **1990**, *41*, 929.

Pandey, R.B.; Stauffer, D.; Margolina, A.; Zabolitzky, J.G, *J. Stat. Phys.*, **1984**, *34*, 427

Park, I.-A.; MacElroy, J.M.D., *Molec. Sim.*, **1989**, *2*, 105.

Pelmenschikov, A.; Leszczynski, J.; Petterson, L.G.M., *J. Phys. Chem. A*, **2001**, *105*, 9528.

Pereira, J.C.G.; Catlow, C.R.A.; Price, G.D.; *Chem. Commun.*, **1998**, *13*, 1387.

Powles, J. G., *Physica*, **1984**, A126, 289.

Pozhar L.A.; Gubbins, K.E., *J.Chem.Phys.*, **1993**, 99, 8970

Pozhar L.A.; Gubbins, K.E., *Phys.Rev.*, **1997**, E56, 5367.

Press, W.H.; Teukolsky, S.A.; Vetterling, W.T.; Flannery, B.P., *Numerical Recipes (3rd Edition)*, **2007**, Cambridge Univ. Press, Cambridge, UK.

Raghavan, K.; MacElroy, J.M.D., *Molec. Sim.* **1991**, 8, 93.

Ramamoorthy, A.; Rahman, M.; Mooney, D.A.; MacElroy, J.M.D.; Dowling, D.P., *Surf. Coat. Technol.*, **2008**, 202, 4130.

Rao, M.B.; Sircar, S., *J. Membr. Sci.*, **1996**, 110, 109.

Rintoul, M.D., *Phys. Rev. E*, **2000**, 62, 68.

Roman, H.E., *J. Stat. Phys.*, **1990**, 58, 375.

Rowlinson, J.S., **1988**, *On the Continuity of the Gaseous and Liquid States, Thesis, J.D. van der Waals*, Dover, New York.

Savitzky, A.; Golay, M.J.E., *Anal. Chem.*, **1964**, 36, 1627

Schaible, N., *Crit. Rev. Sol. State Mat. Sci.*, **1999**, 24, 265.

Schlick, T., *Molecular Modeling and Simulation - An Interdisciplinary Guide*, 2nd Edition, **2010**, Springer, New York.

Scholes, C.A.; Kentish, S.E.; Stevens, G.W., *Recent Patents on Chemical Engineering*, **2008**, 1, 52.

Schumacher, C.; Gonzalez, J.; Perez-Mendoza, M.; Wright, P.A.; Seaton, N.A., *Ind.Eng.Chem.Res.*, **2006a**, 45, 5586.

Schumacher C.; Gonzalez, J.; Wright P.A.; Seaton, N.A., *J. Phys. Chem. B*, **2006b**, 110, 319.

Shor, N.Z., *Minimization Methods for Non-Differentiable Functions*, **1985**, Springer Series in Computational Mathematics, Vol. 3, Springer-Verlag, Berlin.

- Smit, E.; Mulder, M.H.V.; Smolders, C.A.; Karrenbeld, H.; van Eerden, J.; Feil, D., *J. Membr. Sci.*, **1992**, 73, 247.
- Sone, Y., *Kinetic Theory and Fluid Dynamics*, **2002**, Birkhäuser, Boston.
- Staggs, J.E.J., *Fire Safety Journal*, **2005**, 40, 6, 493.
- Straley, J.P., *Phys. Rev. B*, **1977**, 15, 5733.
- Sung, W.; Dahler, J.S., *J.Chem.Phys.*, **1984**, 80, 3025.
- Takaba, H.; Mizukami, K.; Kubo, M.; Fahmi, A.; Miyamoto, A., *AIChE J.*, **1998**, 44, 1335.
- Taraskin, S.N.; Elliott, S.R.; Klinger, M.I., *Journal of Non-Crystalline Solids*, **1995**, 192 & 193, 263.
- Thompson, S.M., *CCP5 Quarterly*, **1983**, 8, 20.
- Thornton, A. W.; Hill, J. M.; Hill, A. J., **2010**, *Modelling Gas Separation in Porous Membranes*, in Membrane Gas Separation (Eds Y. Yampolskii and B. Freeman), John Wiley & Sons, Ltd, Chichester, UK.
- Tsapatsis, M.; Gavalas, G.R., *J. Membr. Sci.*, **1994**, 87, 281.
- Tsapatsis, M.; Gavalas, G.R., *AIChE J.*, **1997**, 43, 1849.
- Tuckerman, M.E.; Berne B.J.; Martyna, G.J., *J. Chem. Phys.*, **1992**, 97,1990.
- van Beest, B.W.H.; Kramer, G.J.; van Santen, R.A., *Phys. Rev. Lett.*, **1990**, 64, 1955.
- Verlet, L., *Phys. Rev.*, **1967**, 159, 98.
- von Alfthan, S.; Kuronen, A.; Kaski, K., *Phys. Rev. B*, **2003**, 68, 073203.
- Voter, A.F., *Introduction to the Kinetic Monte Carlo Method*, **2005**, in *Radiation Effects in Solids*, (Ed. Sickafus K.E.; Kotomin, E.A.), Springer, NATO Publishing Unit, Dordrecht, The Netherlands.
- Way, D.J.; Roberts, D.L., *Sep. Sci. Technol.*, **1992**, 27, 29.

- Weeks, J.D.; Chandler, D.; Andersen, Jr., H.C., *J. Chem.Phys.*, **1971**, 54, 5237.
- Wijmans, J.G.; Baker, R.W., *J. Membr. Sci.*, **1995**, 107, 1.
- Wolf, D.; P. Keblinski, P.; S. R. Phillpot, S.R.; Eggebrecht, J., *J. Chem. Phys.*, **1999**, 110, 8255.
- Wooten, F.; Winer, K.; Weaire, D.; *Phys. Rev. Lett.* **1985**, 54, 1392.
- Yampol'skii, Yu.; Pinnau, I.; Freeman, B.D.; *Materials Science of Membranes for Gas and Vapor Separation*, **2006**, John Wiley & Sons, New York.
- Yin, M.-Z.; Yao., X.; Zhang., L.-Y., *J. Zhejiang Univ. SCI*, **2004**, 5, 422.
- Young, W.M.; Elcock, E.W., *Proc. Phys. Soc.*, **1966**, 89, 735
- Zhdanov, V.P., *Elementary Physicochemical Processes on Solid Surfaces*, **1991**, Plenum Press, New York.

Refereed Papers in International Journals

McDermott T.C., Akter T., MacElroy J.M.D., Mooney D.A., Michael T.P. McCann M.T.P., Dowling D.P., Diffusion within Ultrathin Dense Nanoporous Silica Films, Langmuir (submitted) (2011)

McDermott, T.C., Moloney, J., Akter, T., McCann, M.T.P., MacElroy, J.M.D., Mooney, D.A., Dowling, D.P., Molecular Simulation of the Fabrication and Permselective Characterisation of Thin Nanoporous Silica Films, to be submitted to Diffusion Fundamentals.

Moloney, J., McDermott, T.C., Mooney, D.A., MacElroy, J.M.D., Dowling, D.P., Kinetic Monte Carlo Simulations of the Formation of Thin Silica Films via CVD on Microporous Substrates, to be submitted to J.Membr.Sci.

Akter T., McDermott T.C., MacElroy J.M.D., Mooney D.A., Dowling D.P., Atomistic Simulation of the Formation of Nanoporous Silica Films via Molecular Chemical Vapor Deposition on Non-porous Substrates, Langmuir, DOI:10.1021/la2031329 [online publication 05/10/2011] (2011).

McDermott, T.C.; MacElroy, J.M.D., 2004, Diffusion within a Near-Critical Nanopore, Mol.Phys., 102, 2113-2121.

Refereed Conference Proceedings

Akter T., McDermott T.C., MacElroy J.M.D., Mooney, D.A., 2008, Molecular Simulation of the Formation of Ultrathin Silica Films from TEOS (tetraethoxysilane) using Kinetic Monte Carlo AIChE National Annual Meeting, Philadelphia, Pennsylvania.

Moloney J.B., McDermott T.C., Mooney D.A., MacElroy J.M.D., 2007, Molecular Modeling of the Creation of Novel, Ultra-Thin, Nano-Porous Layers and Supported Membranes Using Chemical Vapor Deposition, Annual AIChE Meeting, Salt Lake City, November 5-9.

McDermott T., Mooney D.A., MacElroy J.M.D., 2007, Atomistic Simulation of the Formation of Nanoporous Silica Films via Chemical Vapor Deposition, Conference on Computational Physics, Brussels, September 5-8.

Akter, T., McDermott, T., MacElroy, J.M.D., Mooney, D.A., 2007, Modeling of thin silica layers via kinetic Monte Carlo (KMC) of TEOS deposition, Conference on Computational Physics, Brussels, September 5-8.

Akter T., McDermott T.C., MacElroy J.M.D., Mooney D.A., 2007, Studies into the Preparation of Model Microporous Silica and Molecular Simulation of Ultra-thin Oxide Layer Deposition on Porous Substrates, Conference on Computational Physics, Brussels, September 5-8.

Moloney J., McDermott T.C., Mooney D.A., MacElroy J.M.D., 2007, Studies into the Preparation of Model Microporous Silica and Molecular Simulation of Ultra-thin Oxide

Layer Deposition on Porous Substrates, Conference on Computational Physics CCP2007, Brussels, Belgium.

McDermott T.C., Kozachok M., Akter T., MacElroy J.M.D., Mooney D.A., 2006, Atomistic Simulation of the Formation of Nanoporous Silica Films Via Chemical Vapor Deposition, AIChE National Annual Meeting San Francisco, USA.

Kozachok M., MacElroy J.M.D., Cuffe L., Tacke M., McDermott T.C., Mooney D.A., 2005, Atomistic Simulation of Heterogeneous Silica Gas Separation Membranes, 7th World Congress of Chemical Engineering, Glasgow.

McDermott T.C., MacElroy J.M.D., 2002, Tracer Diffusion in a Simple Fluid Confined within a Model Silica Nanopore, Annual Symposium of the Irish Society for Scientific and Engineering Computation (ISSEC), NUI Galway, May 2002.

McDermott T.C., MacElroy J.M.D., 2002, Self-Diffusion of A Simple Fluid within a Crystalline Silica Nanopore Under Subcritical and Supercritical Conditions, XIV International Conference on Chemical Thermo-dynamics, St Petersburg, Russia, July 2002.